Investigations of metal organic precursors as direct write electron beam resists and their nanopatterning for functional devices

A Thesis

Submitted for the Degree of

Doctor of Philosophy

by

Bhuvana T

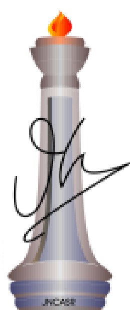

Chemistry and Physics of Materials Unit
Jawaharlal Nehru Centre for Advanced Scientific Research
(A Deemed University)
Bangalore – 560 064

JULY 2008

DECLARATION

I hereby declare that the thesis entitled "**Investigations of metal organic precursors as direct write electron beam resists and their nanopatterning for functional devices**" is an authentic record of research work carried out by me at the Chemistry and Physics of Materials Unit, Jawaharlal Nehru Centre for Advanced Scientific Research, Bangalore, India under the supervision of Professor G. U. Kulkarni and that it has not been submitted elsewhere for the award of any degree or diploma.

In keeping with the general practice in reporting scientific observations, due acknowledgment has been made whenever the work described is based on the findings of other investigators. Any oversight due to error of judgement is regretted.

Bhuvana T

CERTIFICATE

Certified that the work described in this thesis titled "**Investigations of metal organic precursors as direct write electron beam resists and their nanopatterning for functional devices**" has been carried out by Ms. Bhuvana T at the Chemistry and Physics of Materials Unit, Jawaharlal Nehru Centre for Advanced Scientific Research, Bangalore, India under my supervision and that it has not been submitted elsewhere for the award of any degree or diploma.

Professor G. U. Kulkarni
(Research Supervisor)

Acknowledgments

I thank my thesis supervisor, Professor G. U. Kulkarni, for introducing me to the field of nanolithography, for suggesting interesting research topics as well as for providing involved guidance through the investigations. He has indeed been a friend, philosopher and guide to me.

I thank Professor C. N. R. Rao for creating such a nice place as JNC with excellent research ambience, where young minds like mine learn. On a personal account, he has been very motivating and encouraging; I thank you Sir. I also received immense support from Professor M. R. S. Rao, President, JNCASR, which I gratefully acknowledge.

It is a pleasure to thank all my collaborators; Dr. Stefan Heun - Pisa University, Italy, Professor Timothy Fisher - Purdue University, USA, Professor T. Pradeep - IITM, Professor Chandrabhas, Dr. Luca Gregoratti and Mr. Dalmiglio - Elettra, Italy, Dr. Subramaniam - IITM, Dr. Pavan Kumar, and Kyle - Purdue University, USA, for active collaboration.

I am thankful to the faculty members belonging to JNC and Chemical Sciences division at IISc for course work.

My research work has derived technical help from many; Thanks to Mr. Srinath, Mr. Srinivas, Ms. Selvi, Mrs. Usha, Mr. Vasudeva, Mr. Anil, Mr. Basavaraj and Dr. Kiran and among students, particularly Gomathi, Bhat, Vivek, Neenu, Pranab,

Vengadesh, Kalyan and Jithesh. Mr. Sunil and Mr. Narasimhamurthy are thanked for their help.

I thank Mr. Jayachandra and staff members from administration, academic, complab and library for the service offered.

The financial support from DST towards the research work and fellowship as well as for sponsoring my visit to Elettra, synchrotron Italy through the NSTI program, is gratefully acknowledged.

I would like to thank past and present labmates - Dr. Angappane, Dr. Neena, Dr. Karthick, Ved, Reji, Vijay, Radha and Ritu. A special note of thanks to all the SRFs and POCE students for making the lab cheery during the summer.

The support from my friends - Gomathi, Jayashree, Sruthi, Mahalakshmi, Vengadesh, Dinesh, Harish, Pavan, Pranab, Kalyan, Madhu, Datta, Chaitanya, Muthukumar, Ramasastry and Nonappa, I affectionately acknowledge.

I would like to recall my affectionate association with Mrs. Kulkarni, Tejaswi and Poornachandra who treated me as a member of family.

I wish to express my gratitude to my parents, brother and sister for their unconditional support.

Preface

The thesis pertains to investigations of metal organic precursors as direct write electron beam resists and their nanopatterning for functional devices. It is organized into eight chapters. **Chapter 1** introduces the concept of nanoscale materials and their patterning using different lithographic techniques. **Chapter 2** discusses the zwitter resist action of polystyrene, which is hitherto known for its negative action. At low e-dosages, the resist behaves as negative resist masking electroless Au deposition while on increasing e-dosage, it works as a positive resist allowing Au deposition only to switch its behavior to successive negative and positive states with increasing e-dosage. The observed states of polystyrene have been examined using Raman spectroscopy. In **Chapter 3**, the results obtained using a blend of Ag triphenylphosphene nitrate and polystyrene as an e-beam resist are reported. Upon e-beam exposure, Ag nanocrystal patterns are formed, as revealed by SEM and TEM measurements. The nature of electrical conduction in Ag embedded patterns has been studied using conducting AFM measurements. The effect of variation in e-beam energy and its dwell time at a pixel has been studied. The I-V data acquired show that the dwell time required to produce conducting patterns decreases with increase in e-beam energy.

Chapter 4 presents the use of Pd hexadecanethiolate as a direct write e-beam resist. The hydrocarbon chains of the thiolate crosslink bringing about a negative resist action, which has been examined by a host of microscopy and spectroscopy

tools including XPS nanospectroscopy at a synchrotron beamline. The electrical behavior of a Pd nanowire patterned across gap electrodes has been studied while it was subjected to thermolysis at increasing temperatures. The Pd nanowires produced at 230 °C are found to be highly metallic with low carbon impurities. E-beam patterning of Ni butanethiolate and its thermolysis in sulfur atmosphere to yield NiS_2 nanowires is the subject of investigation of **Chapter 5**. I-V measurements on a single nanowire have shown that the nanowire behaves like an activated conductor, which is linked to the surface metallicity in bulk NiS_2. **Chapter 6** deals with the catalytic behavior of Pd nanocrystals obtained by the thermolysis of Pd thiolate, for the growth ZnO nanowires from a precursor solution. The ability of the Pd thiolate to act as an e beam resist has been exploited to obtain patterned catalyst and in turn, patterned regions of ZnO nanostructures. **Chapter 7** contains investigations on Au and Pd nanocrystalline films as solid substrates for surface enhanced Raman measurements and their nanopatterning for Raman chip fabrication. Raman enhancement factors of $\sim 10^7$ and 10^5 have been obtained for Au and Pd substrates respectively, by suitably controlling the morphology of the films. A Raman chip has been realized by EBL patterning of the substrates to obtain micron-sized SERS active regions, called 'SERS bits'. The chapter also presents another investigation related to SERS activity of femtolitre capacity metal cups. **Chapter 8** demonstrates the use of Pd hexadecanethiolate as a nanosolder. Carbon microfibres and carbon nanotubes as active elements have been soldered to gap electrodes by thermolysing the soldering precursor. Here, the Pd thiolate not only establishes ohmic contact but also directs nanotubes to self-assemble across the gap electrodes. These aspects have been examined in detail by a host of experimental techniques.

Contents

Preface **vii**

1 Introduction **1**

1.1 The Nanoscale 1

1.2 Nanomaterials 1

1.3 Quantum confinement and size dependent properties 3

1.4 Nanolithography 4

1.4.1 Lithography: Concepts and definition 6

1.4.2 Conventional lithography 7

1.4.3 An algorithm for lithography 17

1.4.4 Lithography techniques 21

1.4.5 Sub 100 nm lithography 34

1.5 Nanomanipulation 34

1.6 Characterization techniques 35

2 Polystyrene as a zwitter e-beam resist **41**

2.1 Introduction 42

2.2 Scope of the Present Investigation 43

2.3 Experimental Details 44

2.4 Results and Discussion 46

2.5 Conclusions 55

3 $Ag(PPh_3)_3NO_3$ - polystyrene blend as an e-beam resist to produce conducting Ag nanocrystal patterns 57

3.1 Introduction 58

3.2 Scope of the Present Investigation 59

3.3 Experimental Details 59

3.4 Results and Discussion 61

3.5 Conclusions 69

4 Pd hexadecanethiolate as a direct write e-beam resist and electrical characterization of patterned Pd nanowires 71

4.1 Introduction 72

4.2 Scope of the Present Investigation 73

4.3 Experimental Details 74

4.4 Results and Discussion 75

4.4.1 Thermolysis of Pd hexadecanethiolate 75

4.4.2 Electron beam writing on Pd hexadecanethiolate 80

4.4.3 A Pd nanowire circuit 91

4.5 Conclusions 93

5 Ni butanethiolate as a direct write e-beam resist and electrical characterization of patterned nanowires of NiS_2 95

5.1 Introduction 96

5.2 Scope of the Present Investigation 97

5.3 Experimental Details 97

5.4 Results and Discussion 99

5.5 Conclusions 107

6 Catalytic growth of ZnO nanostructures on e-beam patterned Pd 109

6.1 Introduction 109

6.2 Scope of the Present Investigation 112

6.3 Experimental Details 112

6.4 Results and Discussion 113

6.5 Conclusions 119

7 Nanocrystalline Pd and Au films as solid substrates for surface enhanced Raman scattering measurements and their nanopatterning leading to Raman chip fabrication 121

7.1 Introduction 122

7.2 Scope of the Present Investigation 125

7.3 Experimental Details 126

7.3.1 Preparation Au/C/Si substrates 126

7.3.2 Preparation Pd substrates 126

7.3.3 Patterned SERS substrates 127

7.3.4 Raman measurements 128

7.4 Results and Discussion 128

7.4.1 SERS using Au/C/Si substrates 128

7.4.2 SERS using Pd substrates 138

7.4.3 The concept of a Raman chip 140

7.4.4 SERS on Femtoliter Ag cups 144

7.5 Conclusions 148

8 Self assembled circuits of multi-walled carbon nanotubes with Pd hexadecanethiolate as a nanosolder 151

8.1 Introduction 151

8.2 Scope of the Present Investigation 153

8.3 Experimental Details 154

8.4 Results and Discussion 154

8.4.1 Soldering a carbon fibre 154

8.4.2 Self assembled and soldered CNT circuits 156

8.5 Conclusions 162

References 163

Publications 178

CHAPTER 1

Introduction

1.1 The Nanoscale

The word has its origin in Greek "nanos" or Latin "nanus", meaning "Dwarf". Nano refers to the power in 10^{-9}, simply, one billionth. Usually it is the length scale and therefore a nanometer, which is on the scale of atomic diameters. For comparison, a human hair (see Figure 1.1) is about 100,000 nanometers thick! Nanoscience refers to the science and manipulation of chemical and biological structures with dimensions in the range from 1-100 nanometers. Nanoscience building blocks may consist of anything from a few hundred atoms to millions of atoms, bearing properties that are not only fundamentally different from the bulk but also size dependent. Thus, nanoscience is about creating new chemical and biological nanostructures, uncovering and understanding their novel properties, and ultimately about learning how to organize these new nanostructures into larger and more complex functional structures and devices. In other words, it is a new way of thinking about building up complex materials and devices by exquisite control of the functionality of matter and its assembly at the nanometer-length scale.

1.2 Nanomaterials

A nanomaterial is one where at least one of its dimensions falls in the nanoscale regime. Nanometre-sized materials have attracted a great deal of at-

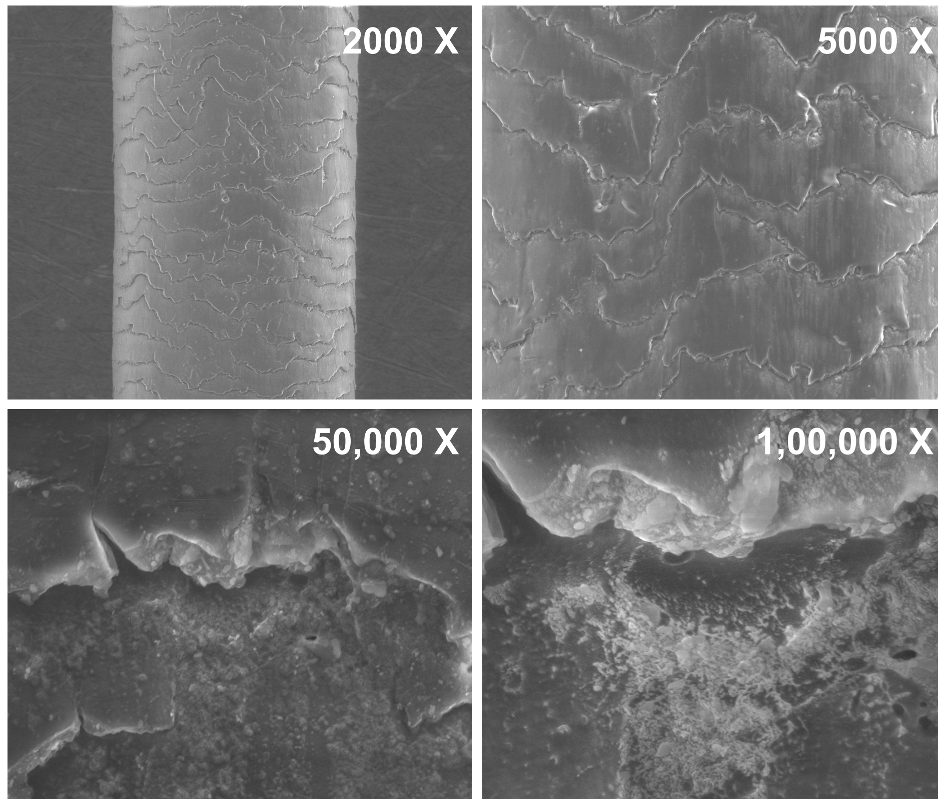

Figure 1.1: SEM image of a human hair at different magnifications. The nanostructure is clearly seen at higher magnification.

tention, in the recent years, due to the immense opportunities they offer in basic understanding as well as in a wide variety of applications. There have been continued efforts to synthesize well defined nanomaterials such as clusters, nanocrystals, nanotubes, nanowires and thin films [1]. Initial effort toward this goal started with Michael Faraday in the 19th century, who prepared Au nanoparticles in the form of a colloidal sol and termed them as 'divided metals' [2]. Of late, it has been possible to produce clusters of a given nuclearity (such as C_{60}, Au_{55} etc.), nanocrystals of metals and semiconductors of a given size distribution, carbon and inorganic nanotubes as well as nanocrystalline thin films of various materials. The surfaces of these nanomaterials can be functionalized with different organic and biomolecules

to aid desired organization at a mesoscalar level.

In the last few decades, several metals, semiconductors and other materials have been cast into nanomaterials. Although Faraday was the first to identify the nano state of matter, it is commonly believed that the experimental discovery of C_{60} gave birth to the 'modern' nanoscience. Clusters, in addition to offering several ways of making new materials, are a fundamental subject for understanding the intrinsic nature of materials. Small noble metal clusters are of particular interest because the dominance of quantum effects in such small dimensions alludes to the emergence of several interesting characteristics, such as their catalytic properties, etc. While most studies were concentrated on pure metallic clusters, it has recently been realized that mixed metallic clusters exhibit unique electronic, magnetic, optical, and mechanical properties. For example, mixed clusters of Au and Ag have been found to exhibit enhanced optical nonlinearity over the corresponding bulk metals. Another advantage of studying these mixed clusters is that they help understand the mechanism of alloying.

1.3 Quantum confinement and size dependent properties

Another aspect of the study of nanomaterials is their size dependent behavior. The property of a nanoscale object can be quite different from that of its bulk. The difference arises due to large surface to volume ratio which contains more atoms to the surface. The change in the property is also brought about due to quantum confinement of the conduction electrons at the nanoscale. This is schematically represented in Figure 1.2. The properties of a nanosystem can also be modified

by changing its shape. Very small nanoparticles or clusters (zero dimensional) behave like atoms with discrete energy levels. Two dimensional nanomaterials such as thin films exhibit steps in their electronic density of states (DOS), while van Hove singularities (sharp spikes) are observed in the case of one dimensional analogues. It is generally accepted that the quantum confinement of electrons by the potential wells of nanometer sized structures may provide a powerful means to control electrical, optical, magnetic and thermoelectric properties of a solid state functional material.

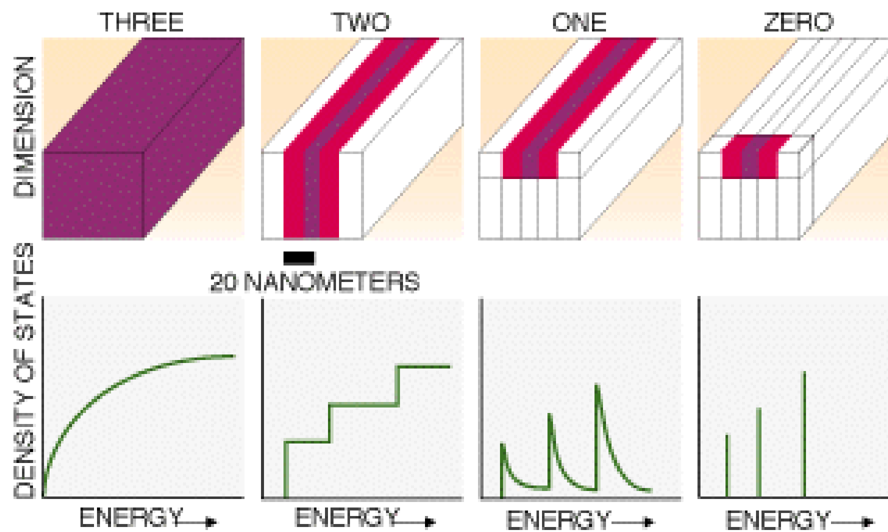

Figure 1.2: Density of states of a metallic system under quantum confinement in different dimensions. Reproduced from ref [3].

1.4 Nanolithography

Nanolithography is the lithography at the nanoscale. Although the basic ideas of lithography are old, the fabrication of structures on the nanometer length scale has made nanolithography an exciting new field of research during the last

one decade. The study of quantum phenomena in confined structures demands patterning periodic arrays, gratings or address systems at the nanoscale made of desired materials. This has resulted in a new class of electronic devices with interesting functionalities. Such applications demand the availability of highly sophisticated techniques capable of fabricating reproducible structures and devices in the nanometer regime. Nanolithography thus, has far reaching implications in fabrication and integration of nanodevices, which explains the importance given to it.

Nanolithography has been applied extensively to pattern new materials or to create new and complex structures using the known materials and studying the various properties-either individual or collective. Repetitive structures such as line grating or arrays of dots or nanopillars have been patterned while varying structural parameters such the feature size and inter-feature distance. The properties of patterned materials, especially electronic, magnetic and optical, have been studied extensively. Patterned materials have also been used as templates for the catalytic growth of other nanostructures such as carbon nanotubes and nanowires.

Another field of nanoscience where lithography is on high demand, is the fabrication of nanocircuitry. Here, the materials are to be patterned across specified nanoelectrodes and studied for their characteristics. There are a few important issues that come into play namely, laying nanoelectrodes, placing an active element like a nanotube or a quantum dot at the desired location either by nanomanipulation or by selective masking, soldering to improve the nanoelement-nanoelectrode coupling and finally, feeding and deriving electrical or optical signals from the nanocircuit. Indeed, each of these issues has developed into separate areas of research and technology.

Both repetitive and non-repetitive nanopatterning borrow several ideas from

conventional microlithography. The lithography beam is essentially a photon or charged particle (electron or ion) beam. In order to achieve the desired resolution, the light of smaller wavelength is used, extreme UV and even soft X-ray photons. A new set of techniques unique to nanolithography have emerged in the recent years. These techniques essentially make use of the scanning probe microscopy setups. Stamping methods have also been downsized to reach nanoscale dimensions.

1.4.1 Lithography: Concepts and definition

In Greek, litho means stone and *gráphein* means to write. It is virtually creating impressions on any surface. Although, caveman knew writing on the wall, it is was Aloys Senefelder in 1796 who invented a repetitive process of reproducing a drawing on Bavarian limestone, then transferring onto paper. Lithography is a generic term for a process in which something is printed on a surface that is receptive to 'ink' in some regions and repels 'ink' in other regions. In present day usage of the term, lithography refers to creating repetitive or non-repetitive patterns of a material on a given substrate, with a wide choice for both, the patterns being anywhere between submicron to nanometric in dimension. The processes involved are not very different from creating ink impressions on paper (Figure 1.3). Writing can be done in three different ways, the easiest of all, is direct write method where patterns are created on the surface directly using the ink. The surface on which the patterns are created is known as substrate and the ink can be referred to as resist. In another method, the impression of a pattern is first cut out on a surface, generally known as mask or stencil, which is then used to transfer the pattern onto a substrate using a brush carrying the ink or sprayed on the substrate with the mask. The advantages of using this method is firstly, the stencil or mask

which is cut out can be used several times to create the same pattern and secondly, the excess of resist/ink used is removed by lift-off of stencil after the inking process. Yet another way shown in the Figure 1.3 is to create an impression is to raise a 'mirror pattern' as a mould or stamp which is inked and stamped to create the impression.

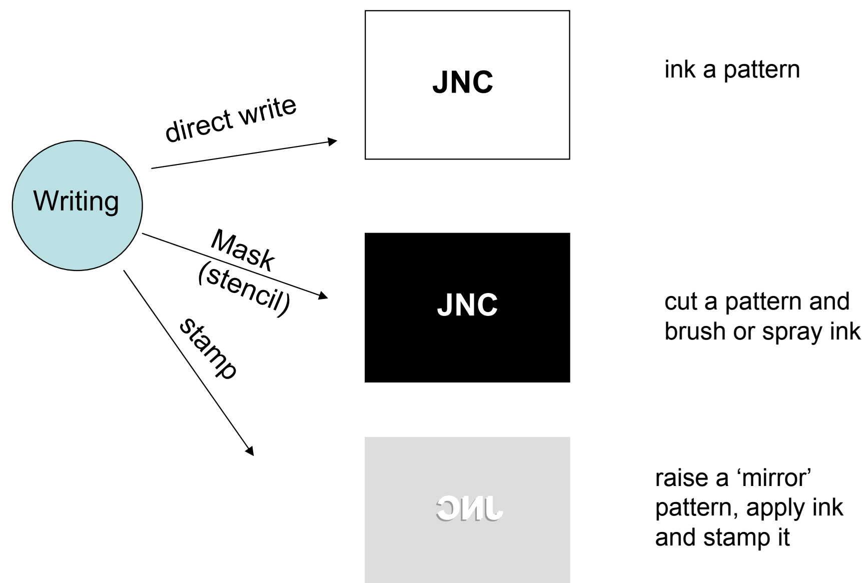

Lithography materials: 'ink', 'paper', 'pen', 'brush', 'mask', 'stamp'

Figure 1.3: Different ways of creating ink impressions on paper.

1.4.2 Conventional lithography

Microlithography, where the feature size is of the order of microns, is considered conventional but much of the ingredients and terminology remain similar for nanolithography. Typically, in microlithography based on light, a substrate is coated with a light sensitive resin (resist), which upon exposure to light transforms in such regions to another form with different properties so that such regions can be selectively retained or washed away. The active (desired) material such as a

metal is brought in during the second stage to finally create metal patterns on the substrate.

Preparing the Substrate

The substrates (also called wafers) used for lithography should be free from contamination. There are several methods to clean the substrate. The most commonly used method is ultrasonication, which physically removes particulate matter from the substrate. The medium can be organic solvents like acetone or alcohols or with distilled water. Wet cleaning involves RCA 1 and RCA 2 cleaning, wherein RCA 1 cleaning is done to removal of organic dirt while RCA 2 cleaning is performed to remove metal impurities. The composition of RCA 1 and RCA 2 reaction mixtures are NH_3:H_2O_2:H_2O::1:1:5) and (HCl:H_2O_2:H_2O::1:1:6) respectively. *(Caution: this mixture reacts violently with organic matter).* The cleaning is performed by heating the reaction mixture at 80 °C for 10 minutes. In the wet cleaning methods, DI water rinse is followed after every chemical treatment. After the cleaning, the substrate is dried under Ar or nitrogen gas. Other methods employed for cleaning the substrates are heating the substrates at high temperatures in vacuum or in oxygen or to use plasma etching techniques. The commonly used substrates are Si substrates or, Si substrates with thermally grown oxide as a dielectric layer for electronic applications, quartz, glass, etc. Si substrates are cleaned chemically using RCA 1 and RCA 2 methods before coating with a resist. For growing the oxide, the cleaned substrate is subjected to a high temperature (>850 °C) in the presence of oxygen flow. Depending on the required thickness of the oxide, the temperature and duration of oxidation is controlled.

Once the cleaning process is completed and the substrate is spin-coated with the resist to produce a thin uniform layer. This is a crucial step for effective pattern

transfer. The thickness of the resist is varied depending on its application. The volume of resist taken, its viscosity and the spinning rate are crucial for uniform resist film. In some cases, a monolayer of adhesion promotor, hexamethyldisilazane vapors (HDMS) is employed to make the surface hydrophobic. Sometimes, dry film resists (DFR), a photosensitive resin in a multilayer configuration with a carrier film and cover films are used in photolithography to form precision patterns.

Positive and Negative resists

The main component to perform lithography is the resist which undergoes the chemical changes on exposure of the light or electron beam. Taking photolithography as an example, polymers that on exposure to light undergo chemical transformations have been exploited as resists and are commonly known as photoresists. Polymers undergo chain scission or cross-linking on exposure of light resulting in an effective decrease or increase, respectively in their molecular weight. After exposure to light, these polymers show selective dissolution in some solvents known as developers. Based on this property, photoresist can be classified into two types, positive and negative photoresists. In the case of a positive resist, the region exposed to light solubilises in the developer (due to chain scission and decrease in the molecular weight) and the unexposed regions remains insoluble. In other words, the exposed resist leaves windows of the bare underlying material, hence, "whatever shows, goes." Negative resists behave in just the opposite manner. For a negative resist, the regions exposed to light become relatively insoluble in the developer compared to the unexposed regions (Figure 1.4).

Originally, the resists were mostly of the negative type, but since 1970s, the positive resists have also come into play. A well known example of a positive photoresist is poly(methylmethylacylate (PMMA). It undergoes chain scission un-

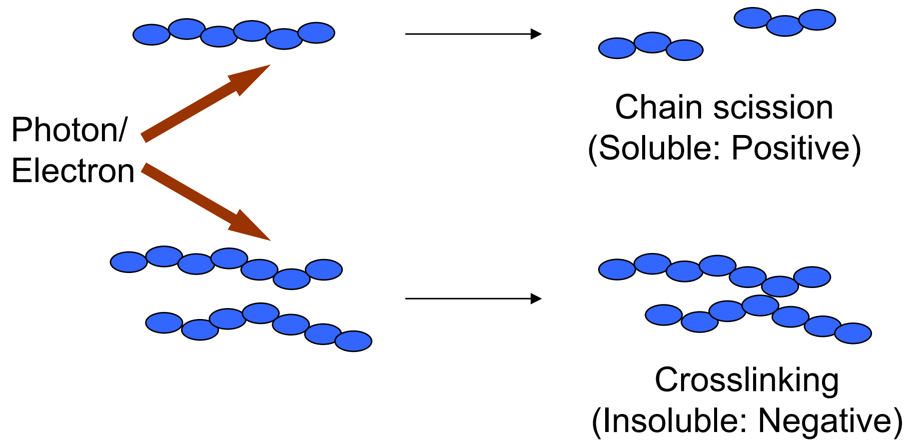

Figure 1.4: Schematic of the chemical changes undergone by positive and negative resist on exposure to photon/electron source.

der UV illumination. Sometimes to increase the sensitivity of the resist, a sensitizer is added. Phenolic Novolak, Diazonapthoquinine (DNQ) is an example of such resist, where diazoquinone ester is the photoactive species and phenolic novolak is the resin. Examples for negative photoresists are Kodak KTFR which is an azide-sensitized polyisoprene rubber. Similarly for electron beam lithography, polymers which undergo chemical change on exposure to electron beam are used. The best example for a positive e-resist is PMMA and for negative tone, examples are polystyrene and Calixarene. There are other commercially available resists for both photolithography and electron beam lithography such as Shipley, DUV, SU and ZEP series. After spin-coating a resist, the excess of solvent is removed by prebaking or soft baking. This step is performed in order to achieve the maximum adhesion of the resist to the substrate. Over-baking should be avoided as the resist film can decompose or it can degrade the photosensitivity of the resist either by reducing the developer solubility or actually destroying a portion of the sensitizer. Under-baking will prevent the light from reaching the sensitizer.

A *mask* is defined as a tool that contains patterns which can be transferred

to a resist coated substrate or to another mask in just a single exposure. A reticle is defined as a tool that contains a pattern image that needs to be stepped and repeated in order to expose the entire wafer or mask. The mask used for a positive resist contains an exact copy of the pattern which is to remain on the substrate whereas the mask used for negative photoresist contains the inverse (or photographic “negative”) of the pattern to be transferred. In Figure 1.5 are shown the difference in the patterns generated from the use of positive and negative resist using a same mask.

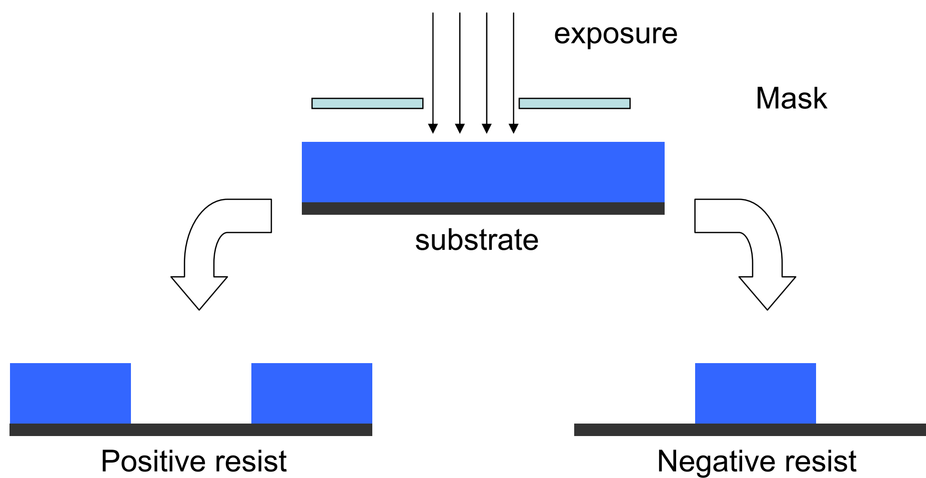

Figure 1.5: Patterns generated on positive and negative resist using a mask.

Exposure or dosage is a process to bring about the chemical changes in the resist using the light or e-beam. The dosage is very crucial as it decides the quality of patterns on the resist material. Underexposure may result in incomplete pattern transfer whereas overexposure may cause undue broadening of the pattern. In case of photolithography, dosage is defined as the energy (in mJ) dosed per unit area (in cm^2) where as in the case of electron beam lithography dosage is defined as charge (in μC) dosed per unit area (in cm^2). The exposure can be done in two ways: using a focused scanning beam or using a broad beam to project an entire pattern. The

major advantage of the second method is a higher pattern writing speed compared to serial writing of the focussed beam, where only small areas of pattern can be written at a time. Optical lithography is more popular because it is a projection based lithography and therefore, large areas can be patterned in a very short span of time whereas the non-optical based techniques which use charged particles like electrons are mostly focussed scanning based, making these process slow.

Developing

After the exposure, the substrate is developed in a developing solution. Development is carried out by immersion developing, spray developing or puddle developing. For example, in the case of PMMA, a mixture of methylisobutyl ketone: isopropyl alcohol (MIBK: IPA) in the ratio 1:3 has been found to be the best developing solution. At low-exposure energies, the negative resist remains completely soluble in the developer solution. As the exposure is increased above a threshold energy, more of the resist film remains after development. At exposures two or three times the threshold energy, very little of the resist film is dissolved. For positive resists, the resist solubility in its developer is finite even at zero-exposure energy. The solubility gradually increases until, at some threshold, it becomes completely soluble. Developing time varies from a few seconds to minutes. Higher the developing time, one has a better control for high definition patterns. Regardless of the method used, it should always be followed by thorough rinsing and drying to ensure that the developing action will not continue after the developer has been removed from the wafer surface. In order to remove the excess solvent and to harden the photoresist and improve adhesion of the photoresist, post baking/hard-baking is necessary. There are also physical methods such as reactive ion etching and plasma etching to develop the pattern. In these cases, the polymer does not come in con-

tact with the solvents. This is particularly advantageous in the case of negative photoresists as the swelling of the polymer is avoided.

Resolution, sensitivity and contrast

The resolution of a resist is defined as the smallest line-width to be consistently patterned. For positive resist, it is related to rate of chain scission and the rate of solubility with the molecular weight. Lower the molecular weight of the polymeric resist, higher the resolution. A disadvantage of negative resists is the fact that their exposed portions swell as their unexposed areas are dissolved by the developer. This swelling, which is simply volume increase due to the penetration of the developer solution into the resist material, results in distortions in the pattern features. This swelling phenomenon can limit the resolution of a negative resist. The unexposed regions of positive resists do not exhibit swelling and distortions to the same extent as the exposed regions of negative resists. This allows positive resists to attain better image resolution.

Lithography sensitivity is defined as the critical dosage required for removal (positive) or retention (negative) of half the thickness of the resist film. Resist sensitivity increases with increasing molecular weight. If the molecules are larger, then fewer cross-links are required per unit volume for insolubility. The sensitivity of a resist can be obtained from its response curve - a plot of normalized film thickness versus log D (dose). To construct such a curve, a series of varying dosages is given to a resist layer and developed. The thickness of the resist in the exposed region is measured and this value is normalized with the initial thickness and plotted against the cumulative or the total dosage. Sensitivity is then read out as the dosage at half the normalized thickness. The other important parameter is the resist contrast, γ [4]. The polymer molecules in the unexposed resist will have a

distribution of length or molecular weights and thus a distribution of sensitivities to radiation. The narrower the distribution, the higher will be the contrast, γ. Contrast is determined by the slope of the curve (Figure 1.6). It is a sigmoid response function obtained for different dosage. Contrast is calculated for positive and negative resists as

$$\gamma_p = (log(d_c/d_0))^{-1} \tag{1.1}$$

$$\gamma_n = (log(d_0/d_c))^{-1} \tag{1.2}$$

where d_0 is extrapolated dose at the kink of the contrast curve, d_c is the dose to clear all of the positive resist. In the case of a negative resist, d_i is the minimum dose required for the retention of the resist. Contrast decides the resolution. Typical contrast values fall in the range of 2 to 5 for novolak based positive resists, and 5 to 10 for DUV resists.

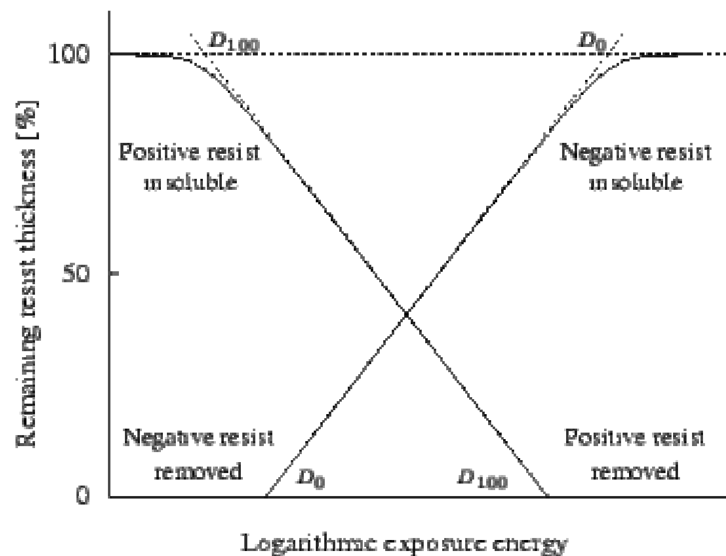

Figure 1.6: Sensitivity plot for positive and negative resist. The slope of curve gives the contrast parameter of the resist. Reproduced from ref. [4].

Clean room

Although the concept of cleanroom is more than 100 years old and is rooted in control of infections in hospitals, a clean environment for industrial manufacturing is only a recent requirement. In semiconductor fabrication industry, clean room processing is rigorous practice else, the dust particles, for example, can cause electrical breakdown of IC components. Coming to Nanotechnology, where fabrication is done using various nanolithographic techniques, it is necessary to avoid the dust and other contaminations as they can interfere with the fabrication. In such cases, a very high standard of cleanliness is required. Hence a clean room is a room that has a 'low' level of environmental pollutants such as dust, other contaminant particles and chemical vapors. More accurately, a cleanroom has a controlled level of permissible contamination that is specified by the number of particles in the ambient per cubic meter at a specified particle size. According to the definition provided by the International Organisation of Standardization (ISO) standard 14644-1,

> "A room in which the concentration of airborne particles is controlled, and which is constructed and used in a manner to minimize the introduction, generation, and retention of particles inside the room and in which other relevant parameters, e.g. temperature, humidity, and pressure, are controlled as necessary."

Cleanrooms are classified according to the number and size of particles permitted per volume of air. Large numbers like "class 100" or "class 1000" refer to the number of particles of size 0.5 μm or larger permitted per cubic foot of air. Clean rooms are rated as "Class 10,000," where there exists no more than 10,000 particles larger than 0.5 microns in any given cubic foot of air; "Class 1000," where

there exists no more than 1000 particles; and "Class 100," where there exists no more than 100 particles. The standard also allows interpolation, so it is possible to describe e.g. "class 2000" [5]. For example, the computer hard disk drive fabrication requires a Class 100 clean room.

A typical lithography recipe

Consider a set of useful patterns on a plane solid substrate. There are alternative recipes depending on the type of resist, mask and the order of metal deposition, prior or after resist coating. A typical procedure to obtain the desired pattern using a positive resist is explained here in Figure 1.7. The positive resist is spin coated on the substrate and prebaked. The light is exposed on the resist either using a mask or a fine beam is moved around to write the pattern. The resist after light exposure is developed using the developing solution, e.g., for PMMA, the developer is MIBK:IPA solution taken in 1:3 ratio. The features patterned on the resist are transferred to the substrate by lift-off. In a lift-off process, the desired metal is deposited on the patterned resist either by physical vapor deposition or by e-beam evaporation. Now the resist is stripped off completely. The metal that is deposited directly on top of the substrate where there is no resist, will stay, but the metal that is deposited on top of the resist will be lifted off along with the resist. The desired metal patterns are thus obtained on the substrate (see Figure 1.7). Further, the metal pattern can be used as etching mask for the substrate, if one plans to etch away some thickness of the substrate.

Another method to get the metal patterns using a positive resist is direct etching method. In this method, the metal is first deposited on the substrate and the pattern development on the resist is followed as described above. After developing

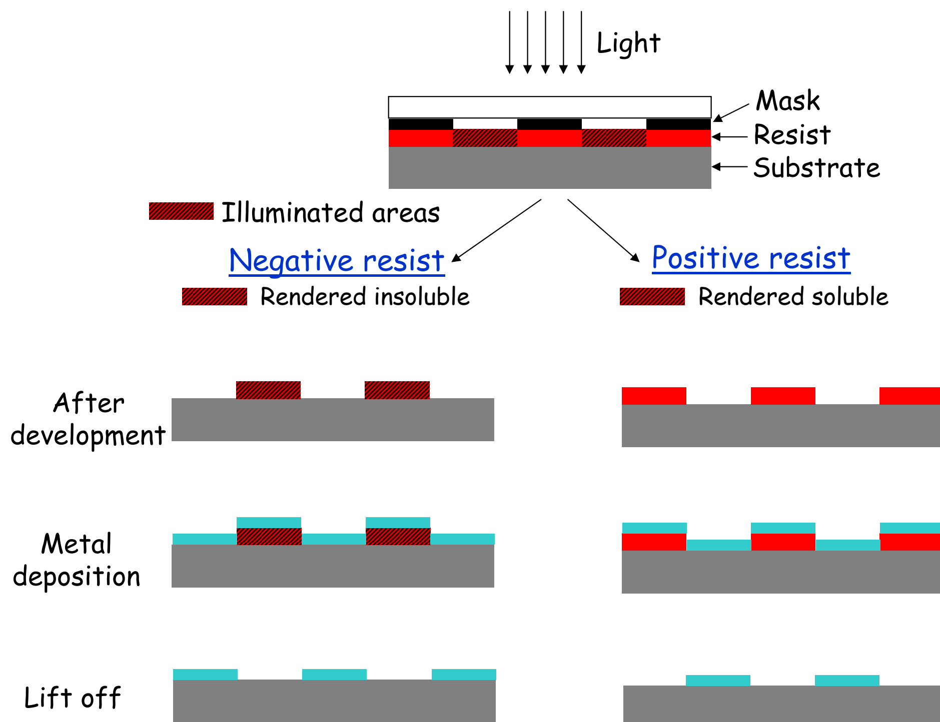

Figure 1.7: A typical photolithographic procedure adopted to get metal patterns by lift off process.

the resist, the metal which is not protected by the resist is etched away, e.g., for Au metal etching, cyanide solution is used. Alternatively, plasma etching can be done to remove the unprotected metal. After metal etching, the rest of the resist is washed away to get the metal patterns.

1.4.3 An algorithm for lithography

The above stated procedure is detailed but hard to comprehend, often even for a specialist. When a deviation is sought, say a negative resist in place of a positive resist, its influence on subsequent steps is not always easy to predict. There is clearly a need of a technical, more precisely a mathematical language to communicate lithography procedures crisply and unambiguously.

Let us begin with symbols.

Different types of lithography beams are possible. Beams of photons (p), electrons (e), ions (i) and atoms (a) are commonly used. A beam of atoms or clusters of a specific material may be denoted as M. This terminology may extend to force fields (f) in such cases where the lithography process involves application of pressure such as in stamping.

P_i stands for a pattern with the subscript 'i' representing the constituent material of the pattern. P_i^+ is a raised pattern of an ink, i; P_i^- is a reticular or stencil pattern cut in the material, i. Thus, the positive sign indicates a raised structure on the surface and the negative sign, a cut-out feature. W stands for the substrate (wafer), on which a pattern, P, is being produced. A pattern P laid on a substrate, W, is represented by a vertical line between them, $P \mid W$.

Example: *Writing with a pen (ink, i) on a paper (W) is the process*, $P_i^+ \mid W$. Cutting slits in desired places on a paper (i) is the process, $P_i^- \mid i$ or simply, P_i^- as it is self standing (here, W may be used interchangeably with i, $W \equiv i$).

A generated pattern may serve as a mask, 'S', in another experiment. Therefore, a 'P_i^-' pattern on a *transparent substrate* may be used as a shade mask, S_i^+. While using a shade mask, the substrate is invariably transparent to the lithography beam and the pattern itself, opaque. For a free standing shade mask such as a wire mesh, the substrate is illusive, just a slab of space around it! A 'P_i^-' pattern may work as a stencil mask, 'S_i^-'. Where 'i' is unimportant in the process, it may be dropped.

A material, i, is termed as R if it works like a resist, positive being R^+ and negative, R^-. When a resist film is exposed to the lithography beam through a mask and subjected to developing, D, by definition, R^+ retains the unexposed regions on the substrate while R^-, only the exposed regions. The resist pattern produced, P_R^+ or P_R^-, will depend on the nature of the mask, shade or stencil, as

illustrated below.

Let us walk through a simple photolithography process (Figure 1.8).

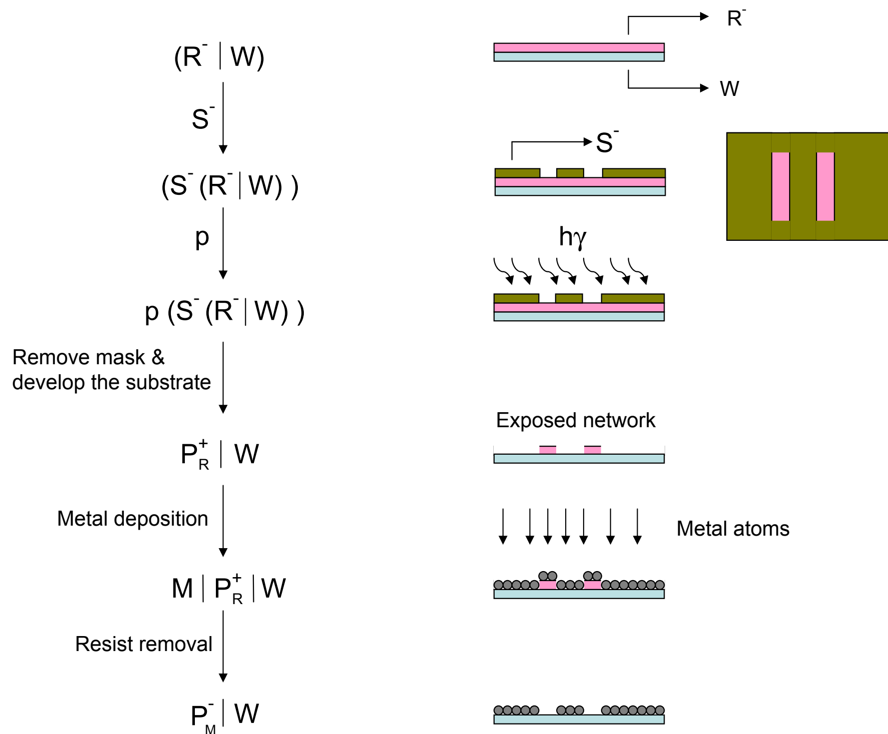

Figure 1.8: A typical photolithographic procedure adopted to get metal patterns by lift off process.

A negative resist is coated on the substrate as a thin film, $R^- \mid W$. A stencil mask is placed on top, $(S^-(R^- \mid W))$. A photon beam shines from the top to expose the resist through the mask, $(S^-(R^- \mid W))_p$. Following exposure, the mask is removed, $(R^- \mid W)_p$ and the resist is subjected to developing (D) in a solvent resulting in a patterned resist, $(P_R^+ \mid W)$. Now, metal M is deposited on top by PVD or by chemical means, $(M \mid P_R^+ \mid W)$. Finally, the unwanted metal is removed by lift-off (E) to produce a stencil pattern in the metal, $(P_M^- \mid W)$.

It may be noted that the vertical bar in between denotes the left *deposited* onto the right as against a set of parenthesis, which signifies the system as a whole. The

mask is *kept* but not deposited on the resist film. Another observation is that the various operations are shown alongside of the arrow (see Figure 1.8).

Let us consider an example where a positive resist is used in combination with a shade mask. The positive resist is coated on the substrate as a thin film, $R^+ \mid W$. A shade mask is placed on top, $(S^+(R^+ \mid W))$. A photon beam induces the resist action, $((S^+(R^+ \mid W))_p$. Following exposure, the mask is removed, $R^+ \mid W)_p$ and the resist is subjected to developing (D) in a solvent resulting in a patterned resist, $(P_R^+ \mid W)$. Now, metal M is deposited, $(M \mid P_R^+ \mid W)$. Finally, the unwanted metal is removed by lift-off (E) to produce $(P_M^- \mid W)$.

From the above examples, it is clear that a shade mask in combination with a positive resist produces the same resist pattern as the combination, a stencil mask with a negative resist. Indeed, they behave like algebraic operators,

$$(S^+(R^+ \mid W)) \longrightarrow (P_R^+ \mid W) \tag{1.3}$$

$$(S^+(R^- \mid W)) \longrightarrow (P_R^- \mid W) \tag{1.4}$$

$$(S^-(R^+ \mid W)) \longrightarrow (P_R^- \mid W) \tag{1.5}$$

$$(S^-(R^- \mid W)) \longrightarrow (P_R^+ \mid W) \tag{1.6}$$

The lift-off process (E) causes inversion.

$$(M \mid P_R^+ \mid W)) \longrightarrow (P_M^- \mid W) \tag{1.7}$$

$$(M \mid P_R^- \mid W)) \longrightarrow (P_M^+ \mid W) \tag{1.8}$$

The utility of the above algorithm is evident. Suppose one wants to produce a raised pattern of a metal on a substrate. Refer to equation 1.8 and work

back. One has to choose between (1.4) and (1.5), depending on the availability of the resist and the mask. This algorithm has been developed in the laboratory (www.jncasr.ac.in/kulkarni).

1.4.4 Lithography techniques

The different lithography techniques are briefly described in the following.

Photolithography

The resolution limit in conventional projection optical lithography is largely determined by the well-known Rayleigh's equation. The resolution, R and the corresponding depth of focus (DOF) are given by the following [6],

$$R = k_1\lambda/NA \tag{1.9}$$

$$R = k_1\lambda/NA^2 \tag{1.10}$$

where λ is the exposure wavelength, NA is the numerical aperture of the optical system, and k_1 and k_2 are constants that depend on the specific resist material, process technology, and image-formation technique used. High resolution photolithography therefore relies photon beam wavelengths shorter than visible range, deep in UV such as from excimer lasers (248 nm and 193 nm). At such short wavelengths, absorption loss from the optical components and air is considerable and may call for preventive measures using suitable instrumentation involving vacuum. There are many variations of photolithography, aimed at circumventing the diffraction limit.

A method of phase shift lithography includes forming a chromeless phase shift

reticle with a pattern of parallel, spaced phase shifters. The phase shift reticle is placed between an exposure source (e.g., UV light) and a substrate having a layer resist formed thereon. Following an initial exposure, the phase shift reticle is rotated and the substrate is exposed a second time. The resist is then developed to form features in areas of resist that have not been exposed. These areas correspond to the projected points of intersection of the phase shifters. Using a positive tone resist, solid resist features are formed. These solid features can be used as mask blocks for etching the substrate to form field emitter sites for a field emission display. Using a negative tone resist, open areas are formed in the resist and can be used to deposit a material on the substrate such as a contacts for a semiconductor structure. The method of the invention can also be implemented using two different reticles with intersecting patterns or using a single reticle having intersecting phase shift areas.

The stencil method is based on selective deposition of material through shadow masks (micro- and nanostencils). The main added value of this technique is that it does not rely on photoresist processes. Although photolithography is still the main method used for creating micro- and nanostructures in thin films, it requires several process steps, for example, application of photoresist, exposure, development, evaporation of a thin film, and lift off. The stencil method can create a structured thin film in one process step. The deposited structures can either be used directly, transferred into a sub-layer, combined by lift-off processes, or refined by self assembly or other growth processes. The stencil method typically uses solid-state membranes with structures in the nanometer range (<100 nm) in combination with micrometer features (>10 μm). These patterns can be transferred to a substrate in a single process step, potentially in a non-contact mode. These specifics make the stencil method applicable to surfaces that are either mechanically unstable, such as

cantilevers and membranes, and/or functionalized for e.g. bio-sensor applications.

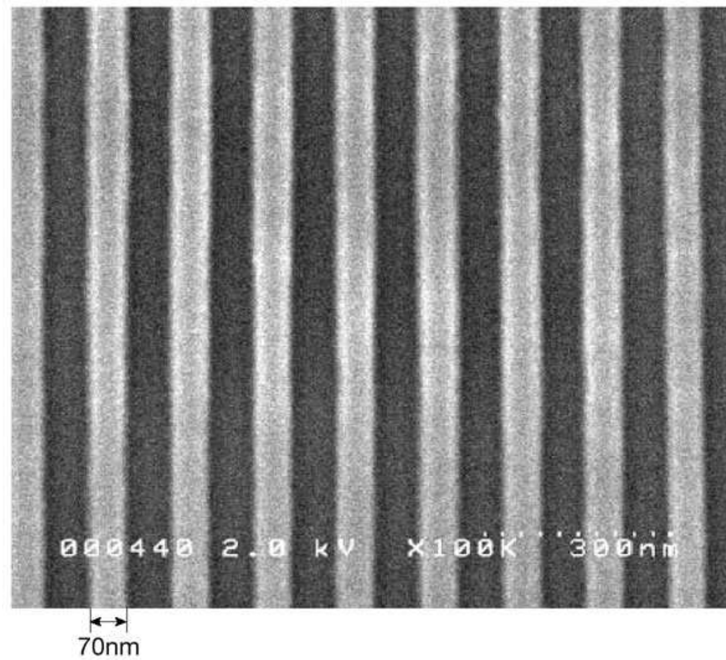

Figure 1.9: Patterns generated on PMMA by EUV microlithography system. Reproduced from ref. [8].

Collimated X-rays are also used as source and this process is known as X-ray lithography (XRL). Being much shorter in wavelength (∼1 nm), X-rays provide increased lateral resolution and in addition, a higher depth of focus. Scattering is also relatively less in case of X-rays. The most commonly known X-ray resist is PMMA, which is a positive resist and is being extensively used whereas negative resists such as polyglycidylmethacrylate (PGMA) have also been developed. The mask used for XRL basically consists of a pattern of X-ray absorbing materials such as Au (high atomic number material) on a substrate relatively transparent to X-rays such as Ti, Si, SiC, Si_3N_4, BN and B (low atomic number materials) [7]. For resist removal and etching, usually physical methods are employed.

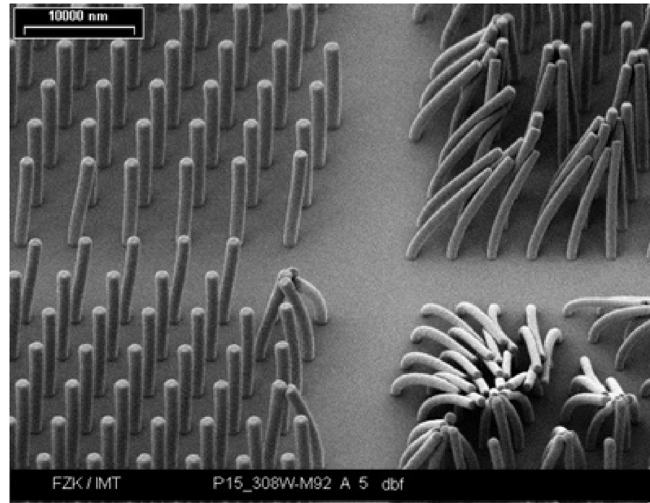

Figure 1.10: Patterns generated by X-ray lithography on a 10 μm SU-8 film, fields of columns with different diameter and pitch. Patterns themselves indicates for the limit of stability. Reproduced from ref. [9].

Charged particles based techniques

Apart from using light sources for lithography, charged particle beams of electrons, protons or ions, are extensively used for patterning the polymeric films. These are preferred over the light based techniques because the de Broglie wavelengths of these particles are sufficiently short (<0.1 nm) that they minimize the effects of diffraction that currently limit many photolithographic approaches. In addition, they allow high depth and fine focus. These techniques are generally performed in high vacuum conditions unlike photolithography. The exposure dose has units of charge deposited by the beam per unit area μC.cm^{-2}. Electron beam lithography (EBL) - in which a beam of electrons is used as the exposure source has extremely high-resolution capabilities combined with a large depth of focus. The patterning can be done in serial or parallel method depending on the type of patterns to be generated. Field emission sources are preferred over thermionic guns because of high achievable beam currents and focus. The beam current is in

the range of pico to nanoamperes. The shorter wavelength possessed by the 2-50 kV electrons are not limited by diffraction unlike photolithography. While using a finely focused electron beam makes it possible to delineate extraordinarily fine patterns down to 10 nm, EBL does suffer from proximity effect due to secondary electrons. Besides, writing of chip-scale patterns with a single electron beam is rather a slow process. According to the pattern complexity, the exposure time for writing also becomes very long, hence low throughput. Therefore, EBL remained as a high-end technique and was primarily employed to make high resolution masks and reticular structures. However with the advent of high current sources and faster electronics since the last two decades, EBL is now being applied for raised patterns of metals, semiconductors and polymers in fine-scale devices. EBL is also used in the small-scale production of the specialized very high frequency devices.

PMMA was one of the first resists developed for EBL in 1968 and is the highest resolution resists commonly available. PMMA is a chain-scission type resist which allows for high resolution because of its high contrast. Another popular positive resist is ZEP. Negative resists work by cross-linking and in general the patterns they produce in EBL are not as good as those produced with positive resists. The patterns suffer due to swelling during development and bridging between features.

The sensitivity of a e-resist is dependent on the beam current and the electron beam voltage. As a rule of thumb, the sensitivity scales proportionally with the acceleration voltage. For example, ZEP has its sensitivity of 200 μC.cm^{-2} at an acceleration voltage of 100 kV. This dose will be reduced to around 60 μC.cm^{-2} at 30 kV! PMMA can be patterned using electron dosage of $\sim$10 μC.cm^{-2} at 30 kV. If the dosage is increased, it behaves like a negative resist, however, the resolution will be degraded to about 50 nm. Generally for most resists, the e-dosage varies from few μC.cm^{-2} to C.cm^{-2}. The dosage is calculated based on the dose given

per pixel.

Area dose = (beam current x exposure time x number of passes)/area per pixel (1.11)

Line dose = (beam current x exposure time x number of passes)/length of the pixel (1.12)

For EBL, the substrate has to be conducting to get high resolution patterning. Of late, researchers have worked with insulating substrates and performed high resolution patterning. One such example is shown in Figure 1.11. Sol gel precursors are also cast into the patterns generated by EBL (Figure 1.12).

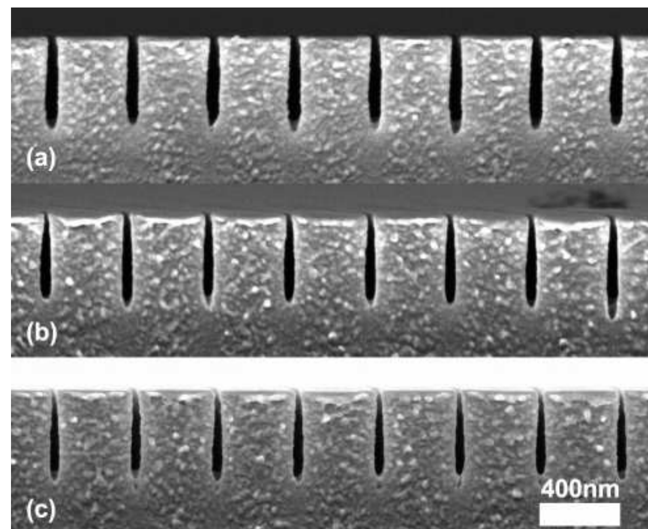

Figure 1.11: SEM images of PMMA cross sections following exposure of line arrays with a 30 keV primary beam energy and uniform line dose of 2 $nC.cm^{-2}$ under (a) high vacuum, (b) 1 Torr, and (c) 2 Torr. Reproduced from ref. [11].

By analogy to EBL, focused ion beam lithography (FIB) [17] scans an ion beam across a surface to form a pattern. Application of a very high electric field onto a liquid metal source such as Ga generates ions (Ga^{+}), which are focused by electrostatic lenses. The development of liquid metal ion source (LMIS) is crucial for the development of FIB. The ion beam may be used for directly sputtering the

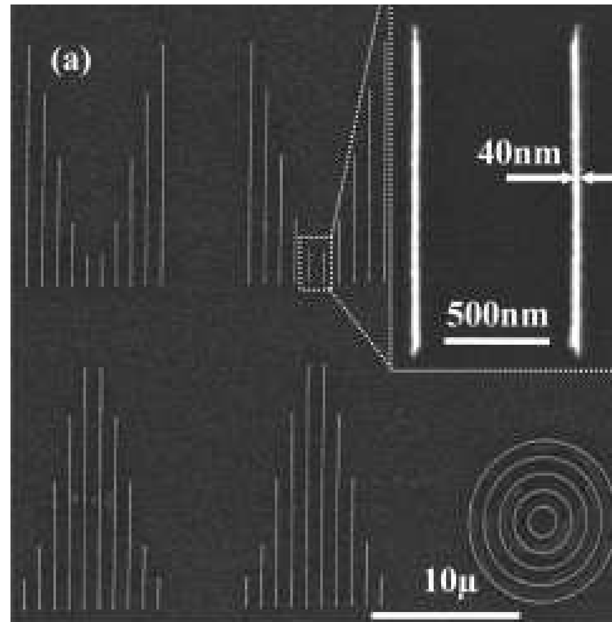

Figure 1.12: Backscattered electron image of ZnO patterns starting with sol-gel precursor on SiO_x substrates annealed in air at 700 °C for 20 minutes. Reproduced from ref. [12].

surface, or to induce chemical reactions in the resist layer. Redeposition of the sputtered material is a common occurrence, which affects the final surface profile. In the case of resist exposure, even though the beam spot size is smaller, secondary electrons limit the achievable resolution to about 30 nm. FIB is commonly used for repair of photomasks such as Au on Si. PMMA is the commonly used resist for patterning. Other ions used are H^+, He^+ and Ar^+ ions. Of late, H^+ based ion beams are increasingly used in lithographic techniques, known as proton beam lithography. Neutral metastable atoms can also be used for particle-based lithography. Neutral atoms are attractive partly because they do not electrostatically interact with one another. Their neutrality requires, however, development of new types of optics based on light forces. Initial results are encouraging: features as small as ∼50 nm have been fabricated in a single step over large areas with stencil masks and ∼70

nm features have been produced using directed deposition with light force lenses.

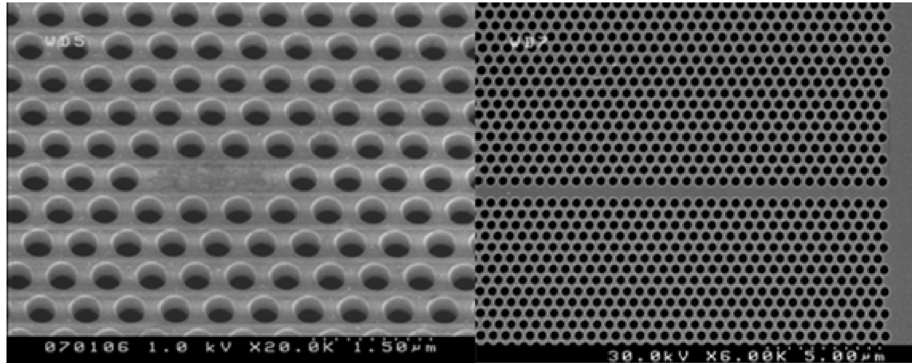

Figure 1.13: SEM micrograph of a) a photonic crystal L3 cavity b) a photonic crystal waveguide fabricated by FIB milling. Reproduced from ref. [10].

Scanning probe lithography techniques

Scanning probe lithography (SPL) [13] encompasses techniques that use sharp (<50 nm) tips scanned near the surface of a sample in the configuration of scanning tunneling microscopes (STMs) and atomic force microscopes (AFMs), or many variations. Although scanning probes were originally designed to provide high-resolution images of surfaces, their lithographic capability was demonstrated in a set of experiments with an STM, just five years after the first STM images were recorded. A large electrical bias applied between a tungsten tip and a Ge surface caused transfer of a single atom from the tip to the surface [23]. Since then, STMs and AFMs are being employed in many different ways to perform sophisticated lithography. Of the two, AFM is more popular due to variations possible.

Advantages of SPL methods include resolution that approaches the atomic level, the ability to generate features with nearly arbitrary geometries, and the capability to pattern over surface topography that deviates significantly from planarity.

However, these methods are serial and have writing speeds that are typically limited by the mechanical resonances of the tips and the piezoelectric elements that maintain constant separation between the tips and the sample. This problem is partially overcome in AFM by hosting parallel cantilever tips to perform repetitive patterning.

There are many variations of AFM based lithography techniques. A biased AFM tip under the influence of water from the ambient can locally oxidize the substrate (usually Si), which is termed as local anodic oxidation (LAO) [24]. A slight variation of this technique is the electrostatic nanolithography which refers trench formation when conducting tip ploughs patterns out of polymer films coated on substrates [25]. Thus formed trenches may be filled with molecules and nanoparticles. There are combinations of these techniques as well. Dip-pen lithography

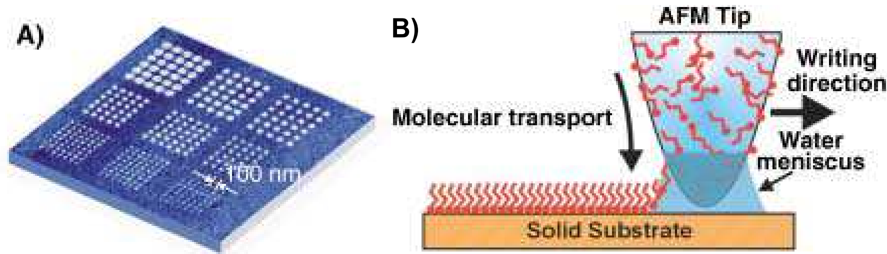

Figure 1.14: (a) Nanoscale dot arrays written on a polycrystalline Au surface with mercaptohexadecanoic acid and (b) schematic of DPN technique. Reproduced from ref. [14].

(DPN) [14], a AFM based technique has become a powerful tool for patterning nanostructures. In DPN, a material (ink) coated on the tip of the SPM cantilever is transferred to the substrate during slow scanning, facilitated by diffusion through a water meniscus. Hence it is a direct-write method and the variety of materials that can be patterned is boundless. Furthermore, the simplicity of the technique

and the higher resolutions achieved render it a more attractive one. Initial success with patterning of alkanethiol molecules was followed by other self-assembling molecules on substrates such as silicon, mica, glass and gold films. The molecular patterns can act as resists for the patterning of underlying films or can be modified further to attach nanoparticles or metal ions. Since DPN is based on the spatial confinement of materials, the pattern resolution chiefly depends on the tip diameter; however, humidity, temperature, nature of the ink, scan rate etc also affect the ultimate dimensions of the pattern. In the literature, DPN has been used to pattern colloids, fluorescent molecules, biomolecules like oligonucleotides, proteins and collagen, conducting polymers, and precursors for solid structures. The magnetic nature and chemical identity of nanopatterns have also been probed. Patterning of Ni catalyst for the selective growth of GaN nanotubes has also been demonstrated. Large-scale patterning is also feasible by employing parallel pen plotters and inkwells. Recently, nanofountain pen technology has been utilized to dispense liquid materials directly on to the substrate.

Soft lithography

This is an extension of stamping method to micro and nanolithography. Soft lithography [15, 16] (see Figure 1.15) is the collective name for a set of lithographic techniques: replica molding (REM), microcontact printing (μCP), micromolding in capillaries (MIMIC), microtransfer molding (μTM), solvent-assisted micromolding (SAMIM), and nearfield conformal photolithography using an elastomeric phase-shifting mask. These techniques use a patterned elastomer (usually PDMS) as the mold, stamp, or mask to generate or transfer the pattern with feature sizes down to 100 nm. Soft lithography offers immediate advantages over photolithography and other conventional microfabrication techniques for applications in which patterning

of nonplanar substrates, unusual materials, or large area patterning are the major concerns. It provides a convenient, effective, and low-cost method for the formation and manufacturing of micro- and nanostructures. It is especially promising for microfabrication of relatively simple, single-layer structures for uses in cell culture, as sensors, as microanalytical systems, in MEMS, and in applied optics. The initial success of soft lithography indicates that it has the potential to become an important addition to the field of micro- and nanofabrication.

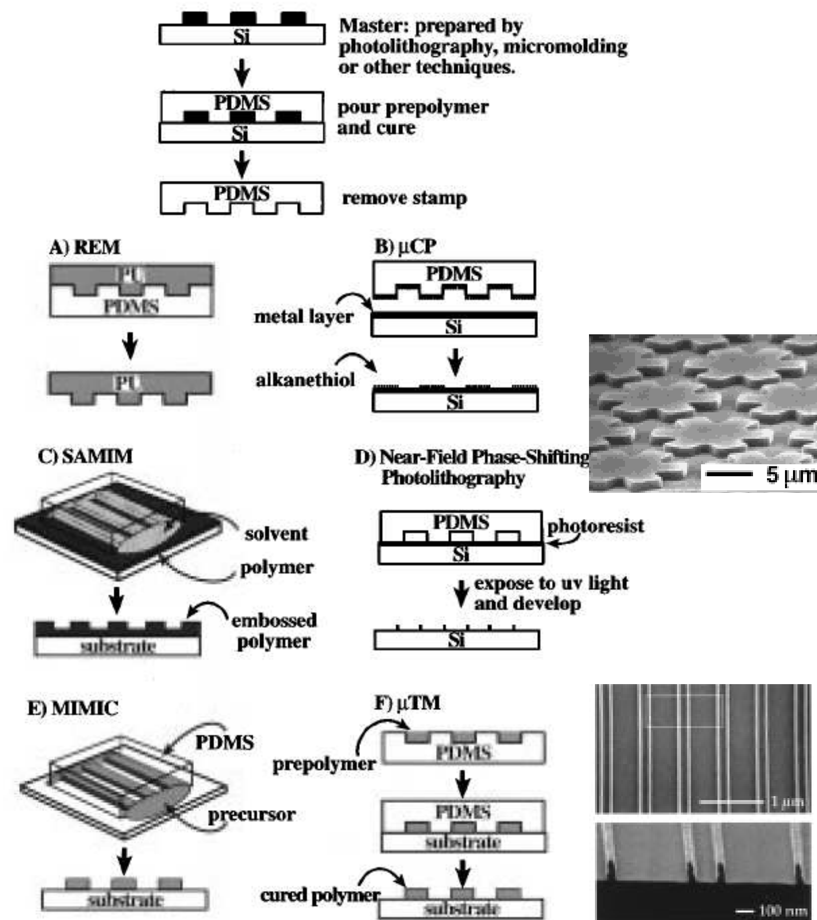

Figure 1.15: Different soft lithographic processes with some typical examples. Reproduced from ref. [15].

Nanoimprint lithography is a novel method of fabricating nanometer scale pat-

terns. It is a simple process with low cost, high throughput and high resolution. It creates patterns by mechanical deformation of imprint resist and subsequent processes. The imprint resist is typically a monomer or polymer formulation that is cured by heat or UV light during the imprinting. Adhesion between the resist and the template is controlled to allow proper release.

Direct write techniques

Dip-pen lithography (DPN) is a good example of a direct write technique. Direct write techniques are simple and straightforward. In other words, the number of process steps are minimal, usually ‘filling the ink’ and ‘writing’. Post processing may be as simple as drying in air! EBL or FIB based direct write techniques [17–19] have been around for quite some time. Electron or focussed ion beam-induced deposition (EBID or FIBID) is a direct-write process in which a pattern is defined directly by a focused electron (ion) beam, without any additional processes or treatments. In a typical setup, metal-organic precursor molecules (generally of W, Fe, Au and Pt) are directed onto a substrate by a gas nozzle in the e-beam vacuum chamber. Under the influence of a focused electron beam, the adsorbed molecules are dissociated into volatile and non-volatile fragments. Depending on the precursor molecules, these fragments form a metal rich deposit. The volatile components are pumped away by the vacuum system. These techniques are usually employed to define interconnects soldering nanoelements in circuitry. The deposit may have poor electrical characteristics because of carbon contamination from the organics.

Instead of cracking the vapor phase precursors by the electron beam, there is increasing interest worldwide, to innovatively come up with direct write resist precursors [21], that may be coated in the solid form on substrates. These resists

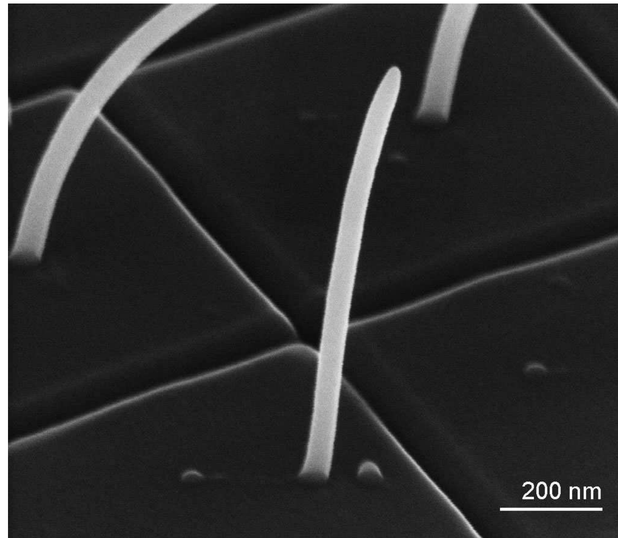

Figure 1.16: Electron-beam deposition of 50 nm thin, 1 micron tall, Pt nano-wires. Reproduced from ref. [20].

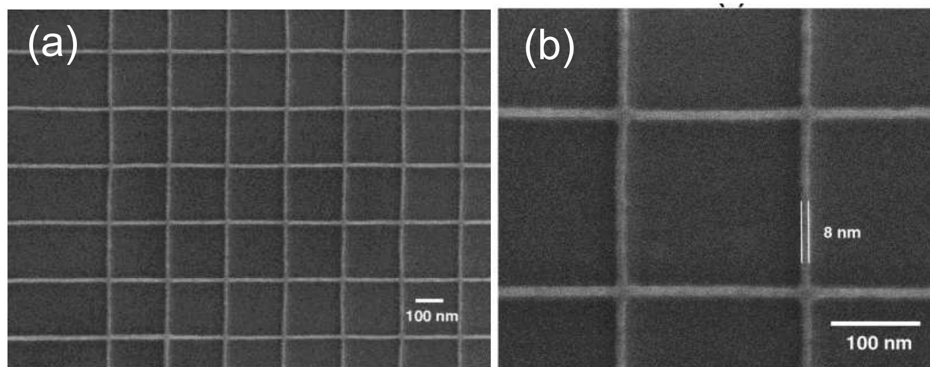

Figure 1.17: (a) SEM images of sub-10 nm patterned grid using a spin-coatable TiO_2 resist. (b) An 8 nm wide line. Reproduced from ref. [21].

uniquely possess the ability to pattern (resist action) and at the same time, transform into desired nanomaterial in a single step processing. Recently, there are innovations in stamping methods that allow direct patterning of the nanomaterial.

1.4.5 Sub 100 nm lithography

The terminology, sub-100nm lithography, is applied to clearly distinguish those recipes which enable one to perform patterning below 100 nm as against those which do not. Such a distinction is but natural as materials below 100 nm behave differently due to quantum confinement. Accordingly, the implications and their potential applications are of immense importance. The sub-100 nm recipe itself may have been derived from any known lithography technique or from a new combination of techniques. SPL techniques such as DPN [14] are good examples for sub-100 nm lithography techniques. EBL, EBID and FIBID techniques as well, on routine basis, can reach below 100 nm. The smallest values identified so far are 1.9 nm for lines and 0.72 nm for dots! The de Broglie wavelengths of the charged particles can be sufficiently short (<0.1 nm), keeping broadening due to diffraction effects minimal, unlike many photolithographic approaches. However, phase contrast photolithography and such methods have intelligently brought the resolution down to below 100 nm [22]. Scientists at IBM have fabricated distinct and uniformly spaced ridges only 29.9 nm wide using 193-nm lithography. This has beaten the 32 nm mark that industry had held as the limit for optical lithography. Among stamping methods, nanoimprint lithography is able to pattern below 100 nm. Examples from other inexpensive soft stamping methods are not common. Once in place, they would replace all other methods because of achievable speed.

1.5 Nanomanipulation

There have been major developments in techniques, that enable manipulation of individual nanoobjects or a group of nanoobjects. Nanomanipulation, as a cousin of nanolithography, makes use of similar instrumentation and therefore,

has seen considerable growth side by side. In one sense, if nanolithography forms the body, nanomanipulation represents its limbs and hands. The finest example of manipulation came out the first, way back in 1993, when a sharp STM tip was used as a billiard stick to place individual atoms to form quantum corral [26]. Since then, probe techniques are being extensively used to displace and transport atoms molecules and nanoobjects like, nanoparticles and nanotubes. The cantilever tip on AFM setup has been used as a shaving blade to rip off portions of SAMs [27]. By electrically activating or deactivating AFM tip, nanoobjects can be lifted and dropped [28] much the same way a crane works in the macroscopic world. In this sense, AFM tip has served as a gripper. Mechanical grippers activated by peizo-drivers allow manipulation at submicron length scales, if not truly at the nanoscale.

1.6 Characterization techniques

Several spectroscopic and microscopic techniques have been used to characterize the prepared samples reported in this thesis. In the following paragraphs, the details of instruments used and the sample preparation methods are described.

1.6.1 X-ray diffraction

Powder X-ray diffraction measurements were performed using a Siemens Seifert 3000TT diffractometer employing Cu Kα ($\lambda = 1.5406$ $\AA$) radiation. Samples were prepared by depositing the nanomaterials in the form of films on glass slides and typical scan rate was 1 deg.min^{-1}.

1.6.2 Thermogravimetric analysis

Thermogravimetric analysis (TGA) was carried out (Mettler Toledo, TG-850) usually in the temperature range of 30 °C - 450 °C at a heating rate of 2 $°C.min^{-1}$ in air. Typically using 25 mg of the sample in solid form mounted on a porcelain boat.

1.6.3 X-ray photoelectron spectroscopy

X-ray photoelectron spectroscopy (XPS) was carried out with ESCA LAB MKIV spectrophotometer (1 x 10^{-10} Torr vacuum) with X-ray source of Al Kα (1486.6 eV). The reported binding energies are relative to the 84.0 eV Au($4f_{7/2}$) level. Samples for XPS (solid substrates) were mounted on the stub using high vacuum compatible Ag paint and drying in a vacuum.

1.6.4 Atomic force microscopy

Atomic force microscopy (AFM) experiments were carried out using Digital instruments multimode head attached to Nanoscope-IV controller Tapping and contact (lateral force) mode imaging was carried out using standard etched Si or Si_3N_4 cantilevers respectively. The scanner was calibrated using a standard Pt coated Au grid with a pitch of 1 μm. The set up for C-AFM consists of the above mentioned AFM instrument and an external multimeter (Keithley 236) as the source and measurement unit for current-voltage characteristics. Commercial Si_3N_4 cantilever probes were made conducting by coating them with Au (300-400 nm) by physical vapor deposition. The bias ramp was applied to the conducting probe through the tip holder and the current was measured from a terminal connected to the floating substrate. The substrate was isolated from the scanner by proper insulation. The

electrical noise was minimized by proper grounding of the instrument. The I-V measurements were done in ambient conditions. The schematic of the set up and the instrument is shown in Figure 1.18.

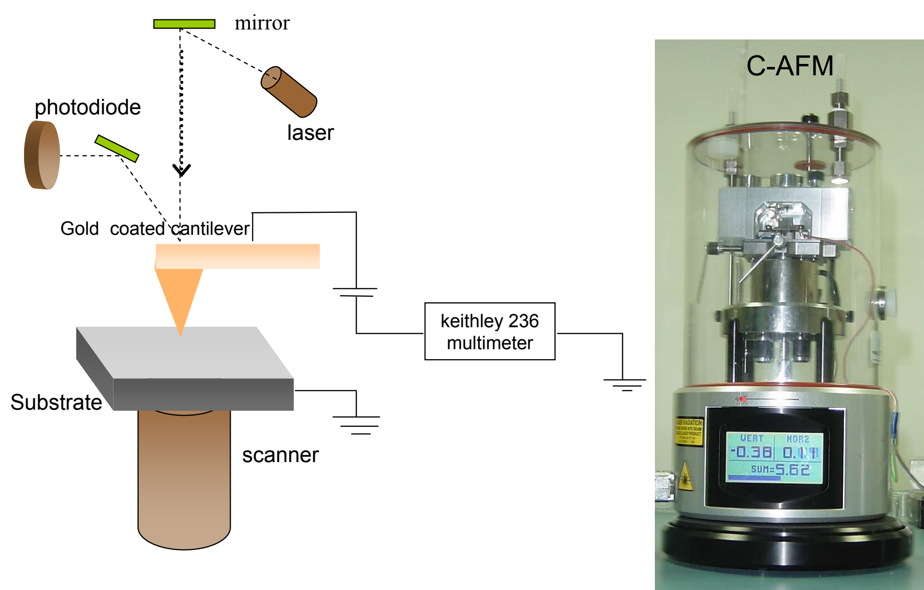

Figure 1.18: Schematic of C-AFM with the image of the instrument used, Multimode, Veeco.

1.6.5 Transmission electron microscopy

Transmission electron microscopy (TEM) measurements were carried out with a JEOL-3010 instrument operating at 300 kV ($\lambda = 0.0196$ Å) and electron diffraction (ED) patterns were collected at a camera length 20 cm (calibrated with respect to the standard polycrystalline Au thin film). Samples for TEM were prepared by depositing a drop of the nanomaterial (scraped from the substrate) on a holey carbon copper grid, allowing it to dry in a desiccator overnight.

1.6.6 Profilometric measurements

The film thickness was measured using a Wyko NT1100 (Veeco, USA) optical profiler (OP) and using a Stylus profiler Dektak 6M (Veeco, USA). In OP, the PSI mode was employed with a field of view and objective lens magnifications as 1X and 20X respectively.

1.6.7 Raman Measurements

Raman measurements were performed using LabRAM HR apparatus (Horiba, USA) with an excitation wavelength of 632.8 nm and 5 mW.cm^{-2}. Signal accumulation was performed for 10 s with a spot size of $\sim$1 μm. For temperature dependent SERS, a Linkam cryostage TMS-650 (U.K.) was used.

1.6.8 Scanning electron microscopy and related techniques

Scanning electron microscopy (SEM) was performed using a Nova NanoSEM 600 equipment (FEI Co., The Netherlands). Energy dispersive spectroscopic (EDS) mapping was performed using EDAX Genesis V4.52 (USA) attached to the SEM column. The EDS mapping was performed at 10 kV (energy window, 10 eV) with a beam current of 1.1 nA, the dwell time per pixel being 25 μs. STEM (scanning transmission electron microscopy) and low vacuum imaging were performed on the same instrument using a STEM and helix detectors respectively. The instrument is shown in Figure 1.19.

1.6.9 Electron beam Lithography

Electron beam lithography (EBL) was performed using a Nova NanoSEM 600 equipment (FEI Co., The Netherlands) (see Figure 1.18). Patterning was done un-

Figure 1.19: SEM instrument used for the study, Nova NanoSEM 600, FEI Co.

der high vacuum conditions, typically 10^{-6} Torr. The substrates used were usually Si or Au coated glass. Before patterning, the sample was well grounded to avoid any charging while patterning, as charging can broaden the patterned feature. The patterns were created using a e-beam write software available with the instrument. The e-beam energy was varied between 5-30 kV. For fine structures, higher kVs were employed whereas for larger area patterning, lower kVs were preferred. The patterning was performed in parallel mode. The beam current was varied between 91 pA to 24 nA. The dwell time, i.e., exposure time per pixel was varied from 0.1-50 μs. Number of passes was varied between 1-16000.

1.6.10 Optical spectroscopy techniques

UV-visible spectra were recorded using a Perkin-Elmer Lambda 900 UV/vis/NIR spectrophotometer. The photoluminescence (PL) spectra were taken with different excitation wavelength from the spectroflurometer. PL was measured on Perkin-

Elmer LS55 Luminescence spectrometer.

Fourier transform infrared measurements were done using a Bruker IFS66v/s spectrometer with a resolution of $\sim$2 cm^{-1}.

1.6.11 Physical vapor deposition

Au metal (99.99% pure) was physically deposited by resistive heating using 12" vacuum coating unit, (12A4D, HindHivac system, Bangalore) under 10^{-6} Torr vacuum. In order to fabricate gap electrodes, thin carbon fiber served as a mask.

1.6.12 I-V measurements

Conducting Ag paint was used for electrical contacts. An external multimeter (Keithley 236) served as the source and measurement unit for current-voltage characteristics. I-V ramp was carried out generally for $\pm$5 V with a delay time of 100 μs between data points. The current compliance was generally set at 80 μA.

1.6.13 SiO_2 overlayer on Si substrates

For nanocircuit fabrication, oxidized Si wafers with oxide thickness 150 nm were used. Freshly etched Si substrates were heated at 900 °C under flowing oxygen. The thickness of the oxide was measured using Stylus profiler, after etching away a portion in HF for step creation.

CHAPTER 2

Polystyrene as a zwitter e-beam resist

Summary*

The zwitter resists are popular, as they allow patterning with either positive or negative tone. The resist action of polystyrene (M_w, 2,60,000) towards electroless deposition of Au on Si surface following cross-linking by exposing to a 10 kV e-beam, has been investigated. Following development of the patterned resist, Au metal deposition was achieved by the electroless plating method from a solution consisting of 0.1 mM potassium tetrachloroaurate in 5 M hydrofluoric acid. The evolving nature of the resist towards the electroless process was studied as a function of the e-dosage. With a low dose of electrons (21 μC.cm^{-2}), the exposed regions inhibited Au metal deposition from the plating solution due to cross-linking - typical of the negative resist behavior of polystyrene, with metal depositing only on the unexposed (bare) Si surface. Upon increased e-dosage (160 μC.cm^{-2}), however, Au deposition took place even in the exposed regions of the resist, thus turning it into a positive resist. Raman measurements revealed amorphous carbon present in the exposed region that promotes metal deposition. Further increase in e-dosage led successively to negative (220 μC.cm^{-2}) and positive (13,500 μC.cm^{-2}) resist states. These experiments have shown that the resist behavior of polystyrene with respect to electroless plating does depend on the extent of e-dosage, showing a zwitter behavior, negative to begin with. The zwitter action of polystyrene resist

*Papers based on this work have appeared in Bull. Mater. Sci. (2006) and Bull. Mater. Sci. (2008).

has been exploited to create line gratings with pitch as low as 200 nm and gap electrodes down to 80 nm .

2.1 Introduction

In electron beam lithography (EBL), electron resist plays an important role. As the technique is sophisticated and time consuming, it is usually used where high resolution patterns are desired. Although, EBL is used to generate very fine structures (<10 nm), it is limited to resists that are sensitive to e-beam. Materials which require very low e-dosages to bring chemical changes resulting in solubility contrast in given solvents are highly desirable as e-beam resists. Over the years, several chemical formulations, mostly polymers, have been tried out as e-resists. Upon e-beam exposure, a polymeric resist undergoes chain scission (positive resist) or cross-linking (negative resist) and the exposed regions exhibit enhanced (positive) or diminished (negative) solubility in a chosen solvent. Poly(methylmethacrylate) (PMMA) is being routinely used as a positive e-resist to produce reticular patterns with 1:1 isopropanol:methylisobutylketone as a developer [29]. Other examples include, PBS (polybutene-1-sulfone), EBR-9 (a copolymer of trifluoroethyl-chloroacrylate and tetrafluropropyl-chloroacrylate), ZEP (a copolymer of chloromethacrylate and methylstyrene) as well as polyphenol-based resists. Similarly, negative resists such as P(GMA-EA) - an epoxy copolymer of gycidyl methacrylate and ethylacrylate, also known as COP, CMS (a partially chloromethylated polystyrene), EPR (epoxidized novolac resist) as well as calixarene and its derivatives are being used to produce raised patterns. Interestingly, some resists exhibit a switching behaviour, from positive to negative or vice versa, upon prolonged exposure of the e-beam [30]. Zailer et al.[31] and Hoole et al.[32]

found PMMA behaving as a positive resist below a e-dose of 30 μC.cm^{-2} to change to a negative behavior upon an additional dose of $\sim$ 50 - 70 μC.cm^{-2}. Geis et al.[33] reported the positive and negative self-developing resist behavior of nitrocellulose on exposure of heavy ions (Ar^+). Tada et al.[34] and Robinson et al.[35, 36] have found the negative-positive tone resist behavior of derivatives of triphenylene and the patterns down to 10 nm in size. Seki et al.[37] have reported the positive-negative inversion of Si-based resist such as poly(di-n-hexylsilane) upon ion beam irradiation. Chen et al.[30] demonstrated the zwitter resist action of acrylic resins.

2.2 Scope of the Present Investigation

The present investigation pertains to a systematic study on the zwitter action of popularly known negative tone e-beam resist, polystyrene. A zwitter resist refers to a resist which, depending on the applied e-doses, can exhibit both positive and negative properties. A resist with simultaneous positive and negative capabilities of patterning will benefit the direct writing technology. There are few polymeric [30–37] as well as inorganic resists [38, 39] known to exhibit zwitter action. There is no report where the zwitter action of a resist is studied with respect to electroless metal deposition from a plating solution, wherein no external bias is applied [40, 41]. Here, the nature of carbon as a resist becomes crucial and dictates the metal deposition on the e-beam exposed regions. Raman measurements are carried out to confirm the nature of carbon in the polymer after e-beam exposure. The zwitter action of polystyrene with electroless deposition of metal, namely Au has been studied and the e-doses required to convert it from negative to positive tone resist have been estimated.

2.3 Experimental Details

Initially, Si substrates (n-doped, 4-7 Ω.cm) were cleaned by sonicating in acetone followed by doubly distilled water and were dried under flowing argon. Figure 2.1 is the scheme adopted to pattern Au using polystyrene. A 1% solution of polystyrene (M_w, 260,000) in toluene was spin coated at 3000 rpm on the substrate to form a thin film, which is exposed to e-beam at 10 kV. The e-beam exposed substrate is developed in p-xylene for 90 seconds and 2-propanol for 30 seconds and dried. The polymer patterned subjected to electroless deposition of Au in the plating solution consisting of 0.1 mM potassium tetrachloroaurate ($KAuCl_4$) in 5 M hydrofluoric acid (HF). After the metal deposition, the substrate was washed with doubly distilled water and dried under nitrogen. As shown in the scheme (Figure 2.1) the e-beam exposure was carried out in two ways. In the method 'a', a mask was used while exposing a broad scanning e-beam whereas in method 'b', a focussed pointed beam was employed to generate polymer patterns. Polystyrene of a higher molecular weight was preferred due to its enhanced sensitivity [42, 43]. EBL was performed using a Nova NanoSEM 600 equipment (FEI Co., The Netherlands) (see section 1.6 for details). The desired regions of the resist coated substrate was exposed to either a broad scanning e-beam while masking with a TEM grid or to a focussed pointed beam exposing pixel by pixel in programmed manner. After exposure to e-beam, the resist film was developed by dipping the substrate in p-xylene for 90 seconds and 2-propanol for 30 seconds [44] and dried under flowing argon. The unexposed regions were washed away leaving behind the cross-linked polymeric pattern. Thus exposed Si surface was deposited with Au by electroless method. The plating solution held in a teflon container. The film thickness was measured using a Wyko NT1100 (Veeco, USA) optical profiler (OP). The PSI mode

was employed with a field of view and objective lens magnifications as 1X and 20X respectively. AFM measurements were performed on a Digital Instruments Multimode head attached to a Nanoscope-IV controller (Veeco, USA). Standard etched Si cantilevers were used for the normal topography imaging in the tapping mode. Energy dispersive spectroscopic (EDS) mapping was performed using EDAX Genesis V4.52 (USA) attached to the SEM column. Raman measurements were carried out on the exposed resist using a LabRam equipment with a He-Ne laser source (631.8 nm) and a spot size ∼1 μm.

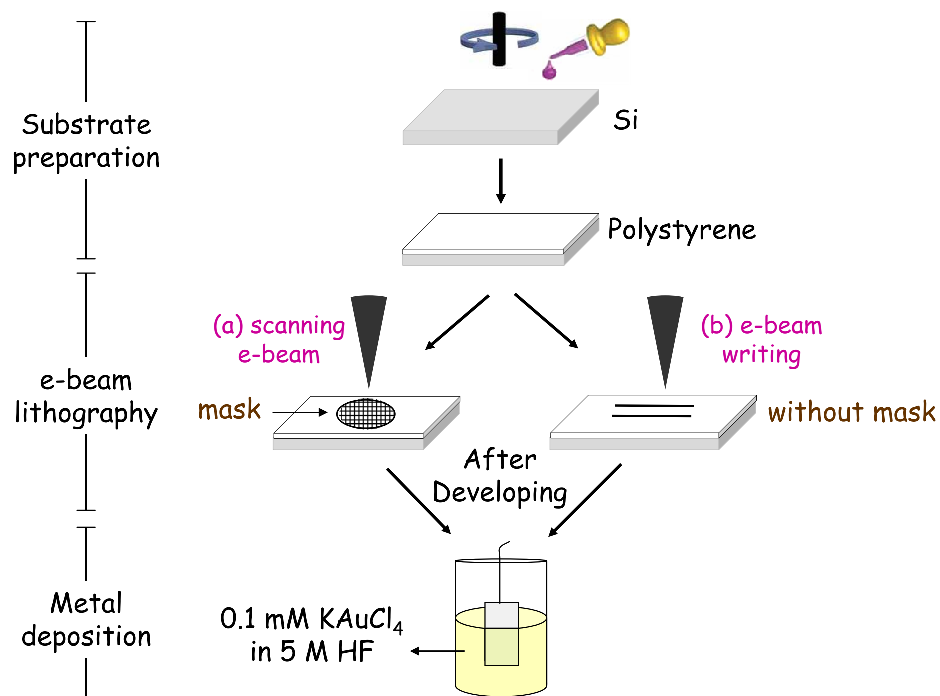

Figure 2.1: Schematic of the procedure adopted for electron beam lithography (EBL). Polystyrene coated substrate was patterned with (a) a broad scanning e-beam with mask or (b) a focussed pointed e-beam. The e-beam exposed substrate was developed and Au metal was deposited by electroless method.

2.4 Results and Discussion

Prior to patterning, a detailed study on electroless deposition of Au on Si surface has been carried out. In Figure 2.2, the topography of the electrolessly deposited Au film obtained using plating solution of 0.1 mM $KAuCl_4$ in 5 M HF for 30 minutes is shown. The deposited film is granular and the particulate appear agglomerated into islands measuring a few hundreds of nanometers. The thickness of Au film on Si surface has been studied under the given concentration of plating solution as a function of deposition time. Figure 2.3a shows that the rate of deposition, as measured by OP, varies proportionally with time. During the first hour, the deposition is at the rate of 1.03 $nm.min^{-1}$ and at longer durations, there is almost an order of magnitude rise, 9.04 $nm.min^{-1}$. It is interesting to note that this change of behavior in the film coincides with oriented growth of the film becoming polycrystalline, as revealed by XRD measurements shown in Figure 2.3b. The rms roughness values obtained from contact AFM also exhibit a similar trend, implying that a change in the rate of deposition owes much to the increased roughness from polycrystallinity. Insets in the Figure 2.3, show the profilometric images of the film after 30 and 90 minutes in the plating solution resulting in thicknesses of 29 nm and 365 nm respectively.

In order to improve the texture, the film was subjected to annealing at elevated temperatures of 250 °C. In Figure 2.4, are shown AFM and diffraction measurements after annealing at 250 °C for 12 hours. The deposited granular film(see Figure 2.2) after annealing(Figure 2.4a) improved the surface topography, the particles measuring $\sim$35 nm appear closely packed. The corresponding XRD pattern shown in Figure 2.4b, shows intense peak at 2.295 $\AA$ corresponding to Au(111) plane with no other peaks suggesting the oriented film.

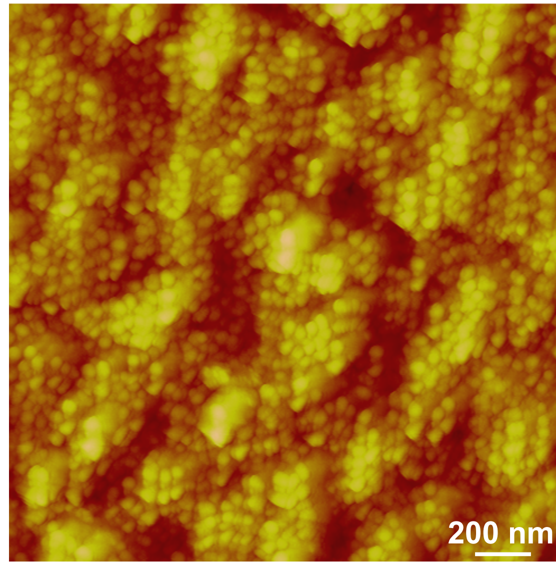

Figure 2.2: Tapping mode AFM image electrolessly deposited for Au film using plating solution of 0.1 mM $KAuCl_4$ in 5M HF and deposited for 30 minutes).

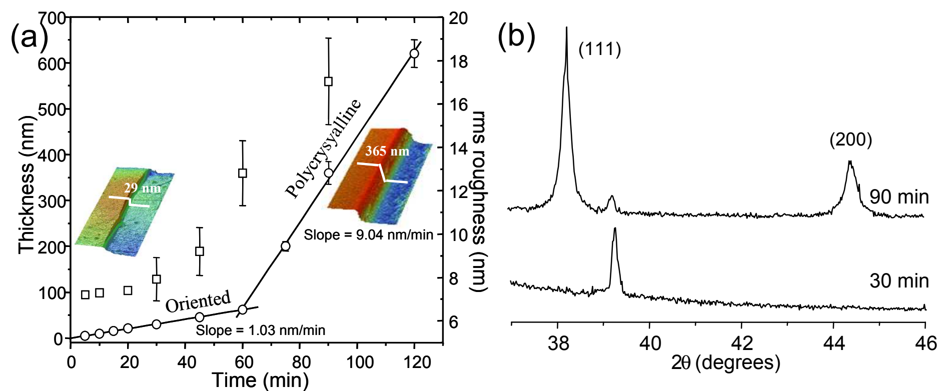

Figure 2.3: (a)Variation in the thickness of the films (circles) as a function of time in the plating solution (0.1 mM $KAuCl_4$ in 5M HF). The variation in the rms roughness values (squares) estimated from 2 x 2 μm^2 area using AFM, is also shown. Insets showing the profilometric images on 30 and 90 minutes deposited film. (b) XRD pattern of Au film obtained for 30 and 90 minutes.

The electroless plating of Au has been carried out in conjunction with polystyrene film on Si, patterned with varying e-dosages at 10 kV beam energy. Figure 2.5 shows the SEM images of the e-beam exposed, developed and Au plated surfaces. Figure 2.5a contains an image of a region (11 x 13 μm^2) seen with a dark contrast that

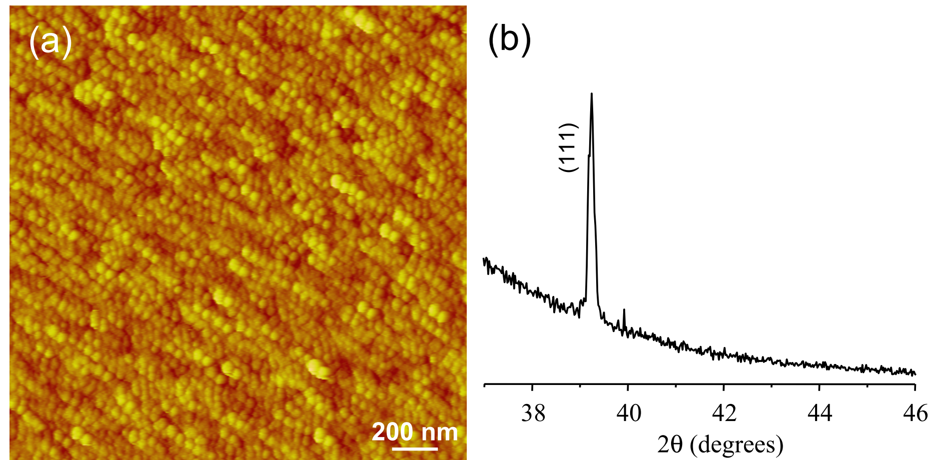

Figure 2.4: (a) Tapping mode AFM image obtained for Au film after annealing at 250 °C for 12 hours and (b) The corresponding XRD pattern.

was exposed with 21 μC.cm^{-2}, resulting in cross-linking of the polymer resist. The region surrounding the dark square is relatively bright and accordingly, the EDS spectrum (also shown in the Figure 2.5a) showed the presence of Au metal. In contrast, the EDS spectrum from the dark region showed only the presence of carbon. Thus, the cross-linked region inhibits the metal deposition, while the surrounding region contained unexposed resist that got washed away during developing thus exposing Si surface for metal deposition. This result reinstates the known negative resist behavior of polystyrene [42, 43]. For convenience, the Au/Si region (in Figure 2.5a) has been denoted as 0 state and the cross-linked region as 1(N) state where, in anticipation of several states of the resist, 1 stands for the first state with N representing the negative behavior.

In Figure 2.5b is shown a region (250 x 220 μm^2) of the substrate exposed with an increased dosage of 160 μC.cm^{-2} followed by electroless plating. Although electron exposed region is discernible, the contrast between the two regions is considerably less compared to that in Figure 2.5a. Accordingly, the EDS measurements showed the presence of Au metal in both the regions. Clearly, with an e-dosage of

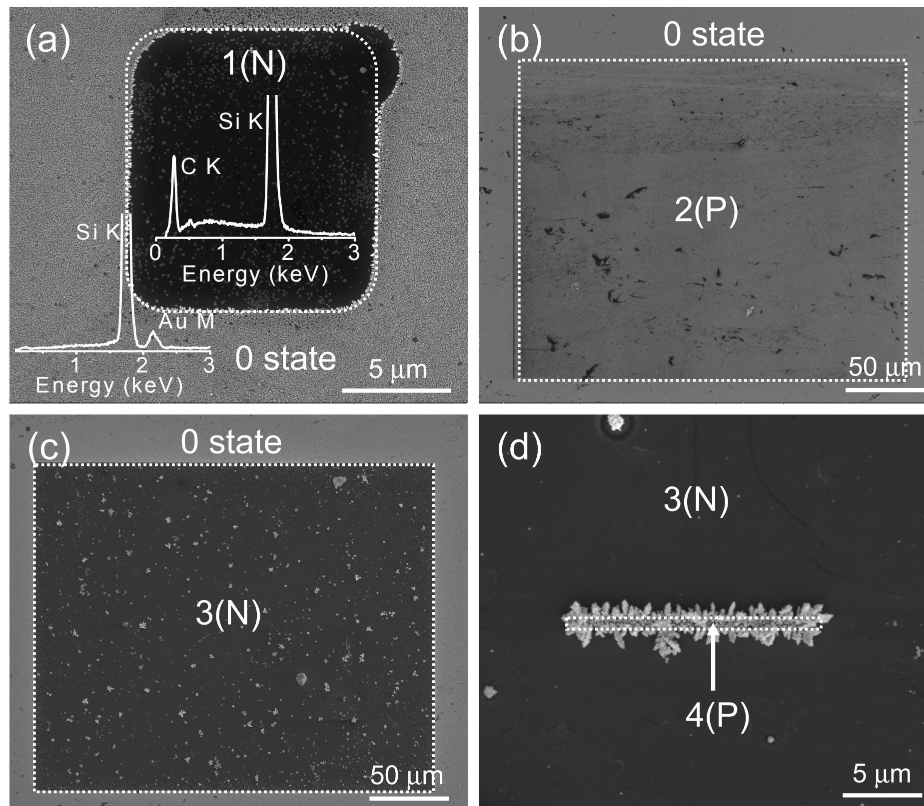

Figure 2.5: SEM images of the patterned substrate. The dashed line marks the region subjected to e-beam exposure. (a) 11 x 13 μm^2 region dosed with 21 μC.cm^{-2}. The EDS spectrum from the outside region shows the presence of Au metal, while that from inside shows only carbon, (b) 250 x 220 μm^2 region with a dosage of 160 μC.cm^{-2}, (c) 250 x 220 μm^2 region dosed with 220 μC.cm^{-2} and (d) further dosed with 13500 μC.cm^{-2} in the center (15 μm line). Here, P and N denote the positive and negative tone behavior of the polystyrene resist while the numbers indicate the successive states.

160 μC.cm^{-2}, the polymer reached a state beyond cross-linking and allowed metal uptake from the plating solution. This second state has been denoted as 2(P), P representing the positive resist behavior.

When the e-dosage was increased to 220 μC.cm^{-2} (Figure 2.5c), interestingly, the metal uptake in the exposed region is negligible somewhat resembling the case in Figure 2.5a. With the increased e-dosage to 220 μC.cm^{-2}, the polymer switches its behavior to negative tone that is denoted as 3(N) state. A narrow line region

within the 3(N) region was exposed to 13,500 μC.cm^{-2} at 30 kV that perhaps removed the resist altogether allowing the metal uptake in the exposed Si region. This may be denoted as 4(P) state.

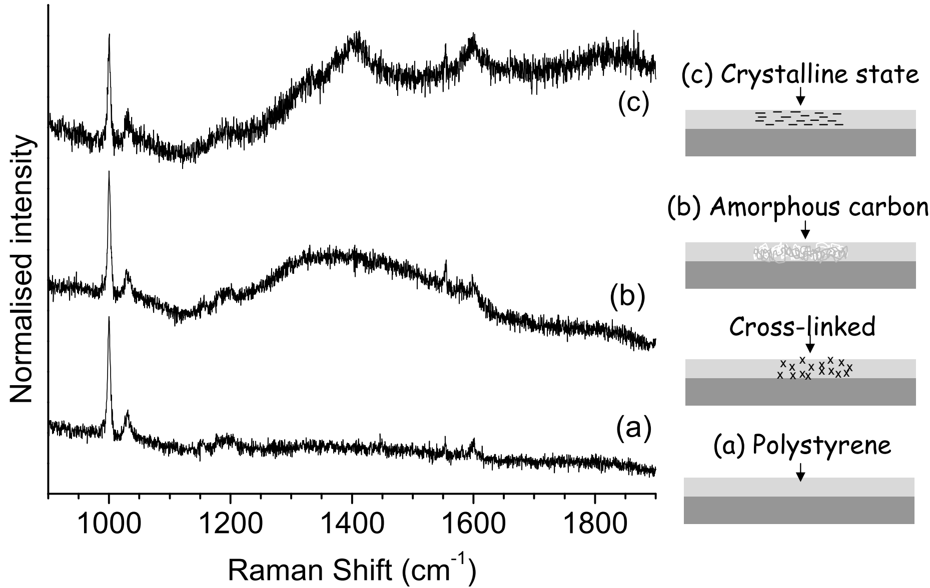

Figure 2.6: Raman spectrum of polystyrene in (a) the pristine form, (b) 2(P) state and (c) 3(N) state. Schematic showing the nature of carbon obtained for different e-dosage

More insight into the resist behavior particularly of the 2(P) and 3(N) states, was obtained by carrying out Raman measurements. Figure 2.6 shows the Raman spectra in the range of 900 - 1900 cm^{-1}, obtained for the different states corresponding to different e-beam dosages. The bands at 999 and 1020 cm^{-1} are arising from C-C ring deformation [45]. In spectrum 'a' from the pristine polymer film, one observes a small band around 1585 cm^{-1} corresponding to ring C-C stretching, more of sp^2 nature. The spectrum 'b' from the 2(P) region (see Figure 2.6b) contains in addition, a broad band centered around 1350 cm^{-1}. This may be a signature of disordered carbon that is likely to form when a cross-linked polymer is further exposed to the e-beam [46]. Incidentally, amorphous carbon on Si pro-

motes Au uptake, thus making it effectively a positive resist. The spectrum ‘c’ from the 3(N) region shows two relatively sharp bands at 1380 and 1560 cm^{-1}. These may be taken to represent more crystalline state of the carbon [47] resulting from an excessive e-dosage. Crystalline carbon on Si being relatively inactive in the electroless process, gives rise to a negative tone behavior.

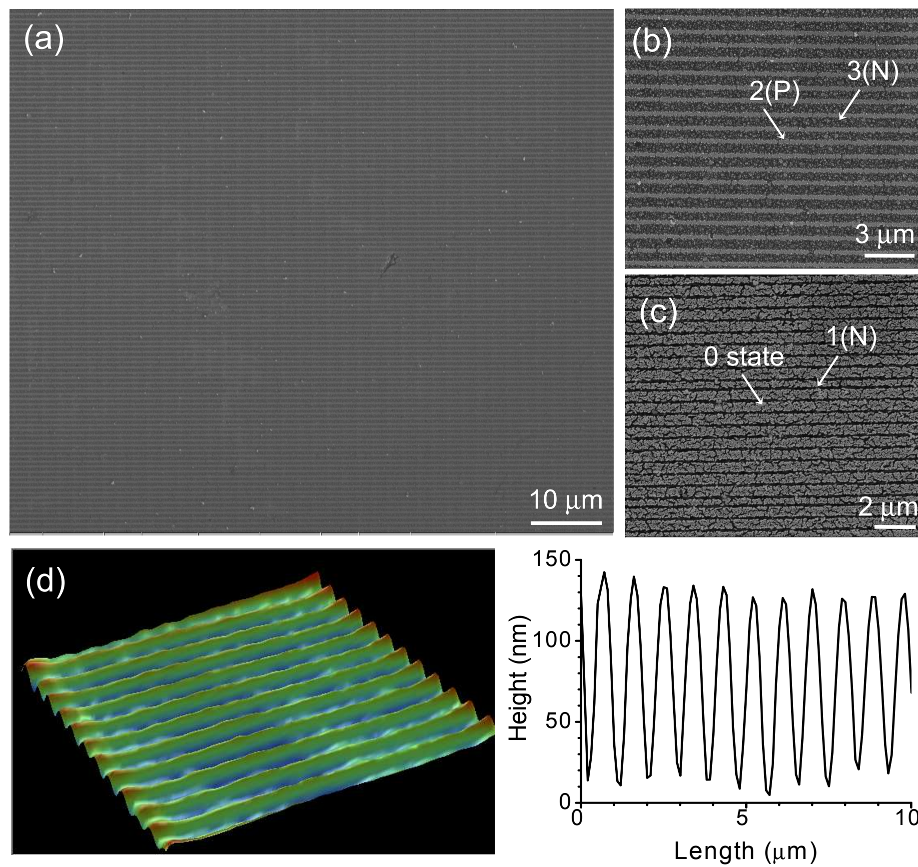

Figure 2.7: (a) Line grating pattern generated by switching between 2(P) and 3(N) states with its magnified image in (b). (c) Line grating pattern generated by switching between 0 and 1(N) states. (d) An optical profilometric image of the gratings in (a) with the measured profile.

Having understood the zwitter action of the polystyrene resist in electroless plating, appropriate conditions for patterning Au on Si have been obtained. In Figure 2.7 are shown Au line gratings obtained by electroless Au deposition on a

developed pattern from the direct write method. Figure 2.7a contains line gratings with a pitch of 750 nm obtained using e-beam energy 5 kV, with e-dosage of 200 μC.cm^{-2}. Under the given exposure conditions, Au lines of 230 nm width are created with the 2(P) behavior of the resist with the gap (500 nm) corresponding to the 3(N) state. By decreasing the e-beam dosage to 10 μC.cm^{-2}, one can also create periodic line spacings ($\sim$ 120 nm) in the 1(N) state, with metal depositing in between (300 nm, 0 state) (see Figure 2.7c). In Figure 2.7d is shown a 3D profilometric image of the gratings along with the height profile. The measured pitch from the profile is found to be is 780 nm, similar to that seen in Figure 2.7b. With the direct write method, patterning over a few mm square areas has been achieved.

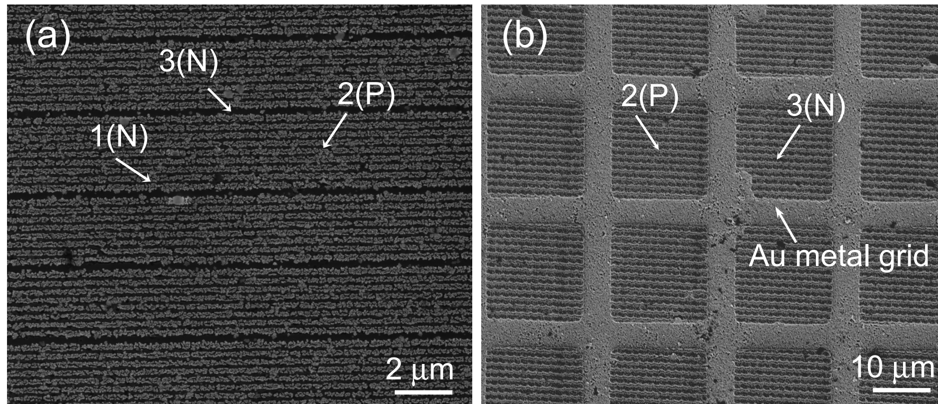

Figure 2.8: A modulated grating pattern generated (a) with two different pitches, 350 nm and of 2.9 μm and (b) using a TEM Cu grid as an additional mask during e-dosage.

The zwitter behavior of the polystyrene resist can be extended to produce more complicated patterns. Figure 2.8 shows SEM images of such line gratings. The line grating structure in Figure 2.8a was obtained by first patterning the resist working between 0 and 1(N) states (similar to Figure 2.7c) followed by another exposure with a periodicity of 2.9 μm to result in the 3(N) state. Following the

development and metal deposition, the modulated structure shown in the figure emerges. In Figure 2.8b is shown a set of line gratings obtained working between 2(P) and 3(N) states (similar to Figure 2.7b) while additionally masking with a TEM Cu grid. The e-beam can also be programmed to create uniformly a 3(N) state in the exposed regions. An extended deposition in the plating solution (120 minutes) produced a well-defined metal grid structure on the substrate (Figure 2.9). A profile analysis revealed the depth of the wells to be $\sim$ 300 nm (Figure 2.9b). Such microwells may find applications in microfluidics.

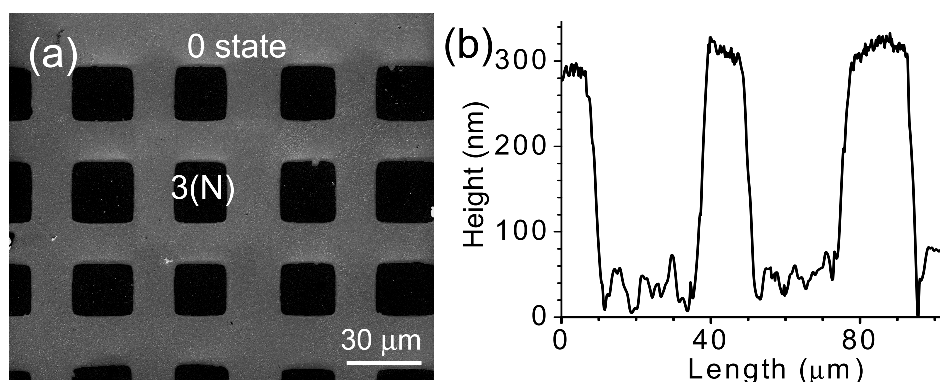

Figure 2.9: (a) Au metal wells generated by masking the resist film with a TEM Cu grid and exposing to a broad beam. (b) The height profile measured using profilometric image.

It may be noted that the metal deposited electrolessly is in intimate contact with Si substrate. Thus, a combination of EBL and electroless process can potentially produce nanometric patterned electrodes for electric field induced embossing and pattern transfer. In Figure 2.10 is shown how quick line scans followed by developing and electroless Au deposition can produce gap electrodes. The SEM image in Figure 2.10 contains a 2 μm gap electrode extending across a 2 mm long Si substrate, bisecting it into two macroscopic contact pads. The inset in Figure 2.10 depicts the image of another set of electrodes with $\sim$150 nm separation. Importantly, such gap electrodes can be produced in a matter of few seconds. Such

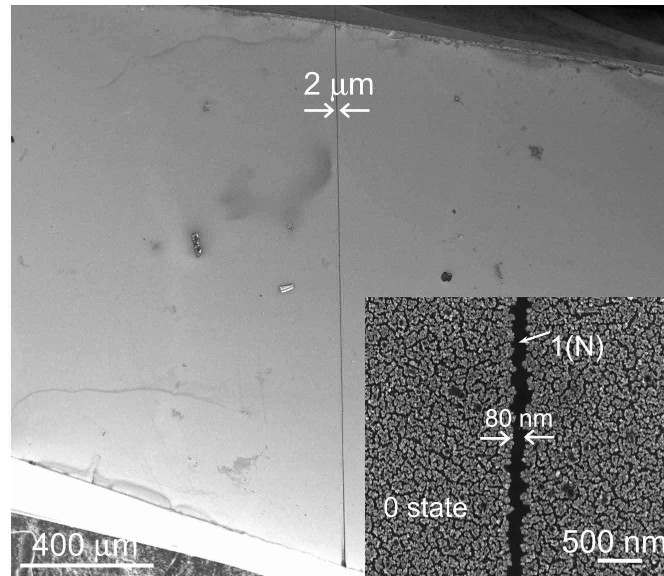

Figure 2.10: A 'quick circuit' generated by drawing a single line with the e-beam across Si substrate coated with the resist. Au deposition following developing of the resist produced a gap of ∼2 μm. Inset shows a gap electrode with a separation of ∼80 nm.

gap electrodes is more useful while studying high conducting nanomaterials, since ambient oxide beneath acts as an insulating layer.

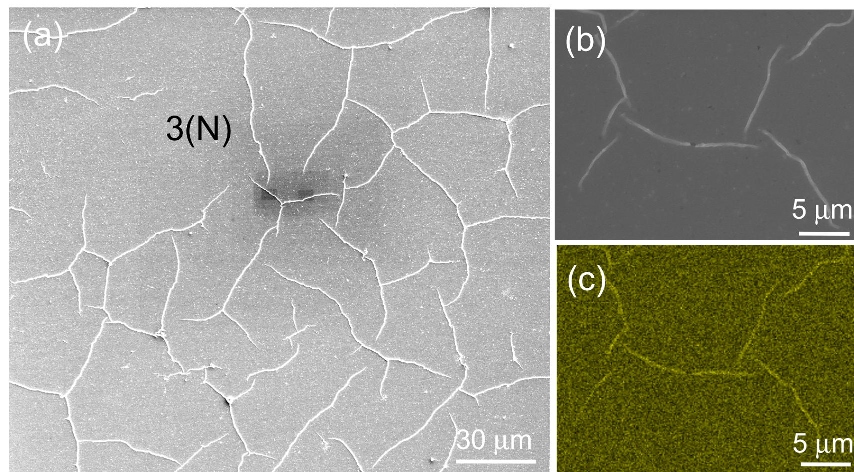

Figure 2.11: A cracked resist film obtained upon prolonged exposure to the e-beam. (a) Crack propagation showing an interesting pattern. Au M line EDS mapping of a selected region (b), shown in (c) reveals Au deposition in the cracked regions.

The chosen resist being very sensitive to the e-beam, an extended exposure may

sometimes lead to cracks in the film exposing the Si underneath. The SEM images in the Figure 2.11 show interesting crack propagation across the resist film. In Figure 2.11a, the bright lines represent the cracked regions, filled with Au during plating. A EDS mapping of the Au M line confirmed this observation (see Figure 2.11b and c).

2.5 Conclusions

The zwitter resist action of polystyrene during electroless deposition of Au has been demonstrated. While increasing the e-dosage from 20 μC.cm^{-2} to several thousand units, polystyrene initially behaving as a negative resist, exhibits successive positive and negative states. Raman measurements on the e-beam exposed regions showed that the cross-linked polymer forms amorphous carbon at dosages of $\sim$150 μC.cm^{-2} and becomes crystalline upon further dosage (above 200 μC.cm^{-2}). The amorphous state of carbon allows electroless metal deposition while the crystalline state inhibits, thus bringing out the zwitter action of the resist. Line gratings have been generated with the lowest pitch value being 200 nm. Similarly, gap electrodes with separation below 100 nm have been fabricated. More intricate patterns such as microchannels have also been produced for applications in microfluidics.

CHAPTER 3

$Ag(PPh_3)_3NO_3$ - polystyrene blend as an e-beam resist to produce conducting Ag nanocrystal patterns

Summary*

Silver triphenylphosphine was blended with polystyrene, a well-known negative tone e-beam resist and patterned using e-beam. Presence of Ag in the patterned region was confirmed by EDS analysis. TEM showed the formation of small Ag nanoparticles in the matrix in the polymer. The reduction of Ag precursor was monitored by XPS. UV-VIS absorption studies showed a broad peak at 464 nm, typical of surface plasmon absorption by Ag nanoparticles. These nanoparticles were covered with a carbon shell (∼25 nm) as seen using STEM. C-AFM measurements showed the high conducting nature of the patterned blend, clearly due to presence of Ag nanoparticles. Under the given conditions, the minimum resistance achievable was similar (8.3 kΩ) independent of the e-beam energy, but the dwell time required was different; higher the beam energy, lesser was the required dwell time. Confocal fluorescence studies showed embedded Ag nanoparticles in the carbon matrix to have fluorescence property.

*A manuscript based on this work is under preparation.

3.1 Introduction

Synthesis of functional nanomaterials in desired patterns is an important stage in device fabrication. In this context, UV or e-beam lithography based synthesis of patterned nanomaterials for active elements is a versatile method. Metal precursor containing polymer blends are good starting materials for this purpose, as the former produces active species under the lithography beam while the latter not only works like a resist but also provides the desired matrix. There are several reports in the last few years of preparing metal nanoparticles in polymer matrices. Eilers et al.[48] obtained telfon-Ag nanocomposite by evaporation of teflon and Ag foil on sapphire substrate and found the broadening of optical absorption indicating the formation of the blend. Peng et al.[49] were successful in synthesizing dispersed polyaniline (PANI)-Au composite particles by direct oxidation of aniline with the metal salt. Thus, the formed particles possessed a Au core encapsulated by PANI. The composite exhibited a broad 835 nm absorption indicating a strong electronic interaction between the core and the shell. Porel et al.[50] have synthesized Au and Ag nanoparticles in polyvinyl alcohol (PVA) matrix by heating to 100-170 °C for an hour and investigated the optical limiting capability of these nanoparticle-embedded polymer.

There are other studies where the blend contained well known resists such as poly(methylmethacrylate) (PMMA). Deshmukh and Composto [51] showed that the thermal decomposition of Ag precursor with PMMA at 185 °C leads to the formation of Ag nanoparticles and their enrichment at the surface. Basak et al.[52] have studied the electrical conductivity of thin films of PMMA dispersed with Ag nanoparticles. The composite was well conducting in dark while in presence of light, the conducting paths were destroyed. Mahapatra et al.[53] used a mixture of

PVA with Au and Ag metal precursors and obtained respective metal nanoparticles by exposing to a broad e-beam of 5-15 keV.

3.2 Scope of the Present Investigation

While there have been many studies on synthesizing metal nanoparticles in polymer matrices by blending prior to reduction of the metal precursor, there are no reports on their patterning. In this chapter, an investigation has been carried out on polystyrene, a negative tone e-beam resist, by blending it with an organic precursor of Ag, with the intention of producing metal composite consisting of Ag nanoparticles embedded in patterned polystyrene. $Ag(PPh_3)_3NO_3$ was chosen as a source of Ag metal as it is soluble in toluene to form a blend with polystyrene. The electrical properties of the blend before and after e-beam exposure has been studied in detail.

3.3 Experimental Details

The resist blend was prepared by mixing triphenylphosphine precursor of silver namely, $Ag(PPh_3)_3NO_3$ (6% by mol) with commercially available negative tone e-beam resist, polystyrene (M_w 2,60,000) in toluene. This blend was spin-coated at 3000 rpm on clean Si or ITO substrates. EBL was done using an e-beam writer available with Nova NanoSEM 600 equipment (FEI Co., The Netherlands) (see section 1.6 for details). An array of 10 x 10 μm^2 square regions was exposed to an electron dosage of 150 $\mu C.cm^{-2}$ at different beam energies 5-30 kV. Electron exposure was done at with constant e-dosage and varying internal parameters such

as dwell time and number of passes. The substrate was then developed in p-xylene and 2-propanol for 60 and 30 seconds respectively. Further, the patterned substrate was dried under flowing argon. A schematic of patterning of the Ag precursor blended with polystyrene is shown in Figure 3.1.

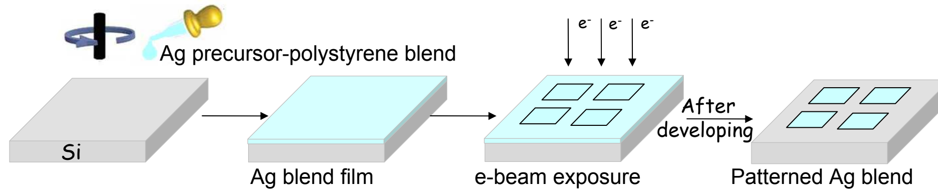

Figure 3.1: Schematic showing the procedure adopted for patterning Ag precursor-polystyrene blend using EBL. Step 1 - Spin coating of the $Ag(PPh_3)_3NO_3$-polystyrene blend on a Si substrate. Step 2 - EBL patterning the blend film and Step 3 - Developing the patterned substrate in p-xylene and 2-propanol for 90 and 30 seconds respectively.

Energy dispersive spectroscopy (EDS) analysis was performed at 10 kV (energy window, 10 eV) with a beam current of 1.1 nA, the dwell time per pixel being 30 μs using an EDAX Genesis (Mahwah, USA), attached to the SEM column and scanning transmission electron microscopy (STEM), was also performed with the same instrument. UV-Vis spectra were recorded using a Perkin-Elmer Lambda 900 UV/vis/NIR spectrophotometer. In order to perform transmission electron microscopy (TEM), a holey carbon grid was drop coated with the blend and patterned. High-resolution TEM imaging was carried out with a JEOL-3010 equipment operating at 300 kV. The core-level Ag(3d) spectra were measured using a VG scientific ESCALAB MK-IV spectrophotometer with an x-ray source of Al Kα (1486.6 eV). C-AFM measurements were done employing a Digital Instruments Multimode head attached to a Nanoscope-IV controller (Veeco, USA) and an external multimeter (Keithley 236) as the source and measurement unit for current-voltage characteristics. Commercial Si_3N_4 cantilever probes from Olympus

(Japan) were made conducting by coating them with Au (300-400 nm) by using a physical vapor deposition. The bias ramp was applied to the conducting probe through the tip holder and the current was measured from a terminal connected to the floating substrate. The electrical noise was minimized by proper grounding of the instrument. The Raman and fluorescence spectra were collected on a specialized instrument with 514.5 nm Ar ion laser from a spot size <1 μm. The laser had a maximum power of 40 mW. The back-scattered light was collected by a 100X objective lens and sent to the spectrometer through a multimode fiber. A super-notch filter placed in the path of the signal effectively cuts off the excitation radiation. The signal was then dispersed using a 150 grooves/mm grating and the dispersed light was collected by a Peltier cooled charge coupled device (CCD). For spectral imaging, the desired area was partitioned into 10,000 squares (an imaginary 100 X 100 matrix drawn over it), with each square representing a sampling point and consequently a pixel for the image. Typical signal acquisition time at each pixel of the image was 0.1 s. Confocal imaging was carried out using 514.5 nm excitation with a photomultiplier tube (PMT) detector. The signal was collected in a back-scattering geometry without using the notch filter. For confocal fluorescence imaging, a super-notch filter was employed.

3.4 Results and Discussion

Electron beam patterns were drawn using the silver triphenylphosphine nitrate-polystyrene blend as a resist are shown in Figure 3.2. As polystyrene is a negative-tone resist, the e-beam exposed regions get cross-linked and remain after developing while rest of the polymer gets washed away. Figure 3.2a shows the SEM image of a $\sim$500 nm gap electrode patterned with the blend resist with an e-dose of 150

μC.cm^{-2} employing 5 kV beam. The EDS mapping carried out at Ag M and C K lines clearly showed the presence of Ag and C in the patterned regions (Figure 3.2b and c). This observation proved successful entrapment of Ag in cross-linked polystyrene. In Figure 3.2d, another example of SEM image of the line patterns drawn, ~150 nm wide and ~300 nm apart obtained with 30 kV beam at 150 μC.cm^{-2} is shown.

The effect of the electron beam exposure on the chemical nature of the blend was examined employing XPS (Figure 3.3). For this purpose, a large area of 3 x 3 mm^2 was patterned using 5 kV at 150 μC.cm^{-2}. The Ag(3d) and C(1s) core-level spectra before and after electron exposure in Figure 3.3a and b respectively. Prior to the e-beam exposure, the Ag(3d) spin-orbit doublets are observed at 366.9 and 374.4 eV respectively (Figure 3.3a) and after e-dosage, at 367.2 and 373.1 eV respectively(Figure 3.3b) and area under the curves being nearly same. Ag(3d) peak becomes broad and shifts to lower binding energy, indicating the reduction of Ag. The emergence of Ag^0 state is clear. The C(1s) region, prior to exposure (Figure 3.3a) was found to contain two features at 284.6 and 287.8 eV due to graphitic and sp^3 carbon respectively, the latter being more intense. After e-beam exposure (Figure 3.3b), position of the main peak shifted to 285.3 eV and with a lower intensity peak at 286.6 eV. This shift indicates the formation of more graphitic carbon in comparison to hydrocarbon before exposure to e-beam.

From XPS studies, it is clear that the reduction of Ag species takes place upon exposure to e-beam. This has been further confirmed by UV-Vis absorption measurements as shown in Figure 3.4. The surface plasmon peak seen at 464 nm for the e-dosed sample is a clear indication of the formation of Ag nanoparticles which is absent in the case of unexposed blend [48]. TEM and STEM images of e-beam exposed sample are shown in Figure 3.5. In Figure 3.5a shows the presence of

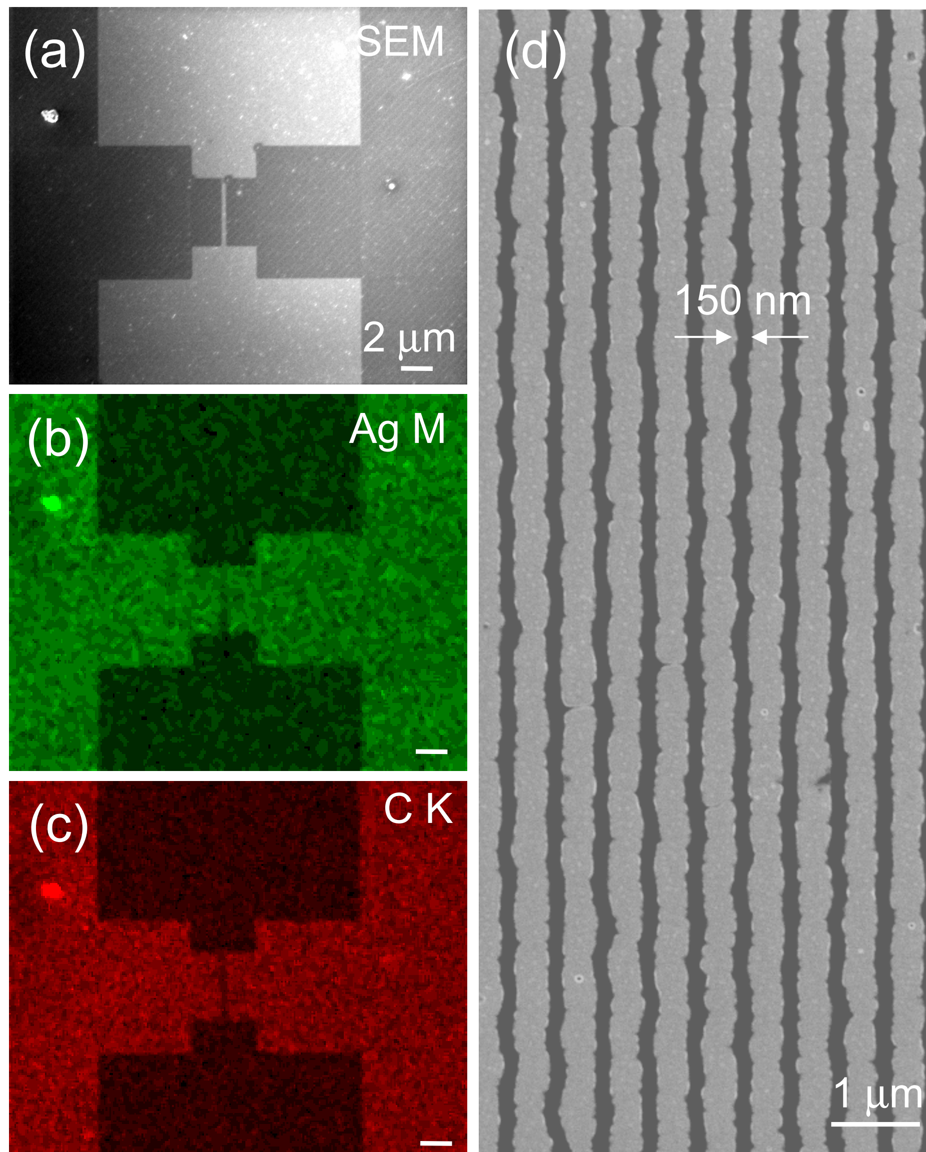

Figure 3.2: (a) SEM image after e-beam patterning. EDS maps of the patterned regions, b) Ag M and c) C K lines and (d) Fine lines of 150 nm wide and spaced 300 nm apart. The lines are slightly wavy.

nanoparticles sized 20-50 nm in the carbon matrix. High-resolution imaging in the top inset shows dark features corresponding to metal center, thus the bigger features are indeed made up of finer particles of 3-5 nm. Electron diffraction pattern in the bottom inset clearly shows sharp spots corresponding to (111) and (200)

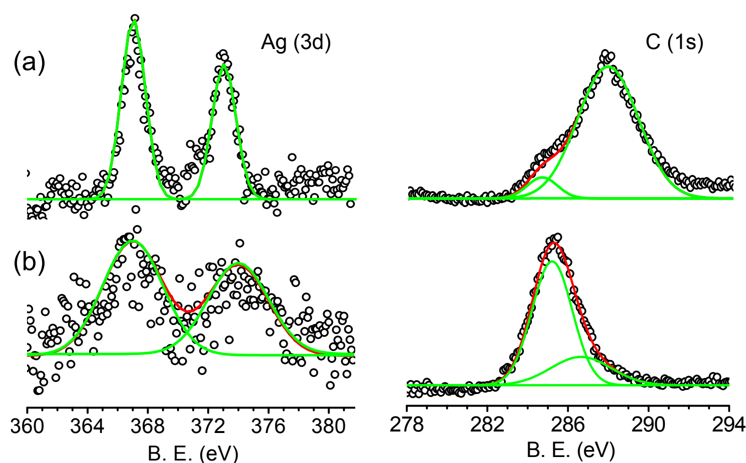

Figure 3.3: Ag(3d) and C(1s) core level spectra of the blend before (a) and after (b) electron exposure. The relatively higher spread in data points in (b) is due to poor signal strength as e-beam exposed region was limited to 3 x 3 mm^2)

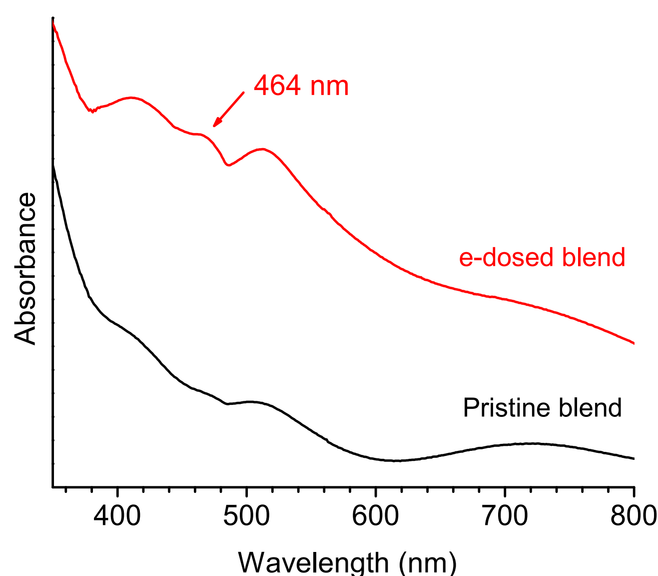

Figure 3.4: Optical absorption spectra of the blend before and after e-dosage. The feature marked with an arrow represents surface plasmon absorption from Ag nanoparticles.

diffraction planes, implying good crystallinity of the Ag nanoparticles. STEM image shown in Figure 3.5b, brings out particulate arrangement within an aggregate. Each Ag core is seen to be covered by a carbon shell of thickness of 25 nm.

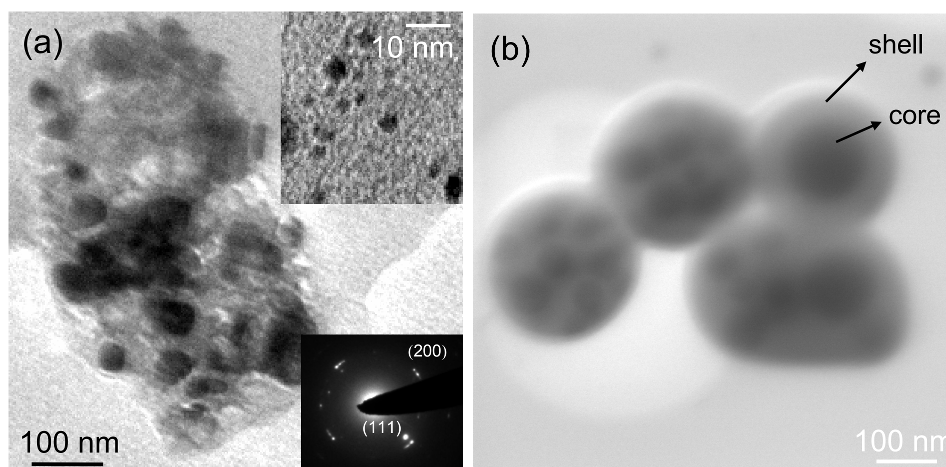

Figure 3.5: (a) TEM image of the e-beam exposed cross-linked blend showing formation Ag nanoparticles. Inset showing high-resolution image (top) and corresponding electron diffraction (bottom). (b) STEM image of the Ag nanoparticle aggregate. The core and shell regions are marked.

The resist blend exposed to e-beam was further examined under confocal fluorescence and Raman microscopy (Figure 3.6). The intensities of the desired portion of the spectra collected over all the pixels were compared by ScanCTRL Spectroscopy Plus Version 1.32 software, to construct a color-coded image. Regions coded yellow represent the pixels where the signal (used for mapping) is maximum, the minimum being represented with red/black colors. The dark regions of the sample indicate that there is absorption of the incident radiation. As shown in Figure 3.6a and b, the confocal image constructed based spectral intensity (Rayleigh being a major component) and the confocal fluorescence images, emission intensity collected using a notch filter, are complimentary to each other, meaning that the regions from which the sample absorbs the excitation radiation (shown as dark regions in the confocal image) are the regions from which light is emitted as seen in the confocal fluorescence image. This may be interpreted as the absorption by the embedded Ag particles or species at the nanoparticle surface and their subsequent emission. In view of the significant absorption manifested at these locations, it is likely that

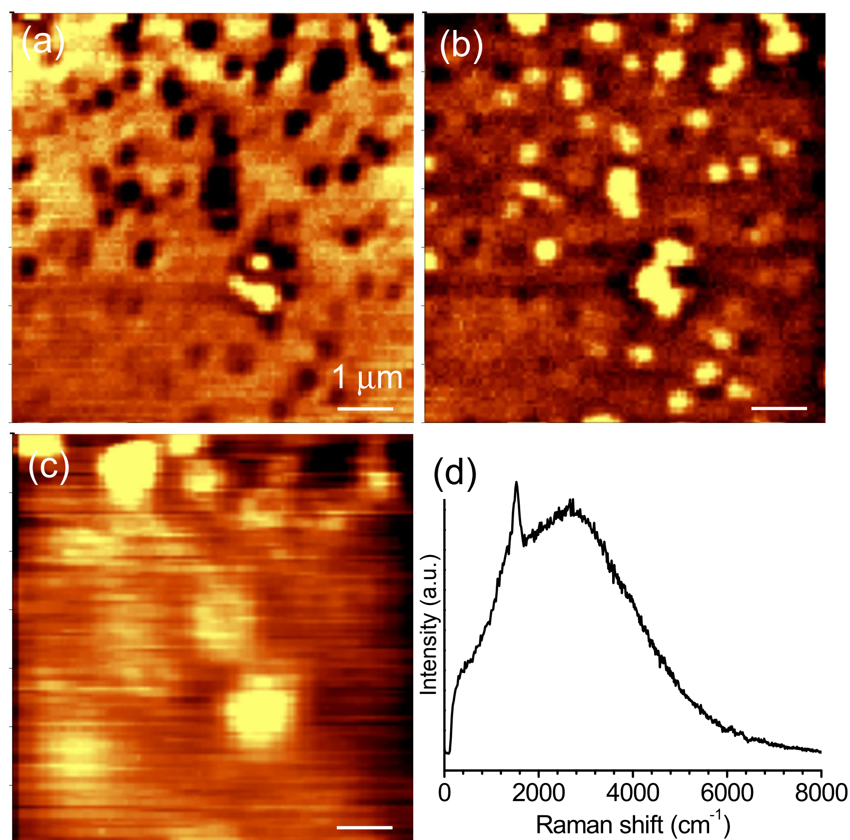

Figure 3.6: (a) Confocal image of Ag nanoparticles in cross-linked polystyrene matrix. Fluorescence (b) and Raman (c) images from the same region. (d) Fluorescence Raman spectrum from the the same region.

the black spots are due to nanoparticles, which is in agreement with the TEM and STEM investigations as shown in Figure 3.5. The plasmon absorption of large Ag particles fall in the region of the excitation radiation [48]. The emission spectrum collected from a spot on the sample using the Raman set-up is shown in Figure 3.6d. The creation of carbonaceous species by e-beam irradiation may be confirmed from Raman peak at 1524.cm^{-1}, which is in accordance with the Raman spectra of amorphous carbon [46]. From the above studies, it is clear that e-beam exposure of $Ag(PPh_3)_3NO_3$-polystyrene blend brings about reduction of Ag^{1+} to form Ag nanoparticles (3-5 nm) covered with a thin layer of amorphous carbon, making it

suitable for electrical transport.

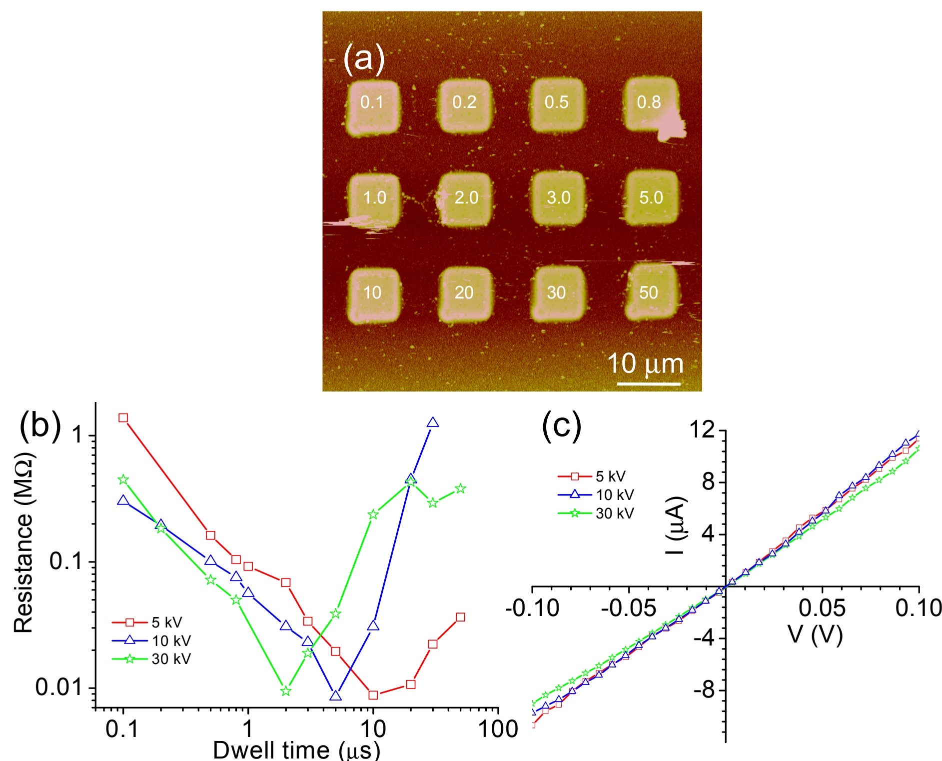

Figure 3.7: (a) AFM image of an array of square islands of the Ag nanoparticles polystyrene composite. (b) Plot of resistance versus dwell time for different islands patterned at 5, 10 and 30 kV. (c) I-V measurement made using C-AFM showing the lowest resistance obtained with different kVs.

In order to evaluate conducting property of the precursor blend, an array of 4 x 4islands of size 10 x 10 μm^2 was patterned. C-AFM was performed on individual islands. A typical AFM image is shown in Figure 3.7a. The islands marked 1-12 have been given constant electron dosage of 150 $\mu C.cm^{-2}$ while varying the dwell time (0.1 - 50 μs) and the number of passes (16000-8). Constant e-dosage was chosen to study the time dependent behavior of Ag metal formation. Figure 3.7b is plot of resistance versus variation in dwell time for the blend patterned at different kVs namely, 5, 10 and 30. At a given kV, the resistance is in the range of MΩs at lower dwell times. On increasing the dwell time, the resistance initially

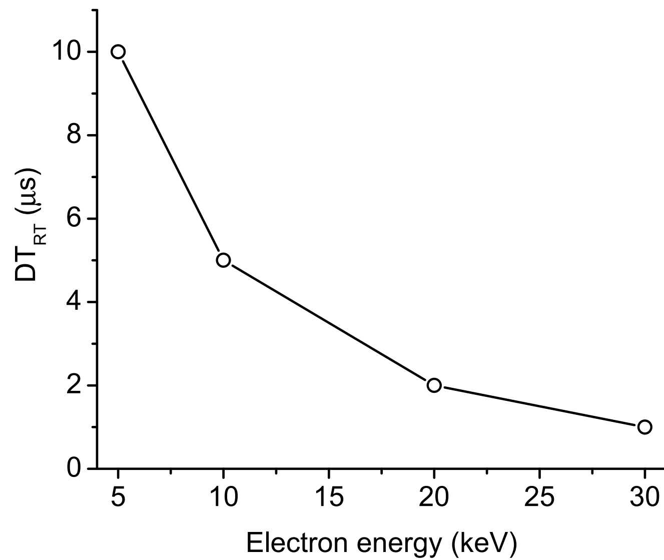

Figure 3.8: (a) AFM image of an array of square islands of the Ag nanoparticles polystyrene composite. (b) Plot of resistance versus dwell time for different islands patterned at 5, 10 and 30 kV. (c) I-V measurement made using C-AFM showing the lowest resistance obtained with different kVs.

dropped to 10 kΩ and increased. This trend was observed irrespective of the kV employed. I-V data corresponding to the least resistance state of the patterned blend is shown in the Figure 3.7c. Independent of the e-beam energy employed, all I-V curves are linear with resistance of 8.3 kΩ.

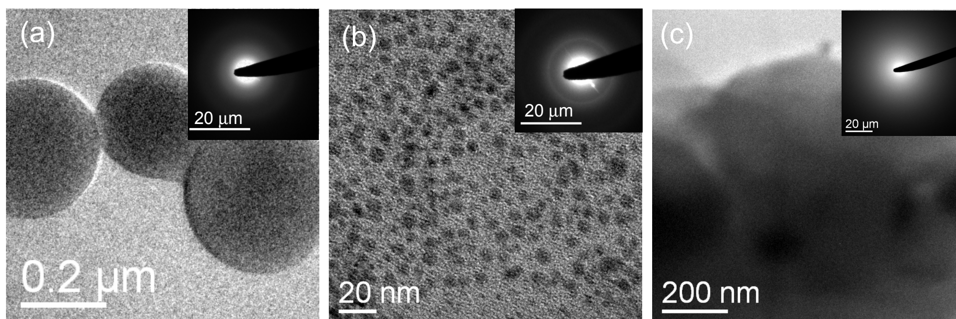

Figure 3.9: TEM images with corresponding ED patterns shown in the inset for patterned regions at 30 kV with different dwell time (a) 0.5, (b) 1 and 50 μs.

In Figure 3.8, a plot of dwell time at which lowest resistance was observed for different kVs is plotted as a function of kVs. For 30 kV, it is around 1 μs whereas for

5 kV, it is 10 μs at each pixel. It is observed that higher the beam energy, shorter is the dwell time required to generate the most conducting pattern.TEM studies were carried out on the 30 kV patterned regions to find the nature of Ag nanoparticles. Figure 3.9a shows some evidence of the nucleation of Ag nanoparticles at a lower dwell time (0.5 μs), whereas at 1 μs, well formed Ag nanoparticles are seen in the carbon matrix (Figure 3.9b). ED pattern shows distinct rings, confirms overall crystallinity nature of the Ag nanoparticles. Clearly, this emphasizes the observed trend in the resistance with the dwell time (Figure 3.8b). On further increasing dwell time to 50 μs, TEM image obtained, is almost devoid of Ag nanoparticles (Figure 3.9c) and ED pattern shown in the inset, appears featureless and diffused.

It is interesting that such a low doping of Ag could enhance the conductivity of polystyrene by several orders of magnitude, thus making the blend a potential electron resist material. The effect of dwell time is evident. At a given beam energy, it requires an optimal dwell time for Ag nanoparticles to nucleate and grow. Lesser dwell time, even though repeated for more times, proves insufficient in inducing Ag nanoparticle growth. Higher dwell time, seem to chip of metallic species leaving behind only carbon.

3.5 Conclusions

Electron beam patterning of Ag,using silver triphenylphosphine and mixing it with a well known negative tone e-beam resist, namely, polystyrene is demonstrated. On exposure to e-beam, reduction of Ag takes place resulting in a core-shell structure with carbon made available from polystyrene forming the shell. The size of the nanoparticles is anywhere between 5-50 nm which also forms bigger aggregates. The reduction of Ag was also confirmed by XPS measurements which

showed presence of Ag^0 peak at 367.2 and 373.1 eV while UV-Vis spectra showed a peak around 464 nm, from Ag nanoparticles. The Ag-carbon core shell structures exhibit fluorescence property. C-AFM studies carried out on the patterned blend supported the formation of metallised polystyrene with the resistivity in the range of $10^{-3}\Omega.m$, typical of metal nanoparticle blends. This study has shown how, by exploiting negative resist behavior of polystyrene in combination with the ability of Ag to reduce under e-beam, conducting patterns of polystyrene doped with Ag nanoparticles can be obtained.

CHAPTER 4

Pd hexadecanethiolate as a direct write e-beam resist and electrical characterization of patterned Pd nanowires

Summary*

Pd hexadecanethiolate is shown to serve as a negative-tone direct-write e-beam resist to produce nanopatterns down to 30 nm. The resist action has been realized with e-dosages of 2 - 300 μC.cm^{-2} at 5 kV e-beam energy. The written patterns do not deviate much from the precursor composition, while a post-treatment at 230 °C in air produced metallic Pd nanowires with residual carbon less than 10% and resistivity close to the bulk value, a desirable property of interconnects in nanocircuitry. The as-written patterns, contain small nanocrystals (<5 nm) in a hydrocarbon matrix, which upon annealing aggregate to form well-connected networks of larger nanocrystals (5 -15 nm), thus giving rise to metallic conductivity. Thus, the study demonstrates the use of Pd hexadecanethiolate as a direct write e-resist requiring low e-dosages, yet leading to highly conducting Pd nanopatterns.

*A paper based on this work has appeared in ACS Nano (2008) and another manuscript has been recently submitted.

4.1 Introduction

The advancement in nanoelectronics crucially depends on the ease with which circuit elements based on nanomaterials can be fabricated reliably. This in turn has led to an intense activity in the literature reporting innovative materials and methods to achieve below 100 nm fabrication [54, 55]. An important and widely pursued aspect of nanopatterning is related to casting metals into submicron features and their exploitation as interconnects [56–58], solder in nanocircuitry [59, 60], sensor elements [61], or as catalysts to grow nanotubes [61] and nanorods [63]. Charged particle beam based lithography techniques, electron beam (EBL) and focussed ion beam (FIB), are well suited particularly when it comes to making an interconnect from a contact pad [56–58] or soldering a nanoobject to it [59, 60]. In this context, direct write EBL or FIB methods employing metal precursor based resist coatings [12, 64, 66–72] or chemical vapor deposition under a focussed beam (EBID [73–79] and FIBID [73, 80–84]) find immense use. Tailor made metal organic complexes and salts [64, 66, 67] as well as nanoparticle sols [68–72] have been employed as thin film resists to generate nanopatterns of Au [64, 68–70], Ag [70] Pd [66, 71, 72], Co [67], Ni [67] and Mo [67] in direct write methods. Vapor phased precursors such as carbonyls of W [34, 73], Fe [74] and Cr [74] as well as organometallic complexes of Pt [75–77, 81–84] and Au [58, 76, 77] have been used in beam induced depositions of the respective metals. One of the pertinent problems in such studies is that the written patterns invariably contain impurities from the starting precursor such as carbon and Ga, as much as 40% or even higher [68, 71, 75–77, 82–84]. Often, a post treatment procedure is adopted to remove the organic impurity and improve the relative metal content [66, 68, 71, 75–77, 80, 81], albeit an overall loss of metal because of high temperature. Besides, the conducting property of the metal

patterns is generally poor, the resistivity being usually a few orders of magnitude higher than the bulk [66, 68–77, 80–84], except in cases where non-carbon based precursors have been developed to obtain patterns with resistivity values few times the bulk [78, 79].

Pd nanopatterning has attracted considerable attention in the recent times [66, 71, 72, 85–87]. Yan and Gupta [84] obtained 5 μm lines of Pd metal by UV photodissociating an acetate film while Lee et al.[85] exposed a patterned PMMA resist to the acetate vapor and produced Pd patterns down to 500 nm. By blending PMMA with Pd precursor, metallised polymer patterns have been obtained by both UV and EBL [86]. Microcontact printing has been used to create Pd metal nanostructures on substrates [87]. Stark et al.[66] have patterned palladium acetate with e-beam to get fine structures of Pd and studied electrical property. Reetz et al.[71] fabricated Pd and Pd/Pt nanostructures by exposing films containing corresponding cluster species to high dosages, $\sim$0.2 C.cm^{-2} at 120 kV. These studies [66, 71, 72] report resistivity values which are few orders magnitude higher than that of the bulk Pd, mainly because of the carbon impurity.

4.2 Scope of the Present Investigation

Previous EBL work using thiolate species as a source of metal (Au) was restricted to functionalized polymeric resists [64, 65], presumably due to processing difficulties, as alkanethiolates of most metals, once formed, cannot be easily solubilized. In contrast, Pd alkanethiolates are soluble in common organic solvents and can be self-assembled repeatedly. Besides, alkanethiolates have high metal content(20-40%) and possess low thermolysis temperatures. The present study is an investigation on the possibility of using Pd hexadecanethiolate as a direct write

e-beam resist. It is expected that upon e-beam exposure, the hydrocarbon chains would undergo cross-linking and form defects which reduces their solubility in solvents. Mild heating should then make thiol desorb to produce the metallic species. This aspect was investigated by fabricating a nanowire circuit with patterned Pd hexadecanethiolate as the active element.

4.3 Experimental Details

Pd hexadecanethiolate, $Pd(SC_{16}H_{35})_2$, was synthesized by mixing equimolar ratio of $Pd(OAc)_2$ (5.0 mmol) in toluene (7 ml) and hexadecanethiol (5.0 mmol) in toluene (3 ml), and the resulting mixture was stirred vigorously. Following the reaction, the solution became viscous, and the yellow color deepened to orange-yellow. The obtained thiolate was washed with methanol and acetonitrile to remove excess thiol and finally dissolved in toluene to obtain a 0.1 mM solution [88]. For EBL, Si substrates (n-doped, 4-7 Ω.cm) were cleaned by sonicating in acetone and doubly distilled water and dried under flowing argon. The resist film was made by spin-coating the thiolate solution at 2000 rpm. EBL was performed using a Nova NanoSEM 600 instrument (FEI Co., The Netherlands) (see section 1.6 for details). The e-beam energy employed for patterning was 5 kV. For nanocircuit fabrication, oxidized Si wafers with oxide thickness 150 nm were used. Au metal film of 70 nm thickness was thermally deposited with a gap of 20 μm between the two electrodes. An external multimeter (Keithley 236) served as the source and measurement unit for current-voltage characteristics. Thickness measurements were performed using a Stylus profiler Dektak 6M (Veeco, USA). Energy-dispersive spectroscopy (EDS) analysis was performed with an EDAX Genesis instrument (Mahwah, NJ) attached to the SEM column. The EDS mapping was performed at 10 kV (energy window,

10 eV) with a beam current of 1.1 nA and the dwell time per pixel being 25 μs. Transmission electron microscopy (TEM) measurements were carried out with a JEOL-3010 instrument. Fourier transform infrared measurements were done using a Bruker IFS66v/s spectrometer with a resolution of $\sim$2 cm^{-1}. UV-Vis spectra recorded in reflective mode using a Perkin-Elmer Lambda 900 UV/vis/NIR spectrophotometer. Scanning photoelectron microscopy (SPEM) with in-situ direct or indirect (600 °C) heating of the specimen was performed at the ESCA microscopy beamline of Sincrotrone Trieste S.C.p.A. di Interesse Nazionale, Trieste, Italy. Photoemission spectra of the nanopatterned regions were measured with a spot size of about 150 nm, 500 eV photon energy and 0.3 eV energy resolution which allows us to probe the core level chemical shifts. Photoelectrons were detected by a hemispherical electron energy analyzer, under a fixed angle of 30° with respect to the surface plane, with an acceptance cone width of 7°. The analyzer was equipped with a stripe detector for the simultaneous energy-dispersive detection in 48 channels. In the imaging mode, the sample is scanned by piezo-motors, yielding 48 images according to the number of parallel detection channels. Alternatively, in micro-spectroscopy mode, the analyzer energy set point is swept in order to take X-ray photoemission spectra from a well defined, microscopic spot on the surface. Deconvolutions of the XPS spectra were performed using Origin 6.0 software with FWHM for Pd and S species as 1.5 and 0.9 respectively.

4.4 Results and Discussion

4.4.1 Thermolysis of Pd hexadecanethiolate

Thermolysis of noble or semi-noble metal thiolates leads to loss of the thiols molecules resulting in metallic nanoparticles [89–91]. This aspect was studied in detail by heating Pd hexadecanethiolate in air (Figure 4.1). Thermogravimetric data (TGA) showed a weight loss of 12% around 150 °C corresponding to solvent evaporation. At 250 °C, around 72% weight loss is observed corresponding to thiol desorption leading to metal species formation. Figure 4.2 presents XRD data following thermolysis of Pd hexadecanethiolate film done for 30 minutes performed at different temperatures ranging from 30 to 250 °C in air. The Pd hexadecanethiolate and Pd metal peak intensities are monitored as a function of temperature. At room temperature, intense peak due to Pd hexadecanethiolate species is seen at 44.41, 22.20, 11.10 and 5.5 $\AA$ corresponding to d-spacings (001), (002), (003) and (004) respectively. This is due to bilayer lamellar structure of Pd hexadecanethiolate [88]. No Pd metal peak intensity is seen at room temperature, indicating absence Pd^0 species. Peaks due to Pd thiolate species continued to be present till 180 °C but with reduced intensities. Thermolysing at 230 °C, resulted further reduction of the Pd thiolate peak intensities, indicating the desorption of thiol molecules, in accordance with the TGA data (Figure 4.1) and the peak broadened along with emergence of Pd metal species with peaks at 2.2455, 1.9443 and 1.3769 $\AA$ corresponding to Pd (111), (200) and (220) respectively (JCPDS 461043). At 250 °C, intensity of Pd metal peaks increased and there was no trace of thiol molecules.

Optical reflectance and FTIR spectroscopy studied of Pd thiolate film done at different temperatures are shown in Figure 4.3. The pristine film shows a broad

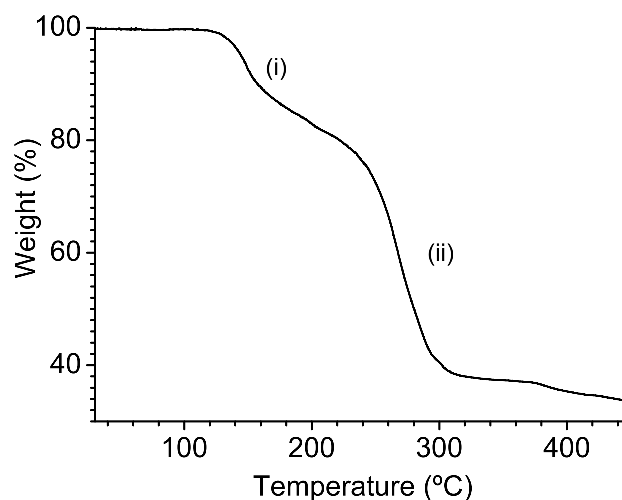

Figure 4.1: Thermogravimetric analysis on Pd hexadecanethiolate done in air. (i) loss of solvent and (ii) thiol desorption.

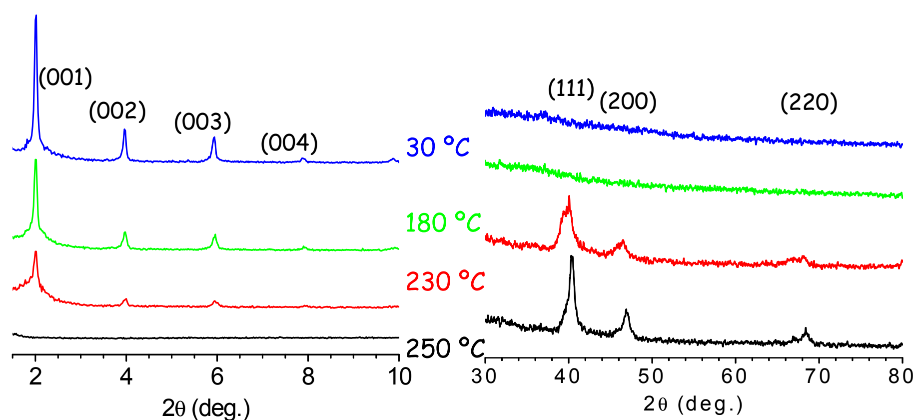

Figure 4.2: XRD pattern of Pd hexadecanethiolate thermolyed at different temperatures.

peak in the reflectance spectrum (Figure 4.3a) standing on a falling background. With the films subjected to increasing thermolysis temperatures, the peak gets weaker and the reflectance becomes increasingly uniform over the entire range of wavelengths, typical of metal films. The FTIR spectrum of the pristine film (Figure 4.3b) exhibits symmetric and antisymmetric methylene C-H stretching modes at 2848 and 2918 cm^{-1} respectively. After heat treatment at 180 °C, the bands

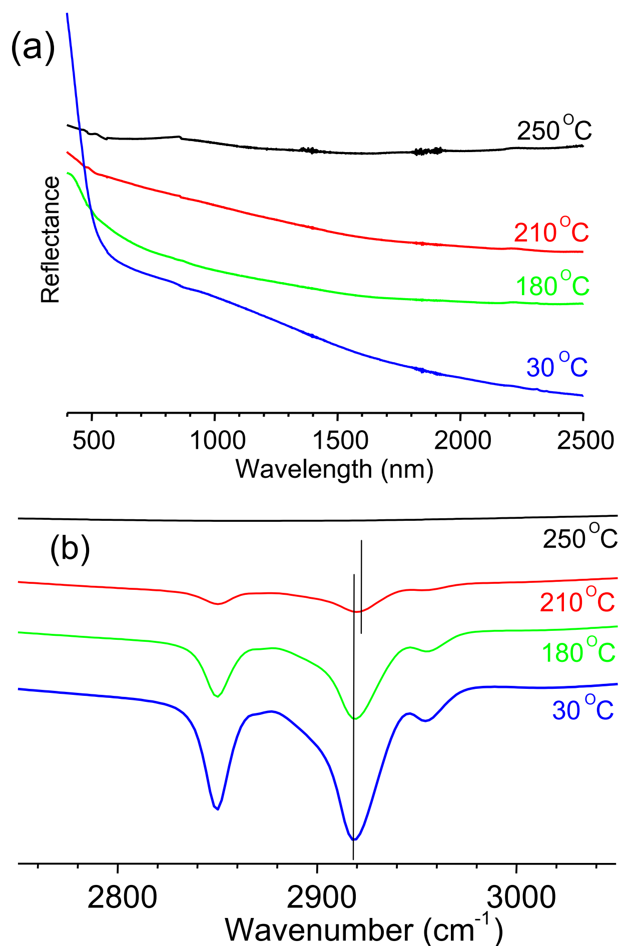

Figure 4.3: Optical reflectance (a) and FTIR (b) spectra recorded on a Pd hexadecanethiolate film after thermolysis in air for 20 minutes at different temperatures.

exhibit small positive shifts (∼5 cm^{-1}) accompanied by diminished intensity, both foretelling the occurrence of defects, particularly gauche defects in the hydrocarbon chains of the thiolate and desorption of thiol molecule. After thermolysis at 250 °C, there is no signature of the C-H bands in the IR spectrum (see Figure 4.3b).

TEM analysis carried out on the thermolysed Pd film is shown in Figure 4.4. The nanoparticles often deviated from the spherical morphology, some elongated or partially agglomerated. The size range is 5 - 20 nm (see Figure 4.4a). The high-resolution image in Figure 4.4b depicts lattice fringes from two nanoparticles where

one appears to be deformed in the middle. The d-spacing of 2.25 $\mathring{A}$ corresponds to d(111) of Pd metal.

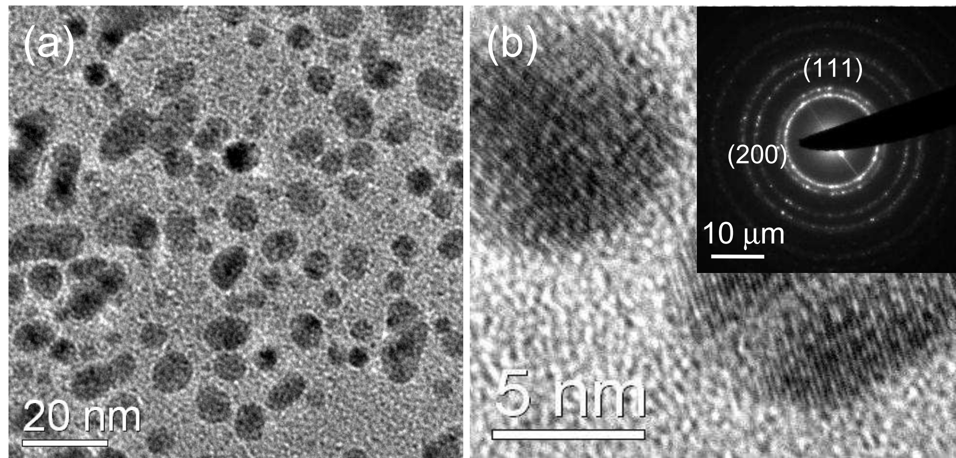

Figure 4.4: (a) TEM and (b) HRTEM images of thermolysed Pd hexadecanethiolate. Inset showing ED pattern.

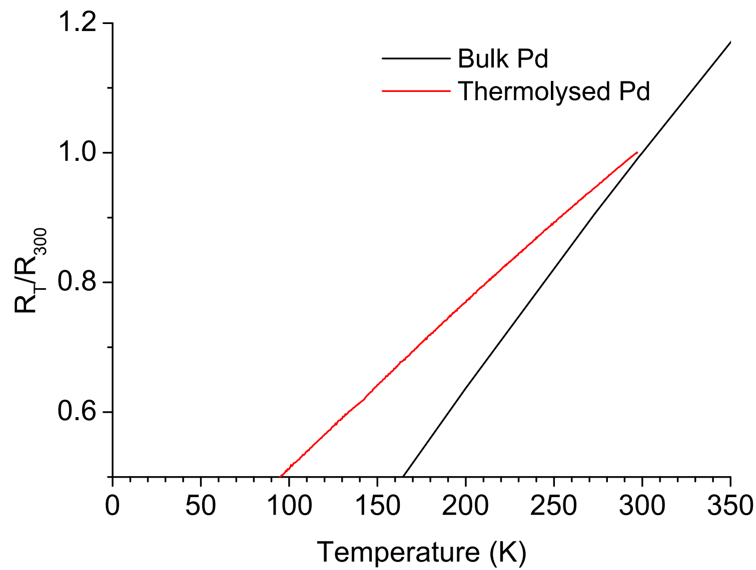

Figure 4.5: Four probe resistivity plot as a function of temperature for the thermolysed Pd film along with bulk Pd (from ref [92].

In order to determine the temperature dependent behavior, a four-probe measurement on a thermolysed Pd film (150 nm thick) deposited on glass substrate (see

Figure 4.5) was done. The variation with temperature is linear following classic Matthiessen's rule. The temperature coefficient obtained (0.00313579 K^{-1}) for the thermolysed film is nearly half that of the bulk (0.00572018 K^{-1}).

4.4.2 Electron beam writing on Pd hexadecanethiolate

Direct-write procedure for Pd hexadecanethiolate is simple, involving basically three steps (see Figure 4.6). A Pd hexadecanethiolate film was spin-coated on a Si substrate, patterned using a 5 kV e-beam at 135 $\mu C.cm^{-2}$ and developed in toluene for 10 seconds. The regions exposed to the e-beam remained on the substrate after developing (Figure 4.7), thus indicating the negative-tone resist behavior of the thiolate. Corresponding to the SEM image (Figure 4.7a) of the four square areas (6.5 x 6.5 μm^2), the energy-dispersive spectral (EDS) images obtained by mapping Pd L, C K and S K lines in Figures 4.7b-d show, as expected, the presence of Pd, C, and S, respectively, in the designated areas. The atomic Pd:C:S ratio obtained for the patterned regions, 21:71:8, agrees with the initial composition (19:69.8:11.2) of the unexposed resist, $Pd(SC_{16}H_{35})_2$, implying that the e-dosage causes only minimal change in the overall composition.

The sensitivity and contrast parameter for the resist has been calaculated by patterning at 5 kV with a beam current of 13 nA, squares of 10 x 10 μm^2 while gradually varying the e-dosage from 2 to 280 $\mu C.cm^{-2}$ (Figure 4.8). The patterned regions were quite smooth as the pristine itself, an important feature of a high-resolution resist (see inset of Figure 4.8). The thickness of the developed region, as measured using OP, is found to increase with the e-dosage, due to increasing resist action. With a minimum dosage of 2 $\mu C.cm^{-2}$, only about 7% of the original thickness is retained following developing in toluene, and this value gradually increased

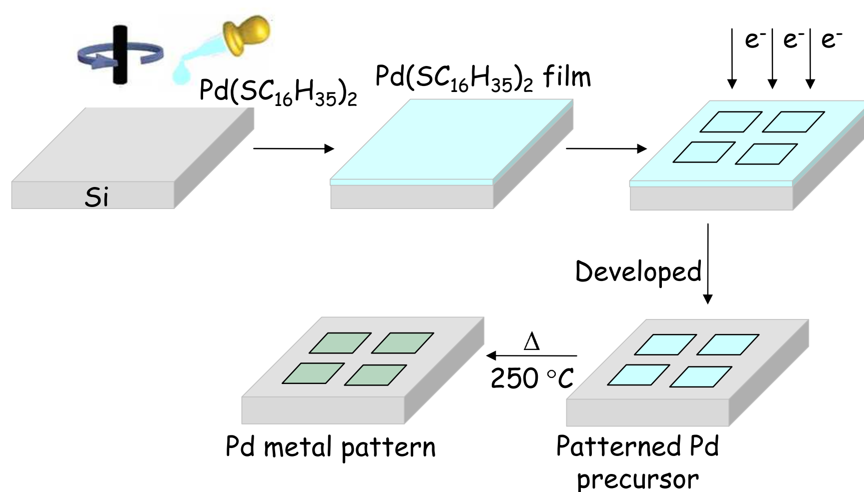

Figure 4.6: Schematic of procedure adopted of e-beam patterning of Pd thiolate.

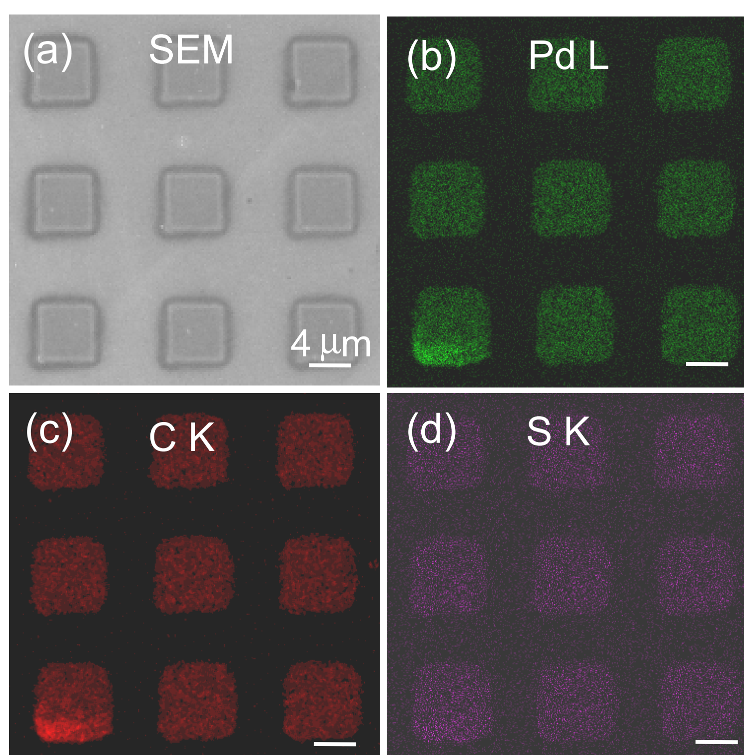

Figure 4.7: (a) SEM and EDS maps of (b) Pd L, (c) C K and (d) S K lines on the e-beam patterned regions.

to 85% beyond 150 μC.cm^{-2}. From the plot in Figure 4.8, it is possible to deduce the sensitivity of the resist, which is defined as the dose at which half the thick-

ness of the resist is preserved [93]. This value was found to be 42 μC.cm^{-2} for Pd hexadecanethiolate, which compared to other direct write resists is commendable. With such value of sensitivity, large areas can be patterned in short time as shown in Figure 4.9. In the literature, typical values for Pd patterning literature values being 10^3 and 10^5 μC.cm^{-2} from Stark et al.[66] and Reetz et al.[71], respectively. The resolution achievable with a resist is defined in terms of its contrast parameter, γ; higher the contrast, higher is the resolution. For negative resist,

$$\gamma_n = (log(d_0/d_c))^{-1} \tag{4.1}$$

where d_0 is the dose required to retain 100% of the resist material and d_i is the minimum dose at which resist action just begins [94] (see section for details). For Pd hexadecanethiolate developed in toluene for 10 seconds, the measured contrast value is 1.43 (see Figure 4.8).

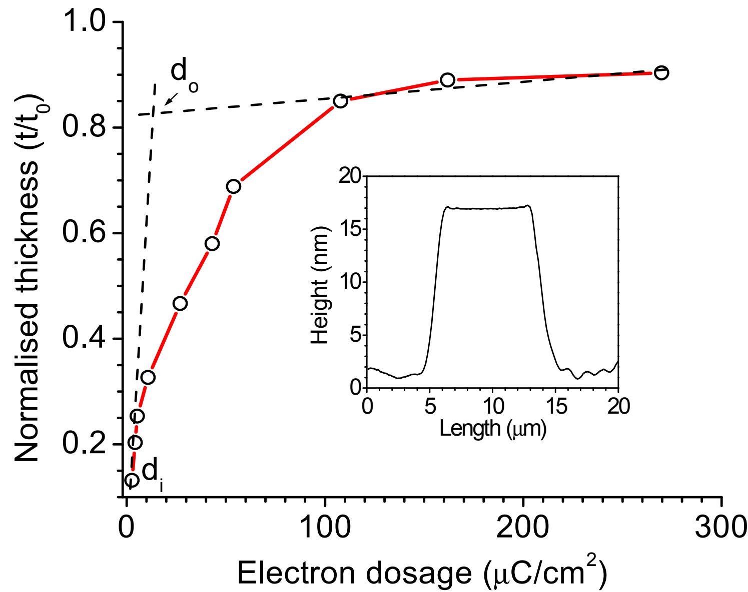

Figure 4.8: Normalized film thickness against the e-dosage for 5 kV. Inset showing the z-profile of a patterned region shown.

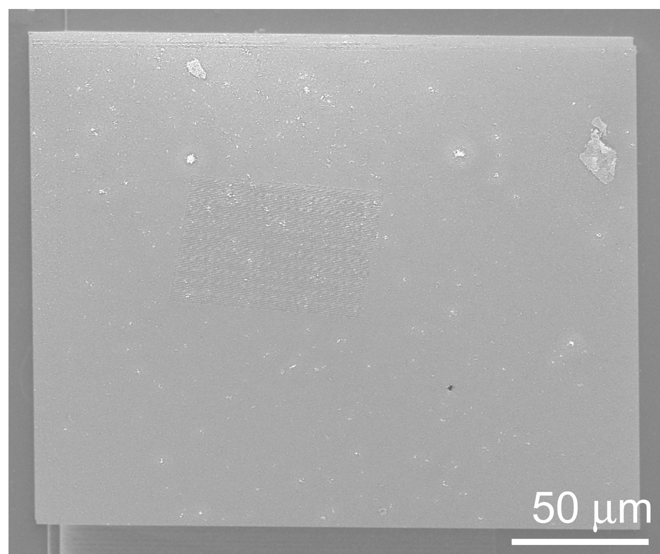

Figure 4.9: A large area pattern (250 x 230 μm^2) created at 5 kV with 36 μC.cm^{-2}.

The Pd thiolate resist is highly sensitive to the e-beam, and that makes large-area patterning with EBL more realistic. For example, the 250 x 230 μm^2 patterned square in Figure 4.14b was generated with an e-dosage as small as 36 μC.cm^{-2}, which also corresponds to its sensitivity. It may be noted that the e-dosage used to create this pattern is much less that the commonly used e-dosages for metals, in particular for Pd, the literature values being 10^3 and 10^5 μC.cm^{-2} from Stark et al.[66] and Reetz et al.[71], respectively.

In order to understand the conformations adopted by alkane chains on exposure to an e-beam, the IR spectra of pristine Pd hexadecanethiolate film with the one exposed to the e-beam at 5 kV with 2 μC.cm^{-2} were compared as shown in Figure 4.10. It is useful to classify IR vibrations into two types. First, there are vibrations which are non-localized and involve the entire chain. These non-localized modes give rise to band progressions which account for nearly all bands observed in this region of the IR spectrum [95–102]. Three such progressions are the methylene rocking progression (P_x) in the region 1000-700 cm^{-1}; the wagging progression,

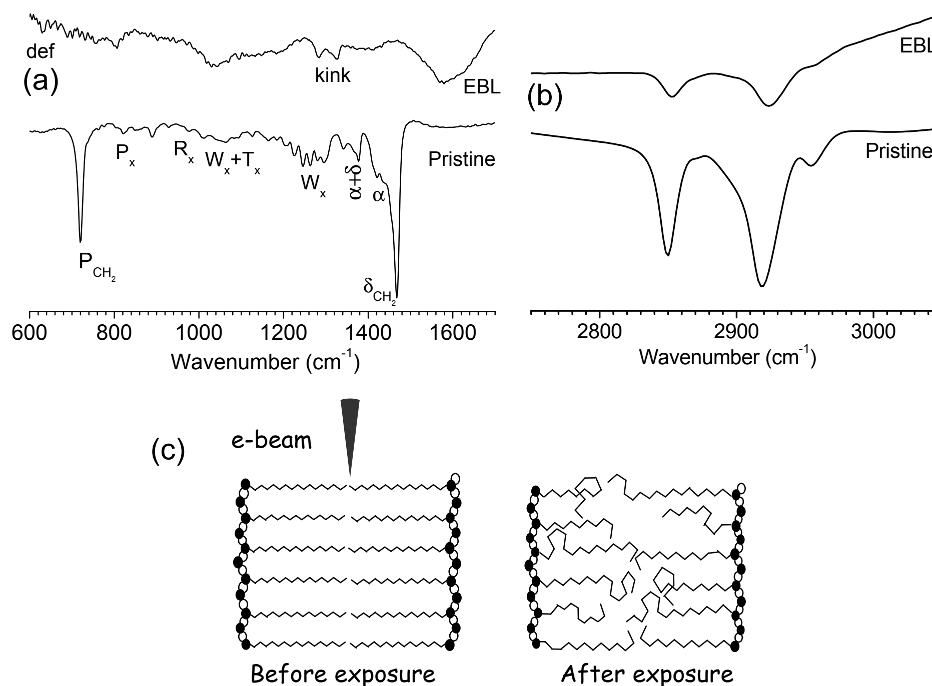

Figure 4.10: IR spectra of the pristine and e-beam exposed Pd hexadecanethiolate. (c)Schematic of the effect of e-beam exposure.

W_x in the region 1350-1150 cm^{-1}; and the C-C stretching progression, (R_x) in the region 1150-1000 cm^{-1}. In the case of pristine thiolate (Fig. 4.10a), the wag-twist progression bands ($W_x + T_x$, 1175- 1350 cm^{-1}) are well-defined implying that the coupling between the methylene oscillators is unaffected because the chains are all-trans, which is also evident from the C-H stretching modes (see Figure 4.10b). Interestingly, these bands are greatly diminished in intensity in the case of e-beam exposed film, which confirms the occurrence of gauche defects in the chains. The strong band at 1467 cm^{-1} due to the methylene scissoring mode (δ) seen in pristine film, is clearly absent in e-beam exposed film, indicating that there is deformation in the alkane chain on exposure of e-beam. Similar is the fate of the peak at 1419 cm^{-1} due to methylene deformation adjacent to the sulfur. The main band at 720 cm^{-1} is the head band of the rocking progression which seen for pristine film.

This band is highly diminished in the case of e-beam exposed film. The second type of vibration involves motions that are localized in certain parts of the chain. The methyl rocking mode at 890 cm^{-1} is an example of a localized vibration. The frequencies of these vibrations are dependent only on local conformation and, in contrast to non-localized modes, tend to be independent of both chain length and the conformation of the rest of the molecule. The peaks at 1454 and 1377 cm^{-1} in e-dosed film correspond to bending modes of the methyl group, the latter more specifically to the umbrella deformation (U), which are absent in pristine film. A peak at 1343 cm^{-1} in e-dosed film arises because of an end gauche defect (W_E). A series of peaks observed between 1000 and 1150 cm^{-1} are assigned to the skeletal C-C-C vibrational modes (R_x), while the progression bands in the region 700-980 cm^{-1} are assigned to the rocking modes (P_x) of the methylene chains. Apart from the above C-C-C skeletal stretching modes, the e-dosed film also exhibits weak bands at 1321 and 1365 cm^{-1} due to $W_{g-t-g'}$, indicating the presence of kinks in the chain, on exposure to e-beam. There is a broad peak observed around 1650 cm^{-1} in e-dosed film, this is due to the loss of hydrogen atoms and radical formation leading to double bonds. The characteristic C-H stretches of the methylene and the end-methyl groups of the alkane chain appear in the 2800-3000 cm^{-1} region (see Figure 4.10b). In the case of pristine thiolate, the symmetric (d_+) and antisymmetric (d_-) methylene C-H stretching modes are broad (see Figure 4.10) with the mean positions at 2848 and 2918 cm^{-1}, respectively. A shift of 4 cm^{-1} in the vibrational frequency implies a disordered environment, such as gauche defects in the thiolate film exposed to e-beam. The r_- (methyl anti-symmetric stretch) mode appears around 2960 cm^{-1}, which also diminishes on exposure to the e-beam and appears as a high frequency shoulder, indicating that most methyl groups have been damaged and/or removed [95]. Clearly, the e-beam exposure induced deformations in the

alkane chains of Pd thiolate making it less soluble and thus, an electron sensitive resist. Schematic of the deformation in alkane chain is shown in Figure 4.10c.

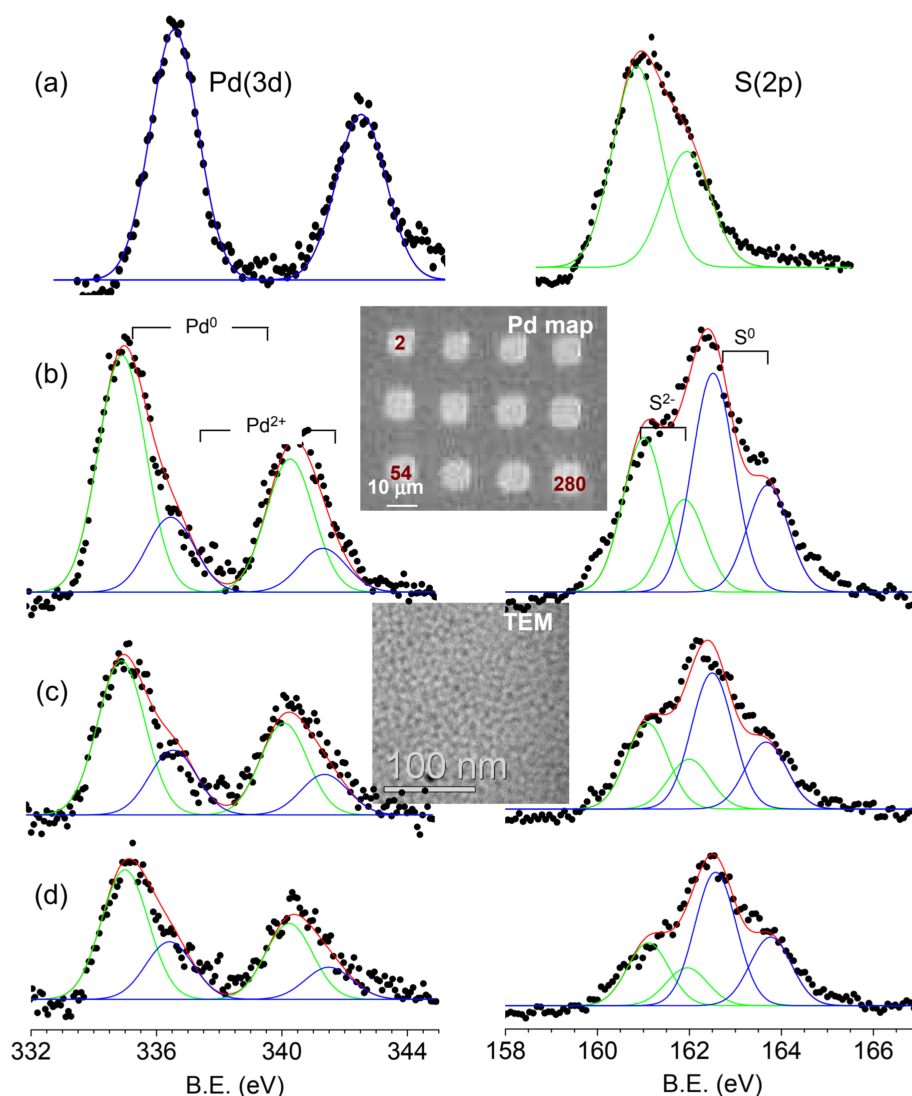

Figure 4.11: XPS of Pd (3d) and S(2p) recorded on (a) the pristine film and the patterned islands using 5 kV with different e-dosages, namely, (b) 2, (c) 54 and (d) 280 μC.cm^{-2}. Inset showing a core level mapping of an array of the Pd islands with different e-dosages and TEM image showing formation of fine Pd nanoparticles on exposure to e-beam.

In order to study the chemical changes on Pd thiolate on exposure to e-beam,

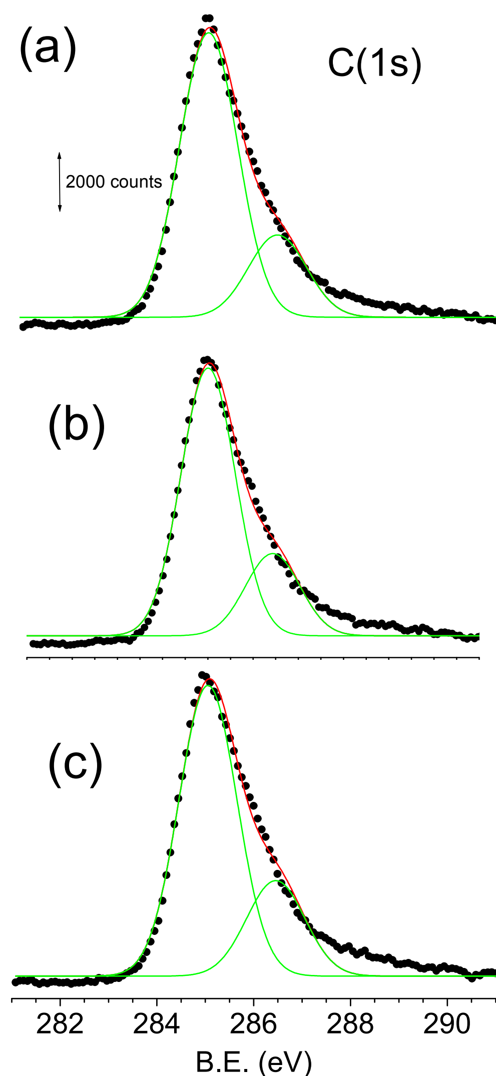

Figure 4.12: XPS of C(1s) recorded on the patterned islands using 5 kV with different e-dosages, namely, (a) 2, (b) 54 and (c) 280 μC.cm^{-2}.

XPS analysis using nanospectroscopy beamline was carried out on e-beam patterned islands where the e-dosage has been varied from 2 to 280 μC.cm^{-2}, as well as on a pristine Pd thiolate film for comparison (Figure 4.11). Pd(3d) and S(2p) core level spectra recorded on the pristine film show the presence of Pd^{2+} ($3d_{5/2}$ at 336 and $3d_{3/2}$ at 341 eV, respectively) and S^{2-} ($2p_{3/2}$ at 161 and $2p_{1/2}$ at 162.2 eV, respectively) species as expected. Among the 12 islands patterned, three were

chosen- 2, 54 and 280 μC.cm^{-2}, for the measurement. These have been marked in the core level map of the patterned region as shown in the inset of Figure 4.11. Surprisingly, in all the three cases, the Pd(3d) main peak is positioned at ~335 eV indicating predominant formation of the metallic species. This is the first important finding from the nano-XPS measurement. TEM image on the patterned region (see image in the middle) shows the formation of fine particles below 5 nm diameter. Indeed, the e-beam exposure not only brings about chain defects and deformation (as evidenced from IR measurements), but also causes significant reduction of Pd^{2+} to Pd^0. Following deconvolution into Pd^0 (335 and 340 eV) and Pd^{2+}, we observe that the ratio, Pd^0/Pd^{2+}, varies in a narrow range, 3.10 to 2.25, with e-dosage. The variation is apparently counter-intuitive; the ratio decreases with increase in e-dosage, 3.10, 2.28 and 2.25 at 2, 54 and 280 μC.cm^{-2} respectively. This suggests that during the development of the resist, the metallic species produced with higher e-dosage gets washed away relatively easily. Secondly, we notice that the overall spectral intensity decreases with increasing e-dosage. On the contrary, the C(1s) spectra showed a slight increase in the intensity (by ~15%) and increased broadening at higher binding energies due to radical formation during e-exposure (Figure 4.12. From the above observations, it may be deduced that the carbon content in the surface layers is almost insensitive to the e-dosage, while Pd is not; e-beam induces reduction and formation of metallic species but some of it is lost during developing of the resist, particularly from regions exposed to higher dosages. The unreduced Pd^{2+} is lost as well but to a lesser extent. The S(2p) spectra also show a similar trend as Pd(3d). Here, S^0 (162.5 and 163.7 eV) is predominant but decreases with increasing e-dose relative to S^{2-} (161 and 162.2 eV), the ratio being 0.70, 0.67 and 0.47 at 2, 54 and 280 μC.cm^{-2} for respectively.

As studied in the case of the film (see section 4.4.1), it is expected that thermol-

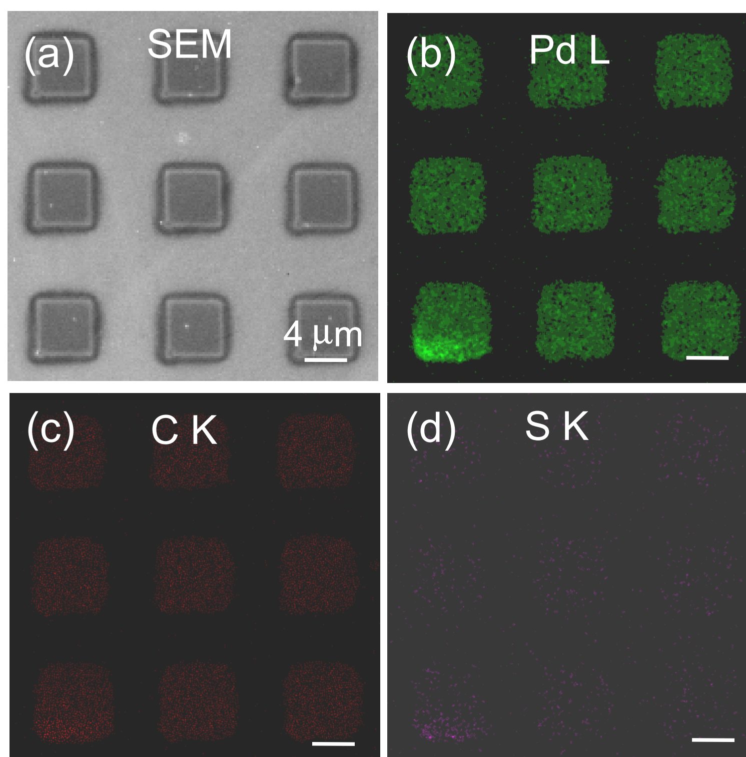

Figure 4.13: (a) SEM and EDS maps of (b) Pd L, (c) C K and (d) S K lines on the e-beam patterned regions after thermolysis.

ysis in air produce metallic Pd. In Figure 4.13, are shown SEM and EDS images of the patterned regions after ex-situ thermolysis at 250 °C. The overall morphology of the pattern is intact. Pd L EDS mapping (Figure 4.13b) shows the presence of Pd in the designated regions similar to that in Figure 4.7b. However, the C K and S K signals became significantly weaker following thermolysis (compare Figure 4.13c and d with Fig. 4.7c and d, respectively), with Pd: C: S (89.7: 9.8: 0.5) suggesting that the metallization process seems to be complete in the patterned regions.

In Figure 4.14 are shown Pd(3d) and S(2p) core level spectra from a 250 x 220 μm^2 patterned area (e-dosage, 2 $\mu C.cm^{-2}$) while subjected to increasing temperatures, the image in the centre being a Pd core-level map. The image looks slightly

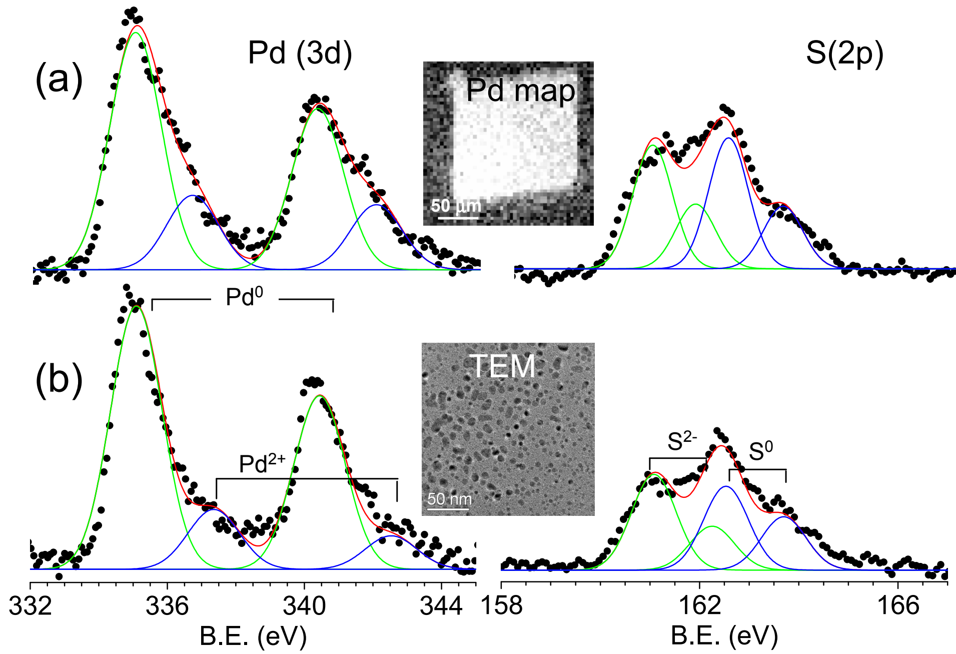

Figure 4.14: XPS of Pd (3d) and S(2p) recorded on a big island patterned with 5 kV at different thermolysis temperatures (a) 160 °C and (b) 250 °C performed in-situ. Inset: Core level mapping of Pd on the island subjected to in-situ thermolysis. TEM image of patterned Pd after thermolysis.

distorted because of mechanical drift of the substrate while in-situ heating. Prior to thermolysis, the room temperature spectra of the e-beam exposed resist gave Pd^0/Pd^{2+} and S^0/S^{2-} values of 3.14 and 0.47 respectively similar to spectra shown in Figure 4.11b. Upon heating the substrate to 150 °C, the relative content of Pd^0 increased (3.6) with the concomitant S^0 state (1.14). The content of metallic species further increased after reaching a substrate temperature of 250 °C (Pd^0/Pd^{2+}, 4.5). Accordingly, the TEM image showed the presence of Pd nanocrystals in the size range of 5-15 nm. This TEM image may be contrasted with that shown in Figure 4.11. The above observation clearly brings out the growth of Pd nuclei that were formed during EBL following thermolysis. The Pd^{2+} and S^{2-} species seen after thermolysis, correspond mostly to the surface species.

Here, e-dosage seems to have countering effects on the direct write resist. While a higher dosage does induce more resist action (in terms of defect formation and cross-linking), it also makes the resist more vulnerable to developing, as the reduced Pd species are more likely to get washed away than the charged species. At lower doses, however, much of the Pd precursor gets washed away due to insufficient resist action. One needs to strike a balance between these two countering effects. Unlike in the case of a conventional polymer resist, a higher contrast alone is not sufficient for a direct write resist. A predominant presence of the active precursor is important and in this sense the optimal parameters for a direct write precursor would be different from those of conventional resists. Under the given conditions, a dose of over 100 μC.cm^{-2} can retain upto 90% of the resist thickness with total Pd content nearly 1.5 times than that retained at the sensitivity value (42 μC.cm^{-2}).

4.4.3 A Pd nanowire circuit

Being a truly molecular precursor, Pd thiolate resist allows hight resolution patterning. In Figure 4.15 is shown a set of parallel nanowires each with diameter of ~30 nm and height around 110 nm. The electrical behavior of one such nanowire during thermolysis was examined by fabricating a circuit with a patterned thiolate line as an active element between Au gap electrodes on a SiO_2(150 nm)/Si substrate (Figure 4.16a) and collected the I-V data during heating (Figure 4.16b). The gap between the two electrodes was ~20 μm. The current prior to thermolysis was in the range of picoamperes which, upon heating to 180 °C, increased to a few nanoamperes and, at 200 °C, to 0.1 μA (at 2 V). At 215 °C, the current was unsteady and increased by an order magnitude over a period of 120 seconds (see the lines labeled 215 °C, 215 °C', and 215 °C"). At 230 °C, however, the current

in the circuit shot up to 80 μA within 1 mV. Figure 4.16c shows the nanowire after thermolysis which is continuous and smooth.

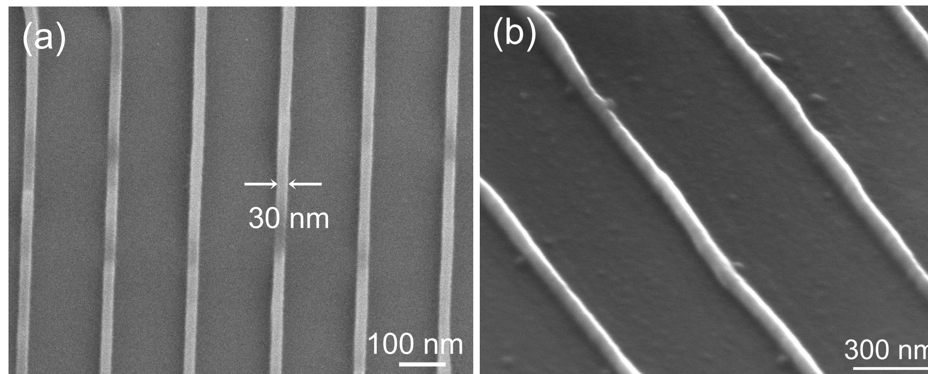

Figure 4.15: SEM images of thermolysed Pd nanowires created using 30 kV

.

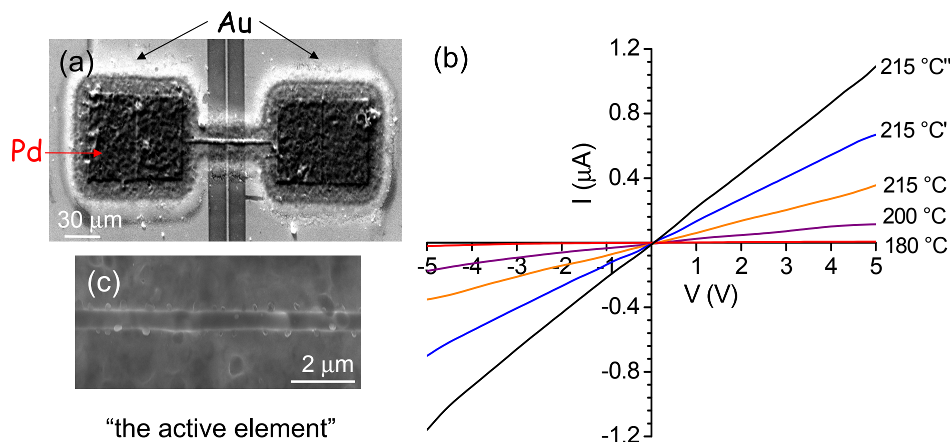

Figure 4.16: (a) SEM images of the fabricated circuit. (b) I-V data of a patterned Pd hexadecanethiolate nanowire between 20 μm Au gap electrodes on a SiO_2(150 nm)/Si substrate subjected to different temperatures (in °C). At 215 °C, three measurements were made within a span of 120 seconds. (c) Magnified image of the active element after thermolysis.

Figure 4.17 shows a plot of resistance versus thermolysis temperature. Prior to thermolysis, the resistance of the Pd nanowire was ~11.2 MΩ, which gradually decreased to 0.65 kΩ when the wire was heated to 215 °C, beyond which the fall in resistance was steep, reaching a value of 20 Ω at 230 °C, corresponding to a specific

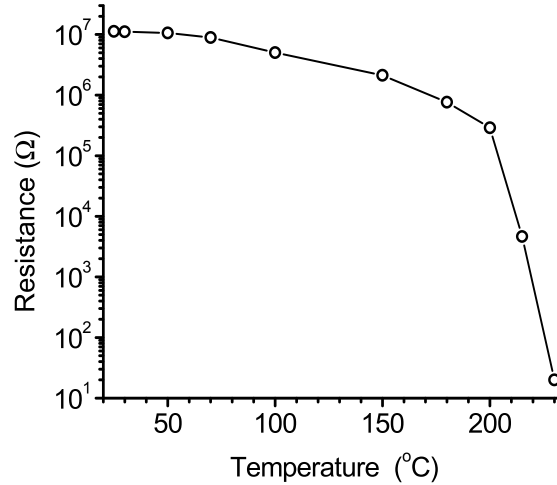

A comparison with literature

Precursor	keV	e-dosage μC.cm^{-2}	ρ/ρ_{bulk}	Ref
Pd-TOABr	120	200 000	39.71	Reetz et al.
$Pd(OAc)_2$	5	1000	9.52	Stark et al.
$Pd(SR)_2$	5	20	2.85	Present work

Figure 4.17: Semi-log plot of resistance (at 2 V) versus thermolysis temperature. A table comparing the literature value of resistivity for patterned Pd.

resistivity of 0.300 $\mu\Omega$.m. It is worth noting that this value of resistivity is only about 3 times the bulk Pd resistivity (0.105 $\mu\Omega$.m). The highly conducting nature of the Pd nanowire obtained is evident when compared to literature values of 100 and 417 $\mu\Omega$.m from Stark et al.[66] and Reetz et al.[71], respectively.

4.5 Conclusions

In conclusion, the present study demonstrates the use of Pd hexadecanethiolate as a direct-write electron resist capable of producing nanometric patterns. The high solubility of the thiolate precursor qualifies it for processing as a resist. The resist preparation is simple and EBL patterning involves only three steps: coating

the resist, exposing and developing. Being a molecular precursor, it allows high-resolution patterning and, importantly, requires very small dosages (a few tens of μC.cm^{-2} at 5 kV), as the alkane chains undergoing disorder and cross-linking are very sensitive to the energetic electrons. Post-treatment leading to metallic nanopatterns is simple, involving heating to 230 °C in air. While the composition of the patterned resist closely resembles that of the thiolate precursor, following thermolysis, the obtained metal lines contain carbon at a record low level ($<$10%), unusual in EBL studies.

CHAPTER 5

Ni butanethiolate as a direct write e-beam resist and electrical characterization of patterned nanowires of NiS_2

Summary*

Thermolysis of Ni butanethiolate at 250 °C in sulfur atmosphere for an hour leads to the formation of NiS_2. SEM and TEM microscopy studies have revealed the formation of 20-30 nm sized nanoparticles. Importantly, Ni thiolate has been shown to work as a negative tone e-beam resist. It could be patterned using 10 kV with a typical dosage of 350 μC.cm^{-2}. After thermolysis in sulfur atmosphere, the patterned regions retained the S species in the form of NiS_2. This property of the thiolate was exploited to fabricate a nanowire of NiS_2 across Au electrodes using EBL. I-V measurements at room temperature showed a linear behavior while at lower temperature (200 K), the curve was non-linear with negligible current near zero bias region - typical of an activated metal. This property of the nanowire resembles the surface metallicity seen in bulk semiconducting NiS_2.

*A manuscript based on this work is under preparation.

5.1 Introduction

Nickel disulfide, NiS_2, like other 3d transition metal dichalcogenides, exhibits a pyrite structure. The electrical and magnetic properties of this family, MS_2 (M = Mn to Zn) are interesting [103]. For example, FeS_2 is a semiconducting with a band gap of $\simeq$ 0.9 eV, CoS_2 is metallic and orders ferromagnetically below $T_c \simeq 120$ K. NiS_2 is an antiferromagnetic insulator with a small gap of 0.3-0.8 eV [104] and $T_N \simeq 40$ K [105]. One-electron band models have been proposed to explain these properties: Between the empty S 3p band consisting of the pπ^* antibonding orbital of the $(S_2)^{2-}$ molecule and the occupied S 3p band of the remaining $S_2)^{2-}$ orbitals, a relatively wide metal 3d (e_g) band and a narrow 3d (t_{2g}) band are located. In FeS_2, the t_{2g} band is full and the e_g band is empty, leading to the nonmagnetic, insulating behavior. In CoS_2, the e_g band is occupied by one electron per Co and polarized ferromagnetically. NiS_2 is insulating in spite of the half-filled e_g band, and is therefore considered to be a Mott insulator.

The exceptional behavior of NiS_2 shows up also in the lattice parameters being larger than expected from their systematic variation in the pyrite family, MS_2, with M = Mn - Zn [106]. The unusually expanded lattice of NiS_2 is expected to lead to a reduction of the bandwidth, driving bulk NiS_2 insulating, in contrast to the metallic ground states of CoS_2 and CuS_2. However, the surface of NiS_2 behaves differently as revealed by photoemission states [103]. The surface electric structure of NiS_2 exhibits a tendency towards a more metallic character which is attributed to lattice relaxation near the surface [107]. Thus, it forms a 2D metallic system and hence immense interest in this system.

5.2 Scope of the Present Investigation

There has been a proposition that the surface of NiS_2 is different, it behaves metallic while the bulk is semiconducting. While the behavior of the bulk is itself considered unusual in the series of 3d metal disulfides, its surface is even more unusual. However, there is no report in the literature on the electrical nature of NiS_2 nanostructures. It would be interesting to investigate this aspect in nanoscale NiS_2, where the surface properties may override the bulk. The present investigation is aimed to address the interesting aspect especially using a single NiS_2 nanowire circuit. It was explored whether this could be achieved by direct write lithography. Similar to Pd precursor (Pd hexadecanethiolate, see Chapter 4) which enabled direct write of Pd patterns, the possibility of using Ni butanethiolate was explored, as this precursor could be solubilized and spin coated.

5.3 Experimental Details

For preparing Ni butanethiolate, nickel chloride hexahydrate, $NiCl_2.6H_2O$ (Merck, 1 mmol), was used as the precursor and the reaction was done in absolute ethanol in the presence of triethyl amine, $(CH_3)_3NH$ (Merck, 2 mmol) that helped in the generation of alkyl sulfide anion by abstracting a proton. Triethyl amine and butanethiol (C_4H_9SH) were taken in equimolar ratio. On vigorous stirring, the solution turned reddish brown following the reaction and the compound was obtained as sticky brownish black precipitate from ethanol medium. The precipitate was thoroughly washed with methanol followed by acetonitrile to remove excess reactants. This was done till there was no evidence for chloride ions in EDS [108]. Ni butanethiolate, $(Ni(SC_4H_9)_2)_n$ was dissolved in toluene to obtain a solution of 1 μM. It may be noted that Ni butanethiolate was preferred as higher Ni thiolates

cannot be solubilized easily to get a clear solution.

For EBL patterning, Si substrate (n-doped, 4-7 Ω.cm) were cleaned by sonicating in acetone and doubly distilled water and dried under flowing argon. The resist film was prepared by spin-coating 60 μl of Ni butanethiolate solution (10 μM) at 2000 rpm. EBL was performed using a Nova NanoSEM 600 instrument (FEI Co., The Netherlands)(see section 1.6 for details). The electron beam energy employed for patterning was 10 kV with a typical e-dosage of 350 μC.cm^{-2}. Following patterning, the patterns were developed in toluene for 5 seconds. For nanocircuit fabrication, Au metal film of 70 nm thickness was thermally deposited with a gap of 20 μm between the two electrodes on a glass substrate. A nanowire was patterned across the two Au electrodes. In order convert the thiolate species to Ni sulfide, the patterned substrate was subjected to thermolysis in a tube furnace heated at 300 °C for an hour. Ar gas was passed over a small amount of sulfur powder heated at 300 °C to carry vapors over the substrate carrying Ni thiolate placed slightly away at ∼250 °C.

XRD measurements were performed using a Siemens Seifert 3000TT diffractometer (Cu K_α = 1.5406 $\mathring{A}$, scan rate, 0.5 deg.min^{-1}). UV-Vis spectra was recorded in reflective mode using a Perkin-Elmer Lambda 900 UV/vis/NIR spectrophotometer. Raman measurements were performed using a LabRAM HR apparatus (Horiba, USA) with an excitation wavelength of 632.8 nm. Energy-dispersive spectroscopy (EDS) analysis was performed with an EDAX Genesis instrument (Mahwah, NJ) attached to the SEM column. Transmission electron microscopy (TEM) measurements were carried out with a JEOL-3010 instrument operating at 300 kV. The sample, NiS_2, was scrapped out from the substrate and dispersed in toluene and a drop of this dispersion was placed on a holey carbon grid.

5.4 Results and Discussion

Ni thiolate on thermolysis in air would undergo oxidation (unlike Pd thiolate, see Chapter 4) whereas in sulfur atmosphere, is expected to yield Ni sulfide species. This is understandable since Ni being a 3d metal is relatively more reactive. In the present case, a thin film of Ni butanethiolate was heated in sulfur atmosphere at 250 °C for an hour. Figure 5.1 shows the XRD patterns obtained on the pristine and the thermolysed film. The XRD pattern of the pristine film in Figure 5.1a, shows an intense diffraction peak at 2θ of 7.254° corresponding to a 12.177 $\AA$ spacing. This is ascribed to the d(001) peak in a lamellar bilayer structure [108]. Higher angle region (see inset in Figure 5.1a) shows the absence of any species such as oxide or sulfide. On thermolysis in sulfur atmosphere, the formation of Ni disulphide (NiS_2) is evident as confirmed from the XRD shown in Figure 5.1b. The most intense peak seen in the pattern corresponds to d(200) of NiS_2 (JCPDS 89-3058). All the peaks present are easily indexable to different planes of pyrite NiS_2. Only negligible intensity is seen in the d(001) region of the thiolate (see inset in Figure 5.1b). The cubic lattice parameter estimated for NiS_2 phase is 5.68 $\AA$, compares well with the reported value of 5.677 $\AA$ (JCPDS 89-3058). The particle size estimated for the width of the d(001) is 29.9 nm. The formation of NiS_2 as against other known sulfides (NiS and Ni_3S_2) is understandable, in the pristine thiolate the Ni:S ratio is 1:2 and the sulfur loss during thermolysis is prevented by the sulfur rich atmosphere present during thermolysis.

UV-Vis absorption spectrum of the pristine Ni thiolate is shown is Figure 5.2a. Three absorption peaks at 334, 411 and 551 nm are seen. These intense absorptions correspond to the S(thiolate) p$\pi \longrightarrow$ Ni d-orbital charge transfer transitions. For tetrahedral Ni(II), additional bands in longer wavelength region (>700 nm)

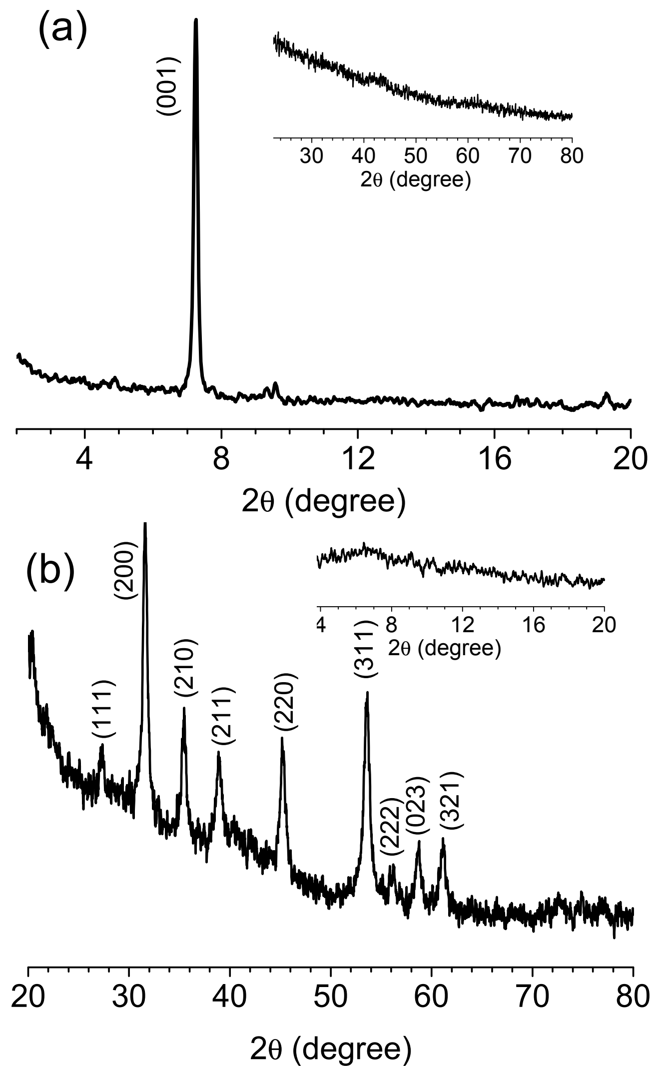

Figure 5.1: X-ray diffraction pattern of the precursor (a) before and (b) after thermolysis in sulfur atmosphere at 250 °C.

are expected due to spin allowed d-d transitions. The absence of any prominent d-d transitions is suggestive of a square planar geometry for Ni(II) [109]. On thermolysing in sulphur atmosphere, one broad band is observed around 410 nm. Raman spectrum recorded on thermolysed film is shown in Figure 5.2b has a sharp band at 493 cm^{-1} corresponding to NiS_2. The corresponding peak for NiS occurs

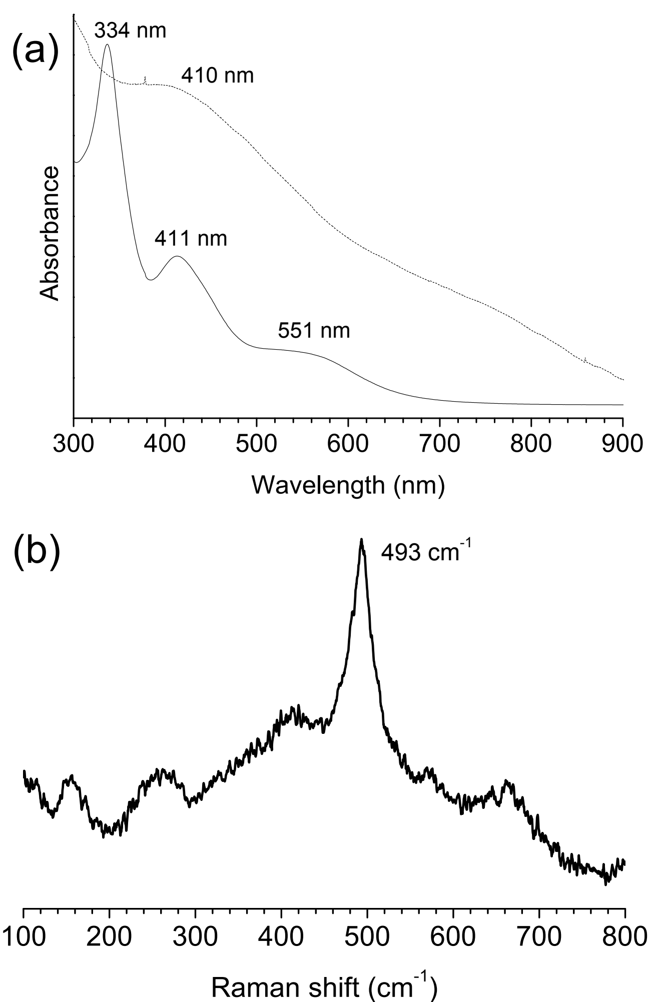

Figure 5.2: (a) UV-VIS spectrum of the precursor before and after (dashed) thermolysis in sulfur atmosphere at 250 °C for an hour and (b) Raman spectrum of the thermolysed film.

at 550 cm^{-1}.

Microscopic analysis was carried out on thermolysed precursor as shown in Figure 5.3. In the SEM image shown (see Figure 5.3a), the film appears granular and the formation of 10-30 nm nanoparticles in irregular and agglomerated form is evident. TEM image of one such aggregate in Figure 5.3b also supports the presence of such nanoparticles. From the high resolution TEM image shown in Figure 5.3c,

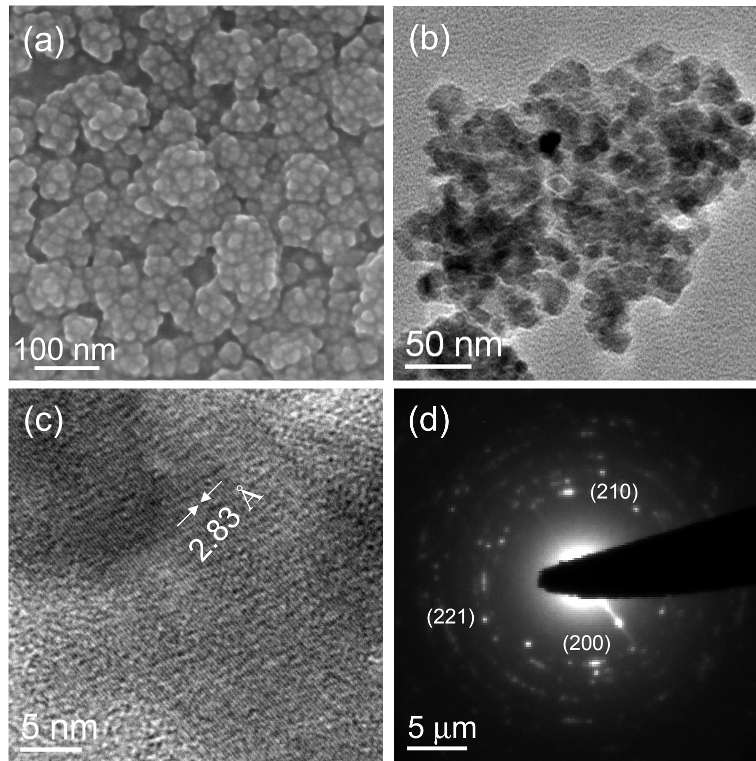

Figure 5.3: (a) SEM, (b) TEM, (d) HRTEM and (c) ED pattern of the thermolysed film.

it is clear that the nanoparticles are crystalline and the lattice reflections seen correspond to the d(200) peak of 2.83 $\AA$. The ED pattern in Figure 5.3d confirms the overall crystallinity of the sample. The diffraction pattern correspond to (200), (210) and (221) planes of pyrite NiS_2.

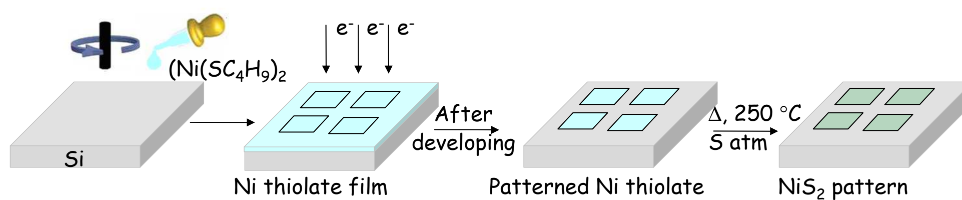

Figure 5.4: Schematic of the procedure adopted. Step 1 - Spin coating of the Ni butanethiolate on Si surface. Step 2 - EBL patterning at 10 kV, Step 3 - Developing the patterned substrate in toluene for 5 seconds and Step 4 - Thermolysis at 250 °C in sulfur atmosphere.

Having successfully established the formation of NiS_2 through the treatment of Ni butanethiolate, the latter was used as an e-resist for patterning. The direct write procedure adopted is simple involving basically three steps (see scheme in Figure 5.4) and is similar to the one shown in Figure 4.6 (Chapter 4). Ni butanethiolate film spin-coated on a Si substrate was patterned using a 10 kV electron beam at dosages between 350 - 500 μC.cm^{-2} and developed in toluene for 5 seconds. The regions exposed to the e-beam remained on the substrate after developing (Figure 5.5) thus indicating the negative tone resist behavior of the thiolate. Figure 5.5a shows the SEM patterned squares (6 x 6 μm^2). It appears that under an e-beam, the hydrocarbon chains of the thiolate seem to develop defects and produce a disordered phase with decreased solubility in the developing solvent (toluene). The e-beam may also promote radical formation and cross-linking of the alkane chains, essentially making it work as a resist. The electron dose employed here is 500 μC.cm^{-2}, but the sensitivity is found to much lesser around 350 μC.cm^{-2}.

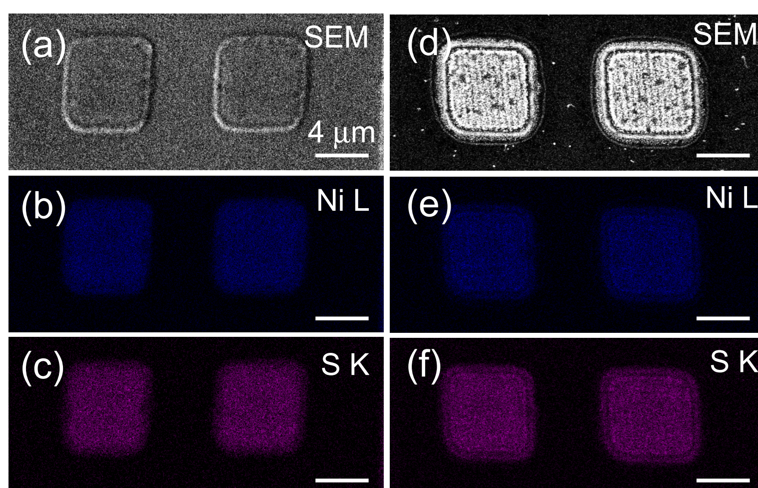

Figure 5.5: a,d) SEM and b-c, e-f) EDS maps of Ni L, and S K lines on the e-beam patterned regions before (a-c) and after (d-f) thermolysis.

The energy dispersive spectral (EDS) images in Figures 5.5b and c show mapping of Ni L and S K lines indicating the presence of Ni and S in the respec-

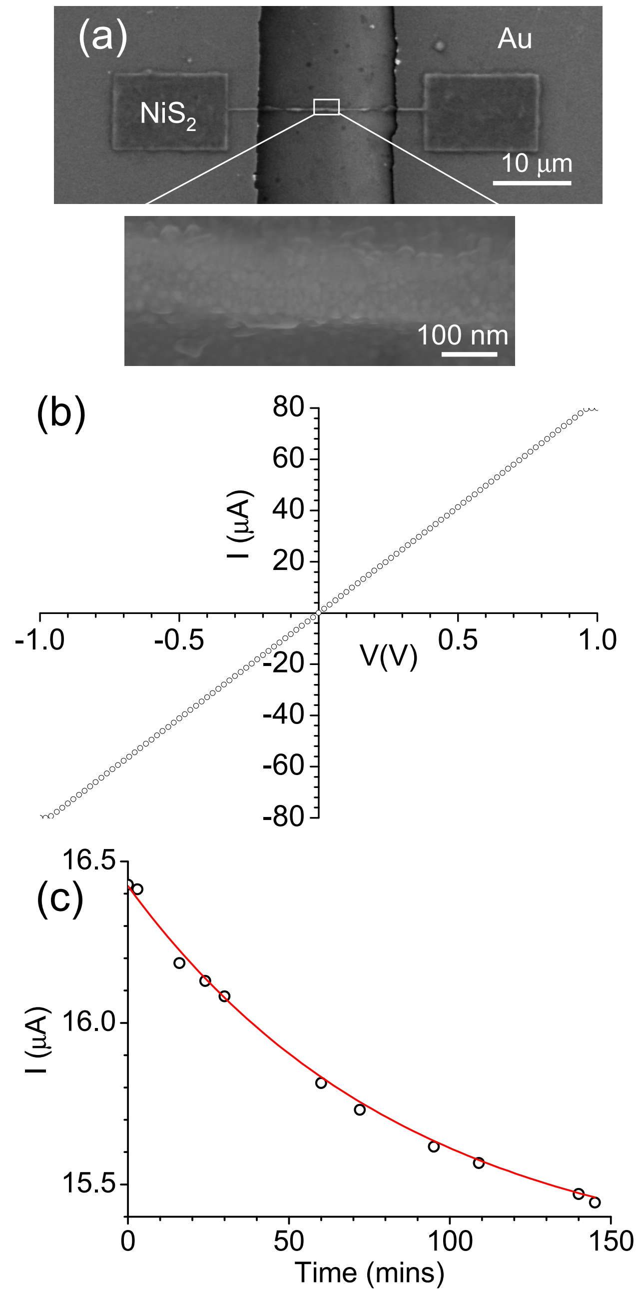

Figure 5.6: (a) SEM image showing the patterned nanowire between Au gap electrodes (gap = 17 μm)on glass substrate and magnified image the nanowire after thermolysis in 250 °C in sulfur atmosphere. (b) I-V data of a patterned nanowire and (c) Current measured at 0.2 V versus time plot of the same circuit showing the expontentially drop in current due to surface oxidation.

tive regions. The atomic Ni:S:C ratios of 36:30:34 obtained for the patterned regions and agrees with the initial composition (27:29:44) of the unexposed resist, $(Ni(SC_4H_9)_2)_n$, which implies that the electron dosage causes only minimal change in the overall composition. The SEM image in Figure 5.5d shows the patterned region after thermolysis in sulphur atmosphere at 250 °C for an hour. The morphology of the pattern is intact. Ni L and S K EDS mapping (Figures 5.5e and f) shows the presence of Ni and S in the designated regions similar to that in Figure 5.5b and c respectively. However, the C content has dropped down drastically following thermolysis (Ni:S:C, 35:49:12). Importantly, there is no loss of sulfur but instead there is 19% increase. The excess sulfur is essentially due to condensation of elemental sulfur on the NiS_2 surface, during thermolysis.

The electrical behavior of this resist is studied by fabricating a circuit with a patterned thiolate line as an active element between Au gap electrodes laid out with a gap of $\sim$17 μm on a glass substrate (Figure 5.6a). The patterned nanowire is 180 nm wide and 200 nm thick. I-V measurements after patterning and following thermolysis in sulfur atmosphere at 250 °C for an hour (similar conditions as in the case of film) is shown in Figure 5.6b. It was that the current prior to thermolysis was in the range of nanoamperes (0.711 nA at 1 V) corresponding to a limited conduction through the hydrocarbon chains which upon thermolysis, increased to 80 μA at 1 V (see Figure 5.6b). The I-V curve is found to be linear after thermolysis. In other words, prior to thermolysis, the resistance of the precursor nanowire was 1.40 GΩ, which decreased to 12.15 kΩ after thermolysis, corresponding to a specific resistivity of 2.144 x 10^{-4} Ω.m. It is worth noting that this value of resistivity is about 2 orders lesser the bulk NiS_2 resistivity (1.2 x 10^{-2} Ω.m). It is remarkable that the I-V is linear suggesting semi-metallic nature of the nanowire, unlike the bulk which is known to be semiconducting [110]. The semi-metallic nature of

the nanowire observed may be linked to the surface property of NiS_2, that being metallic. This is easily understandable since the nanowire contains relatively more surface species and the predominance of the surface property shows up in its I-V behavior, and hence a lower resistivity. If this may be so, one may expect the electrical behavior of the nanowire to be influenced by surface oxidation of air. In Figure 5.6c is shown the variation in the resistance of the nanowire over a period of 2.5 hours, in air measured at 0.2 V. The current follows a first order exponential decay.

$$I(t) = I_0 + Ae^{-x/t} \tag{5.1}$$

where I_0 = 15.2332 μA, A = 1.19068 μA and t = 87.40766 minutes).

This is due to slow surface oxidation. The process is exponential but slow with a time constant of 87.4 minutes and asymptotic value of 15.2 μA indicating that the oxidation is diffusion limited. In order to expedite the process, the circuit was heated in air at 60 °C for 2 minutes and at this stage, the measured current dropped to nanoampere range confirming complete oxidation of the nanowire.

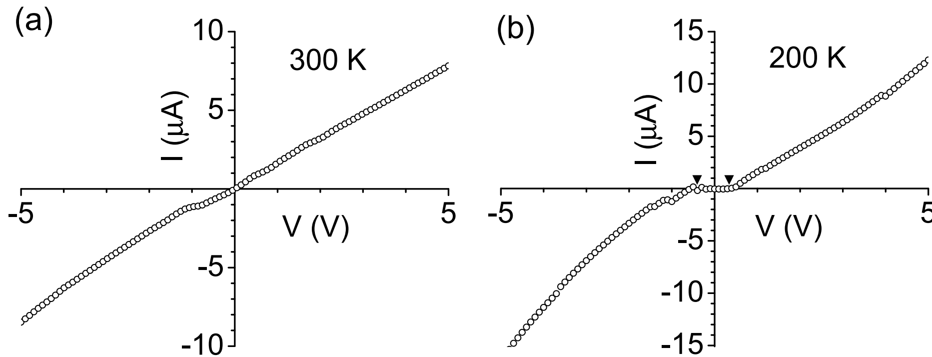

Figure 5.7: I-V measurements done at (a)300 K and (b) 200 K on the patterned NiS_2 nanowire. Arrows indicating negligible current region.

Upon heating in sulfur atmosphere at 250 °C, the nanowire regained the conductivity as shown in Figure 5.7a. The semi-metallic nature of the nanowire was

further investigated by performing an I-V at lower temperature of 200 K (by mounting the nanowire circuit on a cold finger cooled by nitrogen vapor. The I-V curve is seen to be flattened near the zero bias region, the width of which is 0.8 eV. This value is in the range of values reported for the bulk NiS_2, 0.3 -0.8 eV [104]. This measurement demonstrates the activated electrical nature of the nanowire.

5.5 Conclusions

Thermolysis of Ni butanethiolate in sulfur atmosphere leads to the formation of NiS_2 nanoparticles. This precursor has been patterned using e-beam, hence it is a clear demonstration of a direct write precursor for Ni structures. On thermolysis of patterned thiolate, NiS_2 nanoparticles are formed in designated areas with size in the range of 20-30 nm as revealed by SEM and TEM images. I-V measurement on a patterned NiS_2 is linear at room temperature with resistivity of 10^{-4} Ω.m. Thus, the nanowire seems to show a metallic conductivity behavior which goes well with the known surface metallicity of bulk semiconducting NiS_2. Upon lowering the temperature, the I-V data becomes non-linear with negligible current near zero bias, typical of an activated conductor. The nanowire circuit was also sensitive enough to detect air-oxidation. Upon heating to 60 °C, there was no current in the circuit indicating complete oxidation of the active element.

CHAPTER 6

Catalytic growth of ZnO nanostructures on e-beam patterned Pd

Summary*

ZnO growth from a solution based method using Pd nanoparticles (~10 nm) as catalyst has been demonstrated. As Pd thiolate can be patterned using e-beam, ZnO growth is realized on patterned Pd catalyst. Fine nanowires of ZnO with diameter <10 nm are obtained when a Si substrate carrying patterned Pd nanoparticles was dropped in $Zn(NO_3)_2$/TEAB solution for 10 minutes at 80 °C. Longer duration in the precursor solution led to formation of ZnO fibril like structures. EDS analysis confirmed the formation of ZnO structures on Pd nanoparticles and XRD measurements confirmed the hexagonal phase of ZnO being formed. Photoluminescence studies has shown that the fibril-like structures exhibit blue shift in the 390 nm emission peak when the excitation energy is increased, unlike bulk ZnO. This is attributed to the defects present in the quantum confined nanostructures.

6.1 Introduction

Well-defined growth of nanotubes and nanowires on solid substrates is achieved by suitably selecting catalyst seed particles in the vapor-liquid-solid (VLS) method.

*A manuscript based on this work is under preparation.

Thus, various metal nanoparticles have been used to grow nanorods, nanotubes and nanowires of metal and metal oxides. Chen et al.[111] have obtained nanowires of GaN with diameters of 10-50 nm using various metal catalysts such as In, Fe, Co, Ni, or bimetallic (Ni, Co, Fe) metal nitrides. Hannon et al.[112] have studied the growth of Si nanowires using Au catalyst where as Pan et al.[113] used molten Ga as catalyst to grow carrot shaped silica nanowires. Bethune et al.[114] used Co, Fe, Ni catalyst and found Co catalyst induced growth single walled nanotubes. Large scale aligned nanotubes have been reported using Fe catalyst by Li et al.[115] It has been generally found that the ultimate diameter of the nanostructure depends on the size if the seed particle. This has enabled a fine control on the diameter of the grown nanostructures. Templated growth of these nanostructures has also been achieved by impregnating the catalyst particle within the template.

Patterned growth of nanowires and nanotubes is crucial in technology applications such as flat panel display and electronic nose. In the past few years, a number of approaches have been employed to obtain microscale- and nanoscale-patterned metal catalysts for successful large-scale fabrication of nanostructure arrays. This is usually achieved by first patterning the desired metal catalyst and then growing the nanowires or nanotubes by chemical vapor deposition (CVD) or pulsed laser deposition (PLD) or solution based methods. Peng et al.[116] patterned the Fe catalyst and applied the electric field to obtain ordered arrays of suspended SWNTs on predefined locations using a methane CVD growth method. Thus, device-quality SWNTs were grown directly on catalyzed metal electrodes with good electrical contact. The patterned array of MWNTs by CVD has been obtained by first printing a Co nanoparticle catalyst ink with ink-jet technique [117]. For truly nanoscale patterning, EBL technique has been demonstrated as in the case of nanowire arrays of InP [118]. Nanoimprint lithography (NIL) has also been used to obtain

highly ordered and spatially separated metal catalyst dots for subsequent growth of InP nanowire arrays [119]. Kind et al. used microcontact printing to bring in patterned Pd catalyst nanoparticles for the growth of CNTs [120] as well growth of electroless Cu [121].

There are a few examples of patterned growth on ZnO nanostuctures using seed particles. Microscale Au patterns have been generated by the evaporation of Au through masks such as TEM grids [122] as well as by using microsphere lithography [123]. Control growth of ZnO nanowire was obtained in a simple chemical vapor transport and condensation (CVTC) method [122] whereas growing large-area, hexagonally patterned, aligned ZnO nanorod was demonstrated by Wang et al.[124]. In another study, Fan et al.[125] prepared the catalyst Au nanodot templates and carried out ZnO deposition by metal organic CVD. Li et al.[126] used templated porous alumia to grow polycrystalline ZnO nanowires. Similarly, Huang et al.[127] patterned nanowire networks of photoluminescent highly crystalline ZnO nanowires using VLS growth with a catalyst template. Tak et al.[128], deposited thin zinc metal seed layer on a silicon substrate by thermal evaporation and have grown ZnO nanorods. Saito et al.[129, 130] fabricated an electroless method for ZnO micropatterning on Pd catalyst by employing a SAM of photopatterned phenyltrichlorosilane. Lee et al.[131, 132] have developed a simple dry process for the patterning metal nanoparticles in polymer films through the reduction of a metal complex using UV radiation, ZnO crystals were synthesized on the UV-patterned Pd catalysts in the aqueous solution of dimethylamine borane (DMAB)/$Zn(NO_3)_2$ with different ratios and at different temperatures.

6.2 Scope of the Present Investigation

The present investigation aims to produce fine Pd nanoparticles as catalyst for the growth of ZnO nanowires. There are several reports where patterned growth of ZnO has been carried out using patterning Pd using photolithography techniques [131, 132]. As such, ZnO nanowires of $\sim$10 nm are not common. This study exploits the patternable nature of Pd hexadecanethiolate which upon thermolysis would yield Pd nanoparticles in patterns. ZnO growth is followed by a solution based method.

6.3 Experimental Details

Pd hexadecanethiolate was spin coated on Si surfaces and patterned using electron beam lithography (EBL), which was performed using an e-beam writer available with the SEM equipment (Nova NanoSEM 600 equipment, FEI Co.,The Netherlands). The substrate was then developed in toluene for 10 seconds and subjected to thermolysis at 250 °C in air for 30 minutes to obtain Pd metal in the patterned regions. Catalytic property of the patterned Pd was studied by growing ZnO on the patterned regions. For this purpose, Pd/Si patterned substrates were dipped in equimolar solution of Zinc nitrate, $Zn(NO_3)_2$ and triethyamine borane, (TEAB). The reaction was carried out at 80 °C and for 10 and 45 minutes.

X-ray diffraction (XRD) measurements were performed using a Siemens Seifert 3000TT diffractometer (Cu K_α 1.5406 $\mathring{A}$, scan rate, 1 deg.min^{-1}). UV-visible recorded in reflective mode using a Perkin-Elmer Lambda 900 UV/vis/NIR spectrophotometer. The photoluminescence (PL) spectra were collected with different excitation wavelengths using a Perkin-Elmer LS55 Luminescence spectrometer. In order to perform transmission electron microscopy (TEM), the nanomaterial

ZnO/Pd was scrapped from the substrate and dispersed in toluene and a drop was placed on a holey carbon grid. High-resolution TEM imaging was carried out with a JEOL-3010 equipment operating at 300 kV. The same grid was used for STEM (scanning transmission electron microscopy), performed on a Nova NanoSEM 600 equipment (FEI Co., The Netherlands)(see section 1.6 for details). Energy dispersive spectroscopy (EDS) analysis was performed with an EDAX Genesis (Mahwah, USA), attached to the SEM column.

6.4 Results and Discussion

In an initial study, the catalytically property of the thermolysed Pd was optimized for ZnO growth. A microdrop of Pd hexadecanethiolate was placed on a Si substrate and was thermolysed at 250 °C in air for 30 minutes. This is expected to result in Pd metal nanoparticles (see section 4.4.1). The substrate was dipped in a equimolar $Zn(NO_3)_2$/TEAB solution at 80 °C for 45 minutes. The SEM micrograph of the ZnO structure is shown in Figure 6.1a. Corresponding to the SEM image, the energy dispersive spectral (EDS) images obtaining by mapping Pd L, Zn L and O K lines are shown in Figures 6.1b-d respectively. The maps show the presence of Pd, Zn and O in the patterned region and confirmed the site-selective formation of ZnO.

The SEM image of ZnO structures obtained at 80 °C after dipping the thermolysed Pd film in the reaction solution for 10 minutes, is shown in Figure 6.2. The formation of distinct ZnO nanowires with diameter of ∼10 nm is distinct. Some plate like features are also seen. Figure 6.3 are the STEM and TEM micrographs obtained by scrapped ZnO structures on a holey copper grid. The images also reveal the formation of ZnO nanowires. Figure 6.3a is a STEM image showing

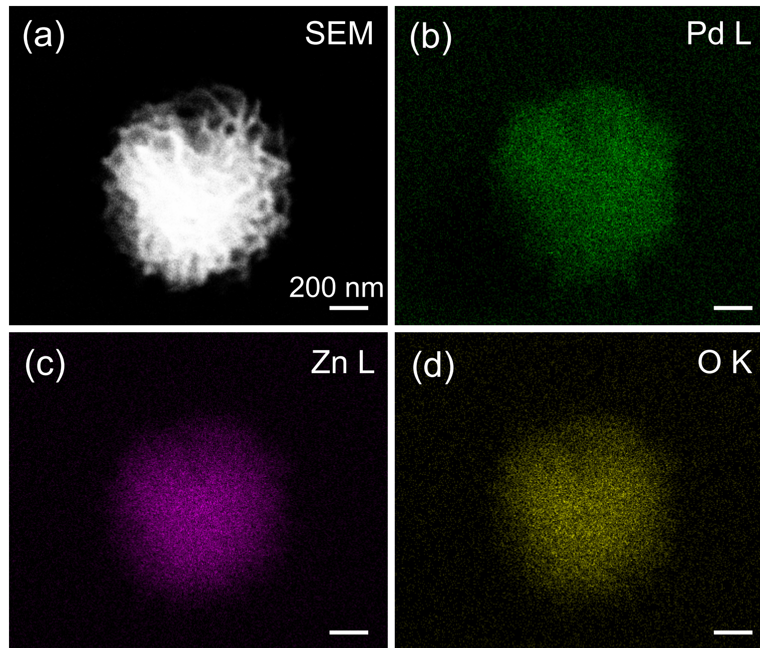

Figure 6.1: (a) SEM image of ZnO grown on patterned Pd. EDS maps of the patterned region (b) Pd L, (c) Zn L and (d) O K lines on the same region.

a collection of the nanowires. Similar observation is made from the TEM image shown in Figure 6.3b. A magnified image of the tubular structure along with a high-resolution micrograph with the d-spacing 2.47 $\AA$ is shown in Figure 6.3c.

When the reaction is allowed for longer time (45 minutes), the formation of dense fibril-like structures was observed as shown in Figure 6.4. From EDS analysis (shown inside), the atomic Zn:O ratio was obtained as 1:0.97 in the ZnO grown regions. XRD measurements on the ZnO structure grown on the Pd catalyst resembles the hexagonal phase of the ZnO (JCPDS 361451) with d-spacings of 2.47 and 1.62 $\AA$ for (101) and (110) planes, respectively, as shown in Figure 6.5a. The pattern showed the presence of Pd metal as well. Figure 6.5b shows the UV spectrum from the fibril structures with the optical band edge at 370 nm.

Photoluminescence measurements performed on the fibril nanostructures are shown in Figure 6.6 in comparison with the bulk ZnO (prepared by a solid state

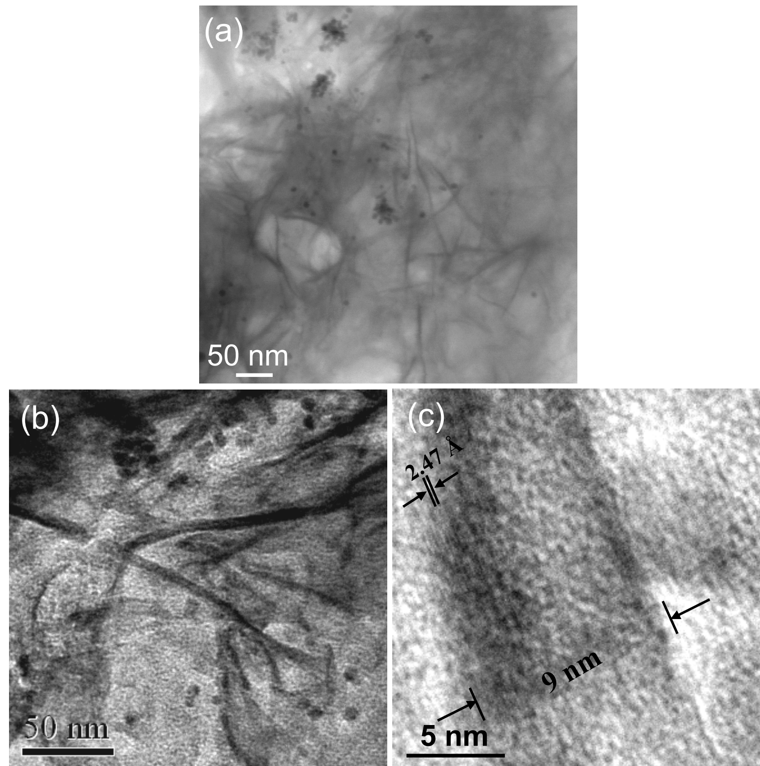

Figure 6.2: (a) STEM image, (b and c) TEM images of the ZnO structures.

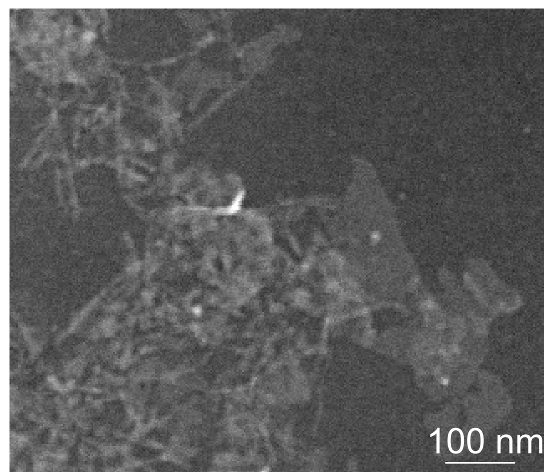

Figure 6.3: SEM image of ZnO nanowires grown on the thermolysed Pd film at 80 °C for 10 minutes.

method). The spectra have been collected by varying the source excitation energy from 280 to 335 nm. In the bulk ZnO (see Figure 6.6a), the main emission peak is

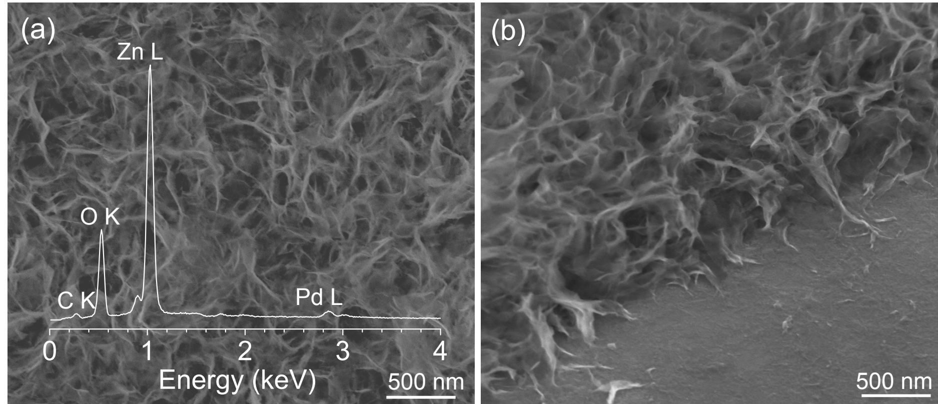

Figure 6.4: SEM images of ZnO fibrils grown on the thermolysed Pd film at 80 °C for 45 minutes (a) without and (b) with tilt and inset showing EDS spectrum.

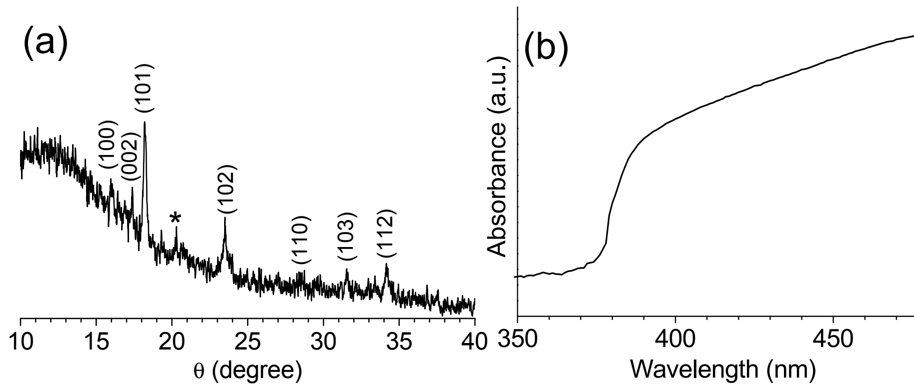

Figure 6.5: (a) XRD pattern of the ZnO nanostructures and (*) indicating Pd(111) peak. (b) Absorption spectrum recorded on the ZnO nanostuctures.

at 390 nm, corresponding to 3.39 eV band gap (see adjacent schematic energy level diagram) [133]. This remains unchanged when the excitation source energy varied. In the case of fibril structures, the emission peak is observed to blue shift from 390 nm with the increase in the excitation source energy (see Figure 6.6b). A simple explanation may be provided for this observation. In bulk ZnO, the main peak in PL corresponds to transition from bottom of CB to the top of the VB - optical band edge which are continuous. The nanostructures prepared in this study are small, <10 nm and the conduction and the valence bands are discretized into states with

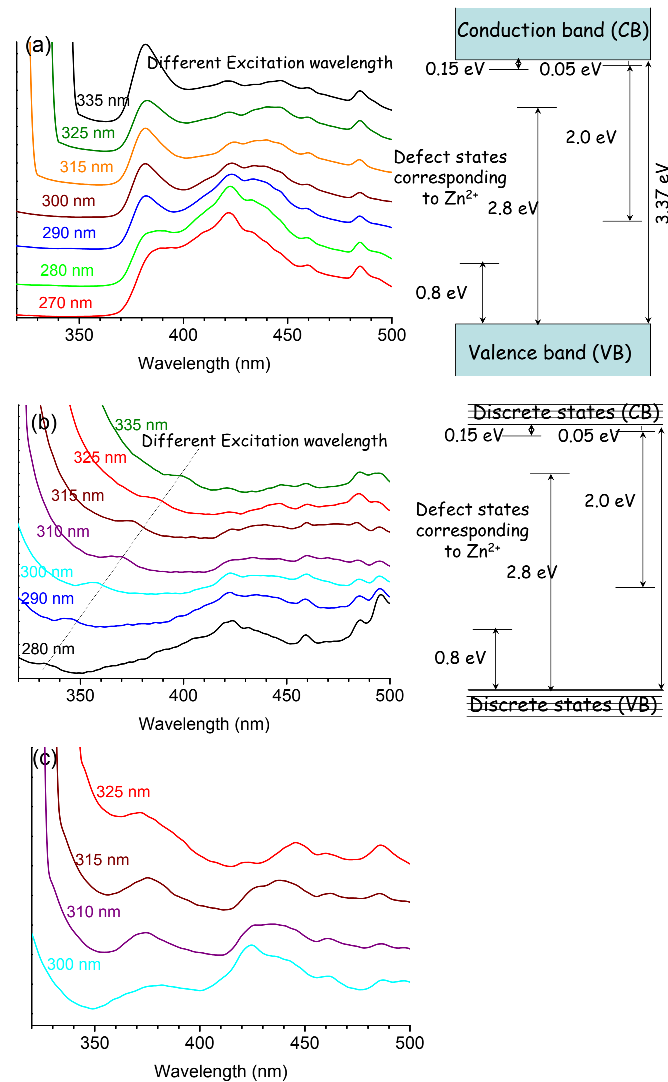

Figure 6.6: PL spectra recorded on (a) bulk ZnO, (b) ZnO nanostructures and (c) annealed ZnO nanostructures. The excitation source energy has been varied from 280 - 335 nm. Schematic energy level diagrams are also shown.

finite but small oscillatory strengths, hence wee much weaker peak intensities are seen. As the transitions originate from discrete states, the peak position shifts with the excitation source. This is a clear manifestation of the quantum confinement in the ZnO nanostructures containing defect electronic states. A shoulder is seen around 460 nm related to free-exciton recombination (i.e. radial recombination of

a photo-generated hole with an electron that belonged to a singly ionized oxygen vacancy in ZnO) [131, 132]. Annealing at 250 °C for 3 hours in oxygen resulted in more bulk like structure (see Figure 6.6c).

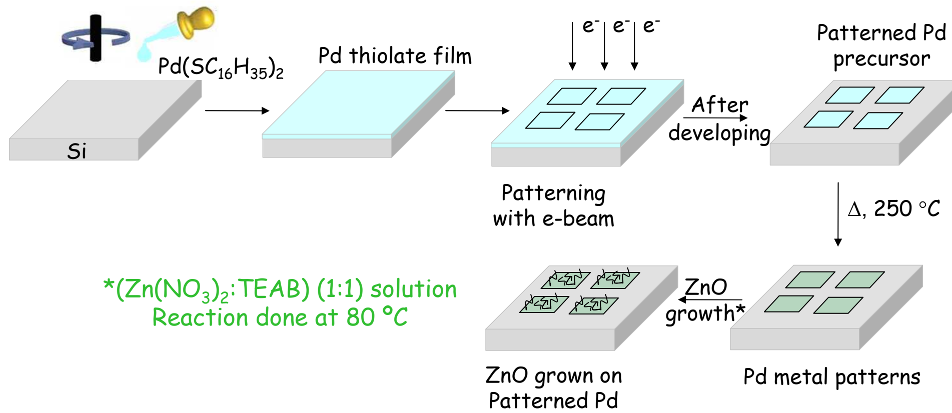

Figure 6.7: Scheme of the procedure adopted.

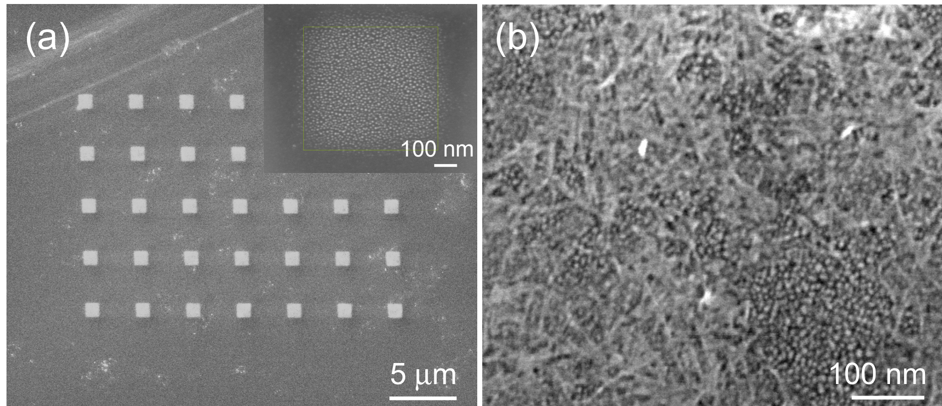

Figure 6.8: SEM image of the (a) patterned and thermolysed Pd film with inset showing magnified image of one island. (b) ZnO growth on the patterned region.

ZnO growth was attempted on the patterned Pd catalyst as well. Using direct write Pd patterning procedure(see section 4.4.2), which involves basically three steps (see Scheme in Figure 6.7), Pd metal was patterned. A Pd hexadecanethiolate film spin-coated on a Si substrate was patterned using a 5 kV electron beam at 135 $\mu C.cm^{-2}$ and developed in toluene. The regions exposed to the e-beam remained

on the substrate after developing thus indicating the negative-tone resist behavior of the thiolate. Under an electron beam, the hydrocarbon chains of the thiolate seem to develop defects and produce a disordered phase with decreased solubility in toluene. The e-beam may also promote radical formation and cross-linking of the alkane chains, essentially making it work as a resist. The patterned resist was subjected to thermolysis to yield Pd catalyst patterns (Figure 6.8a) an array of 7 x 5 islands with each island being 500 x 500 nm^2. Inset in the figure shows, a magnified image of an island with closed packed Pd nanoparticles with particle size $\sim$10 nm. Figure 6.8b reveals the growth of ZnO in the patterned region. The ZnO nanowires are typical 10 nm diameter and $\sim$0.5 μm in length.

6.5 Conclusions

Thermolysis of Pd hexadecanethiolate yields Pd metal. The thermolysed metal is free from sulfur and can be exploited as catalyst to grow various nanostructures. As Pd thiolate can be patterned using the electron beam directly, one can easily achieve patterned growth the nanostructures. ZnO has been grown on the thermolysed Pd using solution based method, as Pd can be patterned, patterned growth of ZnO is demonstrated. For a shorted duration of dip (10 minutes), fine ZnO nanowires of 10 nm are formed but for longer durations fibril like structures are formed. PL studies revealed that the quantum confined ZnO nanowires contain several defect electronic states.

CHAPTER 7

Nanocrystalline Pd and Au films as solid substrates for surface enhanced Raman scattering measurements and their nanopatterning leading to Raman chip fabrication

Summary*

Nanostructured surfaces of Au and Pd have been produced to serve as solid substrates in surface-enhanced Raman scattering (SERS) measurements. While Au based substrate was prepared by electroless plating on a Si substrate coated with amorphous carbon layer, the Pd substrate was obtained by simple thermolysis of Pd hexadecanethiolate film in air. The morphology of the surfaces could be well controlled such that at nanogranular size of 30-70 nm, the two surfaces showed maximum enhancement in Raman signal with thiophenol as the probe molecule. Besides the probe molecule, SERS from a number of biomolecules adsorbed on both the substrates was studied. Important characteristics of the substrates such as stability, robustness, sensitivity, biocompatibility, etc. have been examined in detail. The concept of a Raman chip as consisting of distinct well separated micro-regions - 'SERS bits', each being uniformly SERS active, is proposed.

*paper based on this work have appeared in Nanotechnology (2006), J. Phys. Chem. C (2006) and Small (2008). Another manuscript based on this work has been submitted.

In order to realize the same, Au and Pd substrates were patterned using EBL. While the patterning of Au substrates was mediated by polystyrene resist, in the case of Pd, hexadecanethiolate precursor itself acted as a direct write resist. The substrates with patterned regions were adsorbed with the probe molecule, thiophenol. The chip action is demonstrated by collecting Raman signal from the patterned SERS bits as well as from the regions in between. A small Raman library was created by adsorbing a number of biomolecules on the 'SERS bits', each carrying one type of biomolecule. Additionally, a study was carried on femtoliter capacity Ag cups prepared in the laboratory by pulsed laser ablation. The cups were found to be SERS active when examined after filling them selectively with thiophenol. These cups are suitable while dealing with small volumes of biomolecules.

7.1 Introduction

The last three decades have witnessed an ever-increasing interest in surface-enhanced Raman scattering (SERS) for trace analysis of molecules [134]. When adsorbed on metallic nanostructures, molecules exhibit an enhanced Raman signal usually several orders of magnitude higher compared to free molecules [135, 136]. Two main factors have been recognized as responsible for SERS, namely, the electromagnetic enhancement arising from local optical field resonance and the chemical enhancement due to interaction between the molecular states and electronic levels of the metallic surface. SERS is emerging as an important tool in biochemistry and medicine. It has found numerous applications in understanding antigen-antibody interaction,[137–139] DNA analysis[140] and discrimination [141], enzymology [142], in vivo studies [143], bacterial detection [144], photodiagnosis [145] and genomics [146].

Metal nanoparticles in the form of colloids are commonly being used as SERS active surface. Colossal enhancement is seen in such cases. The usage of sols however suffers from shortcomings such as inherent instability, poor reproducibility, and the necessity of external agents [134]. SERS enhancement, G, is defined as the ratio of the Raman-scattered intensity of the analyte in the presence of the enhancing medium to its value in the absence of the medium. To calculate the enhancement factor (G), the following procedure suggested by Yu et al.[147] has been employed

$$G = (I_{SERS}/I_{norm})(N_{bulk}/N_{surf}) \tag{7.1}$$

where I_{SERS} is the measured SERS intensity for the probe molecules on the nanocrystalline metal surface, I_{norm} is the measured intensity of normal Raman scattering from the bulk sample, N_{bulk} is the number of the probe molecules under laser illumination in the bulk sample, and N_{surf} is the number of molecules probed on the nanocrystalline metal surface. N_{surf} is given by

$$N_{surf} = 4\pi r^2 CAN \tag{7.2}$$

where r is the average radius of the nanocrystals, C and A are the surface density of the probe molecule and area of the laser spot on the sample, and N is the surface coverage of nanocrystals on the surface respectively. N_{bulk} is given by,

$$N_{bulk} = Ah\rho/m \tag{7.3}$$

where A and h are area and the penetration depth of the laser spot and ρ and m are the density and the molecular weight of the probe molecule, respectively.

In this context, solid substrates have been more promising. The Raman signal

enhancement reported for commonly used nanostructured metals Au and Ag is in the ranges of 10^5-10^9 and 10^8-10^{12} respectively [134]. Roughened electrode surfaces of Cu, Ag and Au have been tried out by Chase et al.[148] for wavelength dependent SERS on chemisorbed pyridine. Several other metals have also been tried out. These include Pt, Ru, Rh, Fe, Co, Ni, and their alloys, with enhancement factors ranging from 10^2 to 10^6 [149, 150]. Pd is a new SERS member. Pd nanoparticles deposited on a glassy carbon surface were found to exhibit a same SERS activity [151]. Abdelsalam et al.[152] found a 10^3 enhancement on electrodeposited Pd, while Liu et al.[153] reported SERS activity to be an order higher on an electrochemically roughened Pd surface. Li et al.[154] fabricated a SERS substrate by electrochemically depositing Pd onto an indium tin oxide glass substrate modified with a film of polypyrrole or polyaniline. The enhancement factor reported was $\sim 10^5$. Being an important metal catalyst, Pd-based substrates offer the additional advantage that the species under growth can be effectively studied using SERS.

Nowadays, there are sophisticated methods of lithographically imprinting metal nanostructures on solid substrates, with suitable morphology. Dieringer et al.[155] pioneered nanosphere lithography, which is a simple yet powerful approach to fabricate nanoparticle arrays with a precise control over shape, size, and interparticular spacing. Daniels and Chumanov[156] have prepared nanoparticle mirror sandwich structures in which coupling between a continuous metal film and plasmonic particles have been used for efficient SERS. Drachev et al.[157] have designed electron beam evaporated Ag films and demonstrated their biocompatibility and usage in enzymology. Lu et al.[158] have fabricated ordered, porous nanostructural films that exhibit excellent stability and reproducible properties. Recently, Kalkan and Fonash[159] have synthesized Ag nanoparticles on nanostructured Si films by an electroless method for surface enhanced molecular detection. Gunnarsson et al.[160]

employed EBL and made arrays of electromagnetically coupled Ag nanoparticles on silicon, while Félidj et al.[161] studied the optical response of EBL-patterned Au and reported an enhancement factor G of 10^5. SERS-active noble-metal nanostructures have been produced on Si surfaces by the galvanic displacement method [162]. Bartlett et al.[163] electrodeposited Au nanostructures using the nanosphere lithography technique.

7.2 Scope of the Present Investigation

It is important to understand the methodology through which one can control and maximize the enhancement factor to rationally design an SERS substrate. The present investigation deals with the development of a simple chemical method for morphology controlled SERS substrates of Au and Pd. Until now, nanolithography techniques have been extensively used to control morphology for optimal SERS activity. Here, the lithography method has been applied for the SERS substrate with a different objective. The concept of having many SERS active regions on a same substrate has been explored by performing EBL on the SERS active substrates where each patterned region potentially acts as a SERS active region, thus leading to the concept of a Raman chip. In another study, femtoliter metal cups of Ag produced by laser ablation [164] have been tried out for their SERS activity, with the objective of using them as small metal containers for biological studies.

7.3 Experimental Details

7.3.1 Preparation Au/C/Si substrates

Si substrates were cleaned by sonicating in acetone and doubly distilled water and dried under flowing argon. Carbon coating on the substrates was carried out in a vacuum chamber (10^{-6} Torr) using the pulsed laser deposition method. A frequency tripled Nd:YAG laser (Quanta-Ray GCR-170, Spectra-Physics, USA) with a pulse energy of 100 mJ and a repetition rate of 10 Hz was used for the ablation of a graphite target. Four substrates with 5, 15, 30 and 60 minutes of deposition of carbon were prepared. In order to facilitate the measurement of the thickness, a step was created by partially masking the Si substrates with a teflon tape during deposition. The four substrates were then subjected to gold deposition for 120 minutes in a plating solution in a teflon container. The plating solution consisted of 0.1 mM $KAuCl_4$ in 5 M HF. A Si substrate was similarly deposited with metal, but with no carbon loading and was used as a control. After 120 minutes, the substrates deposited with the Au films were carefully rinsed with double distilled water and dried under Argon.

7.3.2 Preparation Pd substrates

Pd hexadecanethiolate, $Pd(SC_{16}HS_{35})_2$, was prepared following the procedure described in section 4.3. The Pd thiolate spin-coated as films on Si substrate and heated to 250 °C in air for 30 minutes.

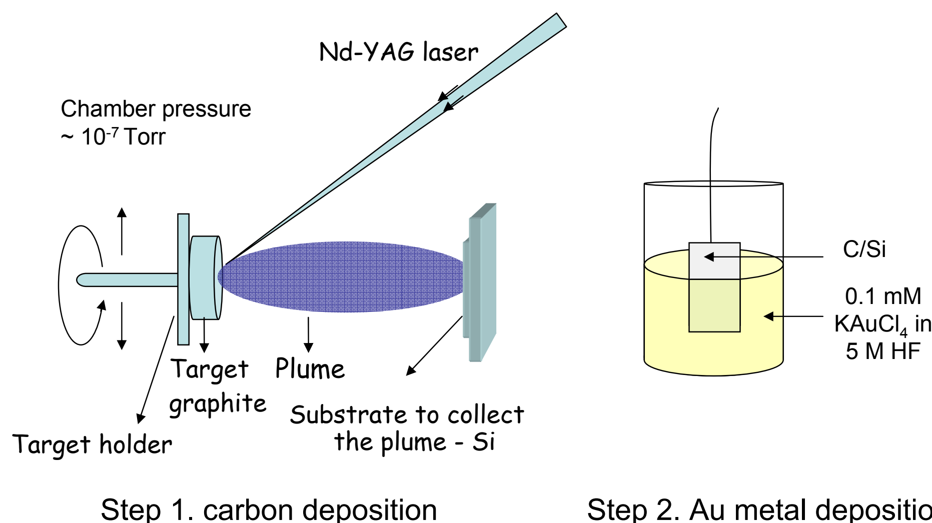

Figure 7.1: Schematic of the procedure adopted to obtain Au/C/Si substrate. Step 1. Pulsed laser ablation of graphite on Si substrate and Step 2. Au deposition from the plating solution (0.1 mM $KAuCl_4$ in 5 M HF).

7.3.3 Patterned SERS substrates

Au substrates

In order to fabricate a micro-arrayed SERS Au substrate, a carbon coated Si substrate (90 nm thick) was spin-coated with a 1% solution of a negative electron beam resist, polystyrene, at a rate of 3000 rpm. Electron beam lithography (EBL) was performed using FEI Nova NanoSEM 600 equipment (The Netherlands) (see section 1.6 for details). The electron beam energy employed for patterning was 5 kV. In a chosen area (150 x 120 μm^2), an array of 8 x 8μm^2 squares was patterned and developed in p-xylene and 2-propanol. The patterned substrate was deposited with Au in the plating solution for 120 minutes, as described in section 7.3.1.

Pd substrates

For patterning Pd, Si substrates were cleaned by sonicating in acetone and double-distilled wter and dried under flowing argon. The resist film (400 nm in

thickness) was made by spin-coating the Pd thiolate solution at 2000 rpm. An array of 6.5 x 6.5μm^2 square regions was exposed to an electron dosage of 135 μC.cm^{-2} at 5 kV. The substrate was then developed in toluene for 10 seconds and subjected to thermolysis at 250 °C in air for 30 minutes.

7.3.4 Raman measurements

Raman measurements were performed using LabRAM HR apparatus (Horiba, USA) with an excitation wavelength of 632.8 nm and 5mW.cm^{-2}. Signal accumulation was performed for 10 seconds with a spot size of ∼1 μm. For temperature dependent SERS, a Linkam cryostage TMS-650 (U.K.) was used. The probe molecules, thiophenol (TP), adenosine triphosphate (ATP), hemoglobin (Hb), myoglobin (Mb), adenine (A), uracil (U), cytosine (C), guanine (G), thymine (T) and rhodamine 6G (R6G) used in the experiments, were purchased from Sigma-Aldrich, USA. Molecules were adsorbed onto the substrate by dipping in 0.1 mM solutions for an hour. Later, the substrates were washed to remove the unadsorbed molecules from the surface.

7.4 Results and Discussion

7.4.1 SERS using Au/C/Si substrates

Prior to discussing Au deposition on carbon covered Si surfaces, the results obtained on the laser deposited carbon are presented in Figure 7.2. Under the given laser ablation conditions (see section 7.3.1), the thickness of the deposited layer as measured from profilometry increased at a rate of 3.16 nm.min^{-1} (see Figure 7.2a). Such a linear growth rate is typical of the laser deposition process

[165, 166]. Raman spectroscopy measurements have revealed the nature of the deposited carbon. From Figure 7.2b, it is seen that the spectra contain two broad bands [167–169], D and G at 1355 and 1575 cm^{-1} respectively, expected from laser ablation of a graphite target. With increasing thickness of the carbon layer, there is an expected increase in the spectral intensity but importantly, the intensity of the D peak is much higher, and both the peaks broaden. This observation suggests the presence of a significant portion of amorphous carbon in the deposited layer. The ratio I(D)/I(G) readily measures the disorder in the deposited carbon overlayer. In Figure 7.2c, we show that this ratio increases gradually at lower thicknesses and more rapidly beyond ~100 nm.

The presence of a carbon layer on Si substrate imparts different wetting properties during metal deposition from the plating solution. An experiment based on optical profilometry was conducted to seek more insight into the nature of the carbon layer (Figure 7.3). A Si substrate was fabricated containing four different regions, namely bare Si, Si with a carbon layer (C/Si) deposited for 30 minutes, Au deposited for 120 minutes directly on Si (Au/Si) as well as on C/Si (Au-C/Si) regions. The regions are clearly discernible in the photograph of the substrate shown in the centre of Figure 7.3. The optical profilometry measurements were carried out to measure the step across the boundaries of the different regions, Si-C/Si, C/Si-Au-C/Si, Au-C/Si-Au/Si and Si-Au/Si as shown in Figure 7.3. The step across the Si-C/Si interface (Figure 7.3a), due to the deposited carbon, measures 90 nm, consistent with the data shown in Figure 7.2a. Similarly, Au deposited on bare Si that was dipped vertically, distinguishes itself (see Figure 7.3b) with a step height of ~390 nm and a step width of ~11 μm. Here, the step width may be taken to represent the extent of wetting by the plating solution at the liquid contact boundary. On the contrary, we failed to see a distinct step at the boundary

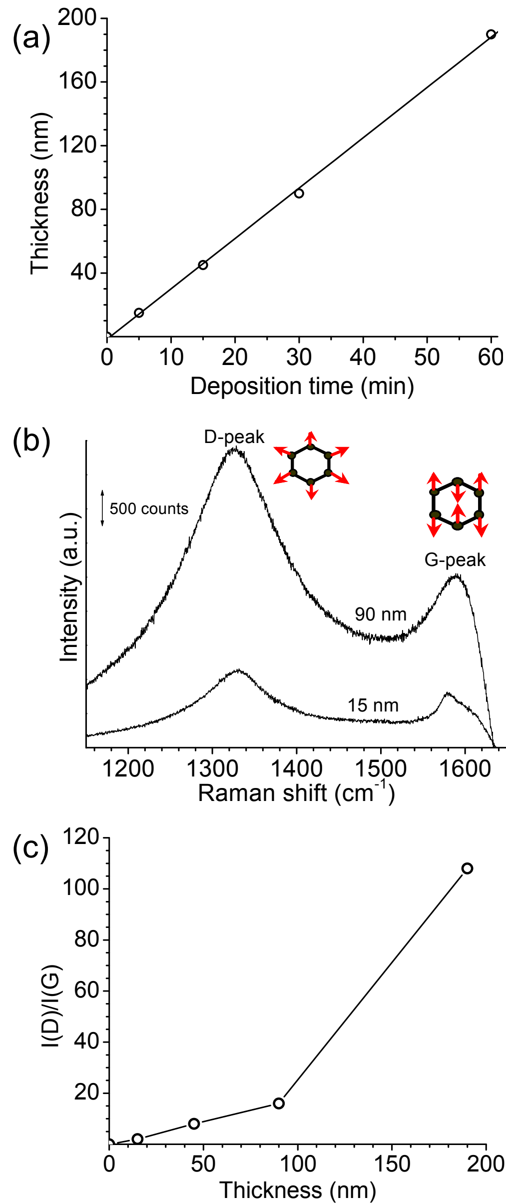

Figure 7.2: (a) Variation in the carbon layer thickness as a function of deposition time, (b) Raman spectra of carbon overlayers with varying thicknesses, 15 and 90 nm. Vibrational modes associated with D and G peaks are shown pictorially, (c) Variation in the ratio, I(D)/I(G) with the layer thickness.

between the C/Si and Au-C/Si regions (see Figure 7.3c), although the uptake of Au on carbon is vivid from the photograph shown (inset Figure 7.3). The absence

of a step between the regions Au-C/Si and Au-Si (Figure 7.3d) is a clear indication that at the air-liquid interface, the plating solution wets the C/Si region over a large range (not less than 60 μm) and as a result, the step becomes more diffused (see schematic diagram in Figure 7.3). In other words, the amorphous carbon layer seems to provide capillary pores for the Au^{3+} ions to diffuse across large length scales. The process observed here somewhat relates to Au reduction in the porous channels of nanostructured TiO_2 [170]. For the same reasons, the step between the Au/Si and Au-C/Si regions was also not distinct (Figure 7.3d). It may be noted that the Au-C/Si region in Figure 7.3 appears to have more luster than the electroless Au itself (Au/Si region).

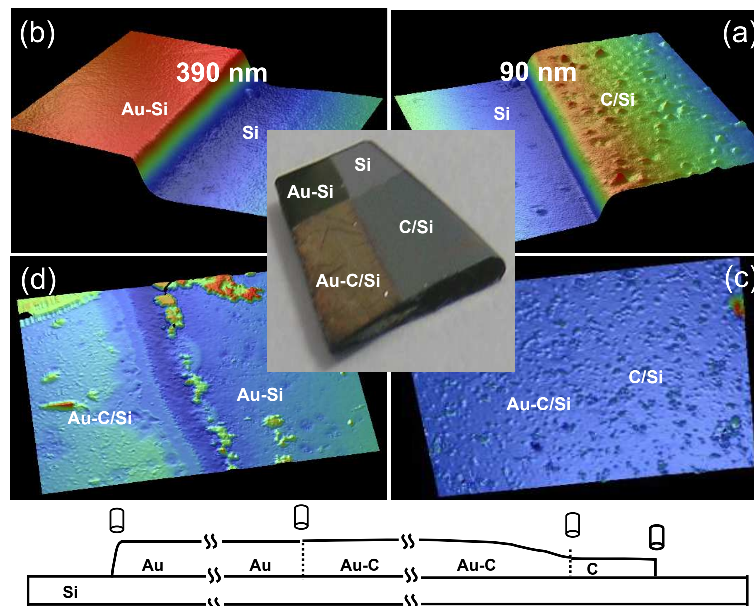

Figure 7.3: Profilometric measurements across different regions on the Si substrate (a) Si - C/Si, (b) C/Si - Au-C/Si, (c) Si - Au/Si and (d) Au-C/Si - Au/Si. Carbon deposition was carried for 30 minutes in the bottom half portion of the substrate by selective masking, followed by Au deposition for 120 minutes in the right half portion. The inset at the centre shows a photograph of the substrate. Below is the schematic representation of the various interfaces viewed through the objective.

AFM images of the C/Si substrates following electroless Au deposition reveal a

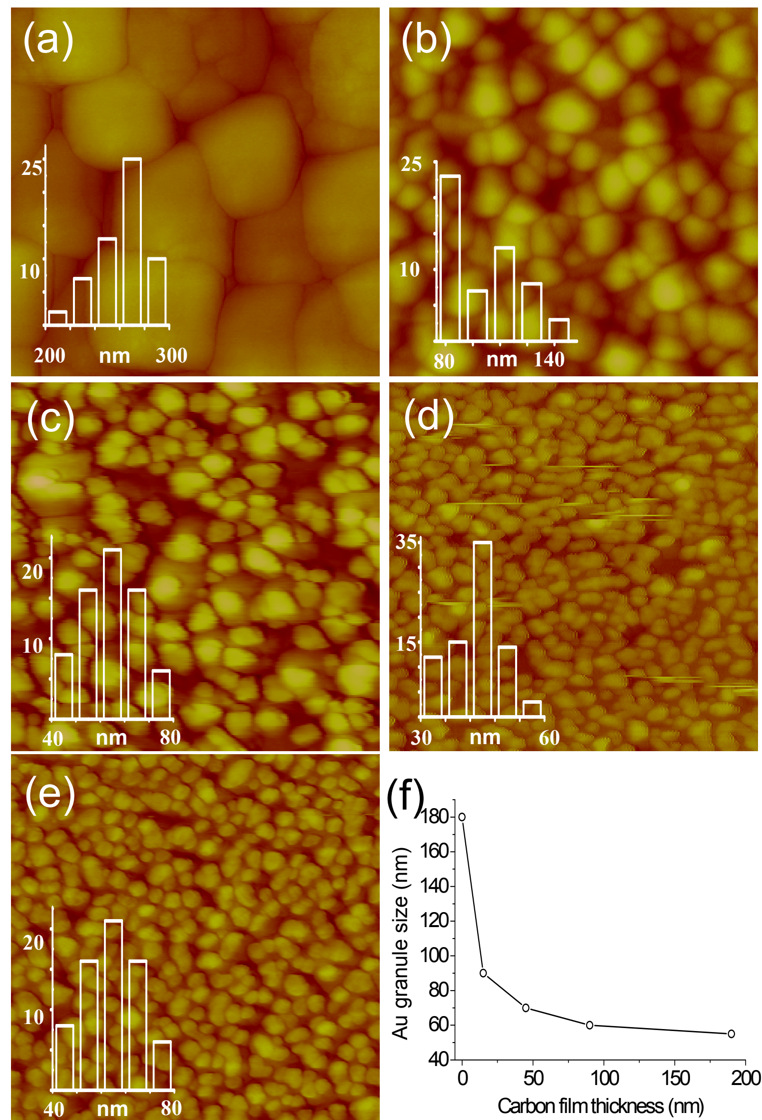

Figure 7.4: AFM images of Au deposited for 120 minitues on Si substrates covered with varying carbon layer thicknesses (a) 0 nm (b) 15 nm, (c) 45 nm (d) 90 nm and (e) 190 nm, respectively. Scan area 1 x 1 μm^2. (f) Variation in the granule size as a function of carbon layer thickness.

granular morphology as shown Figure 7.4. The granule size varies with carbon film thickness. In Figure 7.4a, Si substrate with no carbon layer, contains Au granules in the range 200-300 nm with a mean size of 280 nm and the large granules appear to be in close proximity to each other. With Carbon layer of 15 nm, the granules

size reduces to 80-100 nm (see Figure 7.4b). With higher carbon film thickness of 45 nm, the granules become much smaller in size (∼60 nm) (see Figure 7.6c) with increase in intergranular distance. Au granules of much smaller size, 30-60 nm with a mean size of 50 nm for 90nm thick carbon underlayer as shown in Figure 7.4d with the granule density of 500 granules.μm^2. Au deposits form close-packed granules of nearly uniform size with the granules are well separated with typical intergranular spacing of ∼7 nm. Finally, with carbon layer thickness of 190 nm, there is not much change in granule size, instead the density dropped to 400 granules.μm^2 (see Figure 7.4e) with intergranular distance being ∼15 nm. From AFM profile analysis the average thickness of the granules is found to be 19.5 nm for 190 nm thick carbon layer in contrast to 30 nm for a 90 nm thick carbon layer. Figure 7.4f is a plot of Au granule size variation as a function of carbon film thickness. It is note worthy that as the carbon film thickness increases, Au granule size decreases.

Core level spectral measurements were carried out in order to elucidate the exact chemical nature of the deposited Au on C/Si substrates as shown in Figure 7.5. The figure contains typical spectra without carbon (Figure 7.5a) and with 90 nm carbon overlayer (Figure 7.5b) along with the deconvoluted peaks, corresponding to the two Au species, Au^0 and Au^{1+}, ($4f_{7/2}$ at 84 and 85.5 eV, respectively). From Figure 7.5a, in the absence of a carbon deposit on the Si surface, the spectrum is found to be narrow and symmetric, containing mainly Au^0 species with a little intensity for Au^{1+} features arising because of surface carbon impurity. With precoated carbon of a 90 nm thickness (Figure 7.5b), the spectrum appears significantly broader with larger intensity at higher binding energies. The spectral deconvolution revealed the presence of considerable amounts of Au^{1+} species. As shown below, the presence of Au^{1+} species brings special properties to the substrate. The Au^{1+} is likely to originate from a surface Au carbide species. Thus, it appears that a

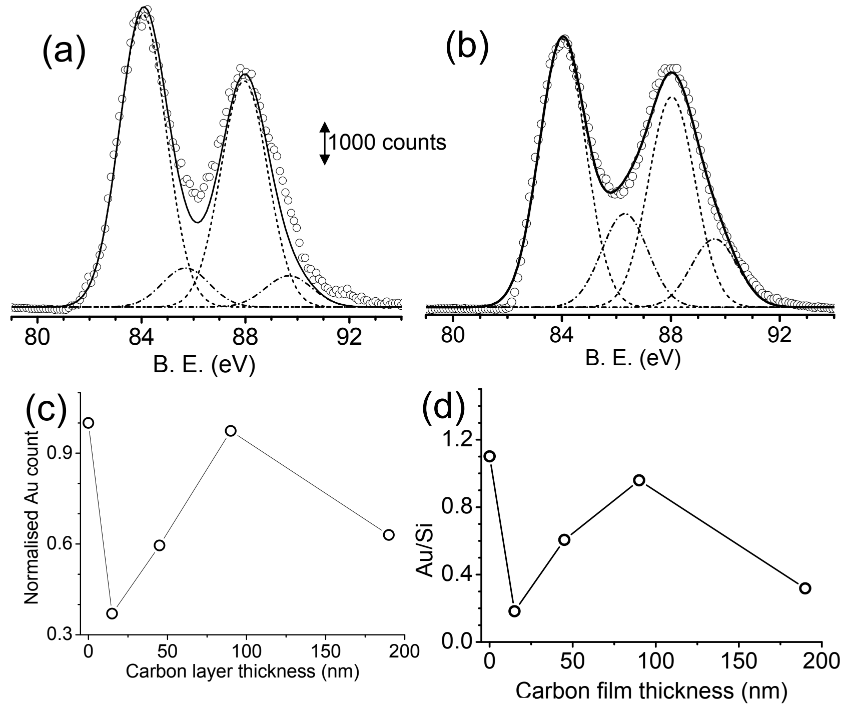

Figure 7.5: XPS Au(4f) core level spectra along with the deconvoluted peaks corresponding to Au^0 and Au^{1+} from substrates with carbon film thickness (c) 0 nm and (d) 90 nm and Au deposition carried out for 120 minutes. The deconvoluted peaks correspond to Au^0 (dash) and Au^{1+} (dash dot) species. (c) Total Au intensity plotted against carbon layer thickness and (d) Variation in Au/Si atomic ratio with carbon layer thickness from EDS analysis.

few atomic layers at the surface interact with carbon, giving rise to the carbidic species. The ratio, Au^{1+}/Au^0, calculated based on the spectral intensities is 0.34 and is found to vary in the range 0.32-0.38 for the different Au films. Interestingly, the total Au spectral intensity for different thicknesses of the underlying carbon layer (Figure 7.5c) shows a trend akin to the EDS data shown in Figure 7.5d. The EDS analysis reveals that the uptake of Au as measured from the atomic ratio, Au/Si, varies remarkably among the different substrates. For the substrate with no deposited carbon, its value is 1.1 but in the presence of a 15 nm carbon layer on the substrate, it decreases sharply to 0.2. This is understandable, as much of the adsorbed atomistic carbon may block the Si surface sites for Au^{3+}

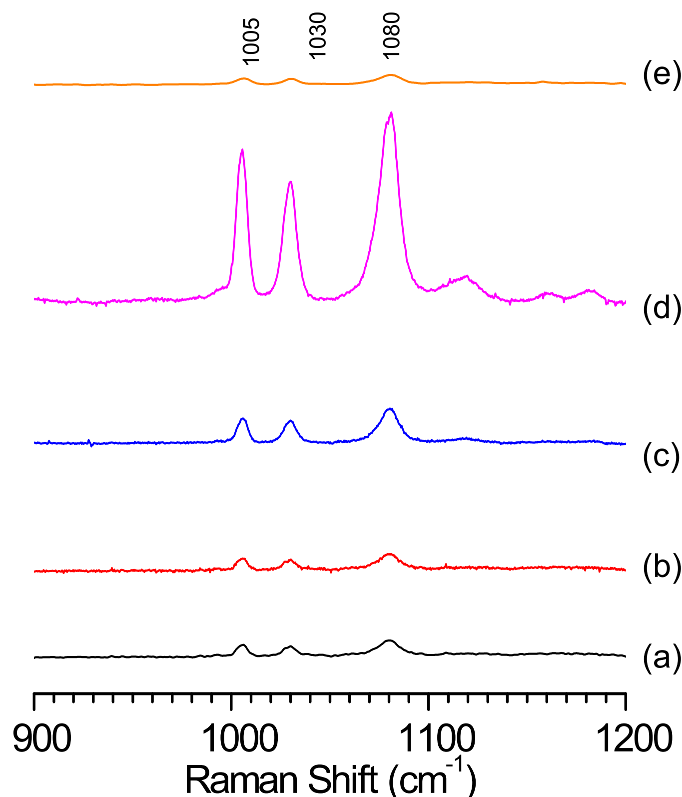

Figure 7.6: SERS spectra of thiophenol on Au deposited for 120 minutes on Si(100) substrates covered with varying carbon layer thicknesses (a) 0 nm (b) 15 nm, (c) 45 nm (d) 90 nm and (e) 190 nm, respectively.

reduction. Interestingly, with increasing carbon layer thickness, the Au/Si ratio starts to increase, reaching a maximum value of 1.0 in the case of the 90 nm thick carbon layer, which is close to that of the bare substrate. From Figure 7.2c, the amorphous carbon with high I(D)/I(G) values present at higher thicknesses, allows facile reduction of Au^{3+} at the Si surface. However, for the substrate with a carbon layer of 190 nm, the Au/Si ratio declines to 0.3, comparable to that of the 15 nm carbon layer. Although the I(D)/I(G) ratio is increasing, the diminished uptake of Au in this case may be merely due to the thickness itself.

Figure 7.6 shows the SERS spectra in the range 900-1200 cm^{-1} from Au/C/Si

substrates adsorbed with the analyte, thiophenol. The spectral features matches well with the reported values in literature [171]. The peak at 1005, 1030 and 1081 cm^{-1} correspond to C-H ring breathing, C-H ring aromatic and puckering mode respectively. The Raman enhancement is clearly evident as the spectral intensities increases with the increase in carbon film thickness. Inserting the following values in equation 7.2 and 7.3 for thiophenol molecule,

C the surface density of thiophenol, (6.8 x 10^{14} molecules cm^{-2})

A area of the laser spot on the sample, (4 μm^2)

h the penetration depth of laser, (100 μm),

ρ is the density of thiophenol, (1.073 g.cm^{-3}), and

m the molecular weight of thiopehnol, (110.18 g.mol^{-1}),

the enhancement factor obtained for the Au-C/Si (90 nm) substrate is 1.04 x 10^7.

Other important design aspects for designing a SERS substrate are its robustness with respect to temperature and the detection limit. These aspects have been studied on the prepared substrates and the results are given in Figure 7.7. Ideally, one would prefer a substrate to behave consistently over a large range of temperatures. This is a crucial prerequisite for studying temperature-dependent phenomena like phase transitions. The Au/C/Si substrate with highest enhancement factor has been used for this purpose. Figure 7.7a shows the SERS spectra of thiophenol recorded between the temperatures 123 and 433 K. It can be clearly observed that the SERS spectra of thiophenol are unaffected over the entire temperature range. At 433 K, interestingly, the spectral intensity diminished primarily due to the thermal desorption of thiophenol. Thus, the substrate not only retained its original nature over the entire temperature range but also was sensitive to the desorption process. In order to actually determine the detection limit of the

substrate, rhodamine 6G was used as a probe molecule (Figure 7.7b). Different concentrations of R6G (10 μl of 10^{-5} to 10^{-11} M) were added to the substrate and the SERS signal was obtained. A plot of intensity under 1539 cm^{-1} peak versus concentration of R6G has been shown in Figure 7.7b. From the plot it is evident that it is possible to detect concentration as low as 10^{-11} M which corresponds to 3-4 molecules on these substrates.

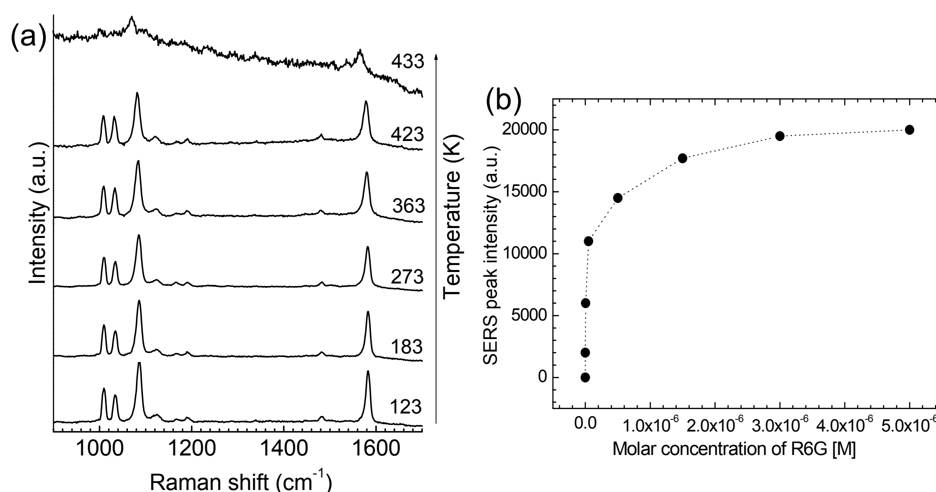

Figure 7.7: (a) SERS spectra of thiophenol between temperature ranges 123 K to 433 K and (b) R6G molecule detection limit by varying the molar concentration.

To test the versatility and biocompatibility, SERS on these substrates with molecules such as rhodamine 6G, myoglobin,and hemoglobin using a similar procedure adopted in the case of thiophenol was performed. The spectral features of the various analytes shown in Figure 7.8 are similar to the earlier reports [174–176]. Interestingly, the SERS spectra of myoglobin and hemoglobin closely resemble the solution-phase spectra, suggesting that the protein structure is intact upon adsorption onto the Au substrate. As can be seen, the spectra present a high contrast and are free from any fluorescence background. SERS of pyridine molecule is also shown and the spectral features match well with the reported values [177]. The

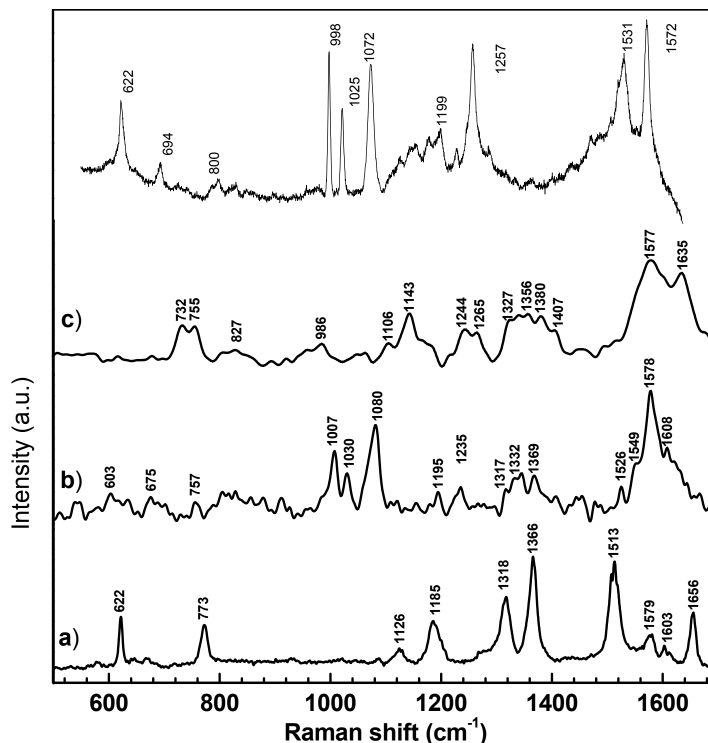

Figure 7.8: (a)SERS spectra of (a) rhodamine 6G (R6G), (b) myoglobin (Mb), (c) hemoglobin (Hb) and (d) pyridine (py).

substrates were stored in a closed container under ambient conditions over a period of 6 months and were tested for stability. The variation in the enhancement factor was less than 5%, emphasizing their robustness and long shelf life.

7.4.2 SERS using Pd substrates

As explained in section 4.4.1, thermolysis of Pd hexadecanethiolate at 250 °C in air yields Pd metal nanoparticles formation. In this study, these nanoparticles has been tried out for SERS. In Figure 7.9, the morphology and SERS spectrum carried out on one such thermolysed Pd are shown. The formation of nanoparticles in the range of 20-50 nm is evident from SEM image in Figure 7.9a. Raman spectrum of thiophenol chemisorbed on a thermolyzed film on a glass substrate (Figure

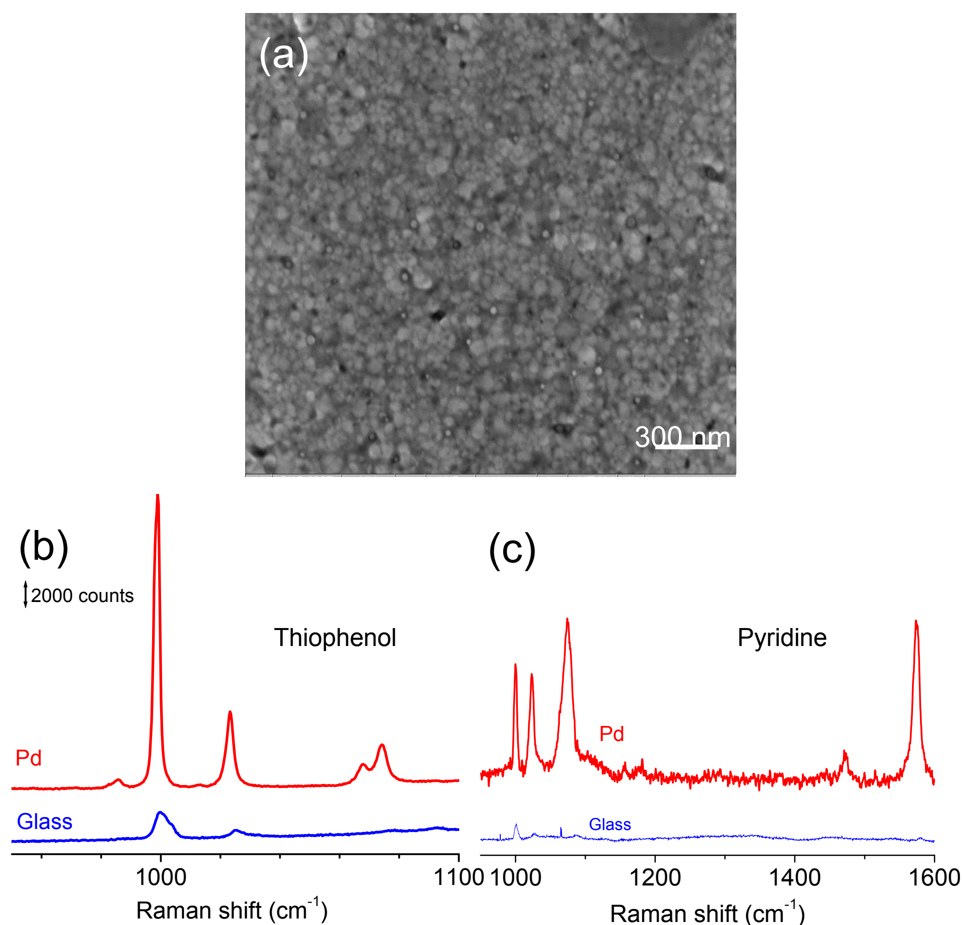

Figure 7.9: (a) SEM image of thermolysed Pd film. Raman spectrum of (b) thiophenol and (c) pyridine chemisorbed on Pd substrate.

7.9b) is compared with the spectrum from neat thiophenol. The peaks at 1005, 1028, and 1079 cm^{-1} correspond to ring breathing, C-H bending, and C-S stretching modes, respectively. The surface enhancement of the Raman signal from the thermolyzed film is remarkable, as the peaks are sharp and intense. As the peak positions are not much affected, this enhancement must be only due to the electromagnetic coupling. The particle size being 20 - 50 nm, such a high response may be expected [134]. The enhancement factor, G estimated from this measurement is 1.2 x 10^5. Similarly, pyridine molecule had been adsorbed and the spectrum is shown in Figure 7.9c. The enhancement factore obtained is considerably higher

than the literature values for Pd substrates of 5.5 x 10^2, 1.8 x 10^3 and 1.8 x 10^3 from Gómez et al.[151], Abdelsalam et al.[152] and Liu et al.[153] respectively, but is comparable to that obtained by Li et al.[154] (1.7 x 10^5).

7.4.3 The concept of a Raman chip

Having achieved high Raman activity with nanocrystalline Au and Pd films, an attempt has been made to produce patterned arrays of the same, towards realization of a Raman chip. A patterned substrate may serve as a chip with bits that are SERS active. Here, the bits are essentially well-defined discrete areas capable of high Raman enhancement. It is important that the areas defining the bits are well separated, such that there is no smearing of Raman-active species from one bit to the neighboring bits. A micro-Raman probe would then facilitate discrete readout from the "SERS bits" (see Figure 7.10). With the advent of nanolithography techniques, it is easy to realize a centimeter-square chip with millions of SERS bits, each bit being fed with Raman-active species by selective deposition [172] or by nanopipetting [173]. The bit size is limited by the lateral resolution of the Raman probe and also of the feeding mechanism, besides the inherent limitation imposed by the strength of the optical coupling required in the Raman process. For this

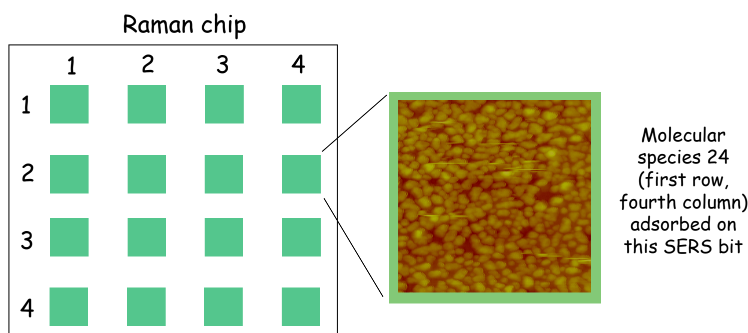

Figure 7.10: A Raman chip.

purpose, the Au/C/Si substrates were patterned as explained in the experimental section (section 7.3.1) and the schematic is shown in Figure 7.11. Briefly, after carbon film deposition, polystyrene solution is spin coated and used. The polymer is patterned using e-beam and developed and subjected to metal deposition. To check the SERS activity on the patterned substrate, the whole substrate was dipped in the analyte solution, namely thiophenol and Raman measurements were carried out.

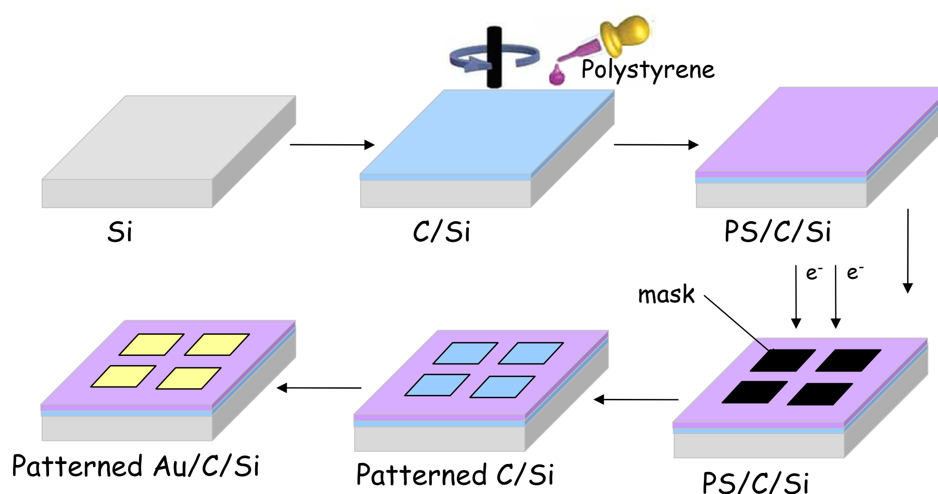

Figure 7.11: Schematic of the procedure adopted to obtain patterned Au/C/Si substrates.

Figure 7.12 shows SEM image of well-formed 8 x 8 μm^2 metal islands separated by ~12 μm. The intervening region is not completely devoid of the metal, but is thinly populated with small Au deposits. Riding on the 1080 cm^{-1} mode of thiophenol, the Raman signal intensity was collected from various locations (1-10) on and off the islands (See Figure 7.12). Regions numbered 1, 3, 5, 7, and 9 corresponding to metal islands produced good intensity signals and the signal from the intervening regions 2, 4, 6, 8, and 10 is negligible.

When it comes to nanopatterning, direct-write resists offer greater advantages,

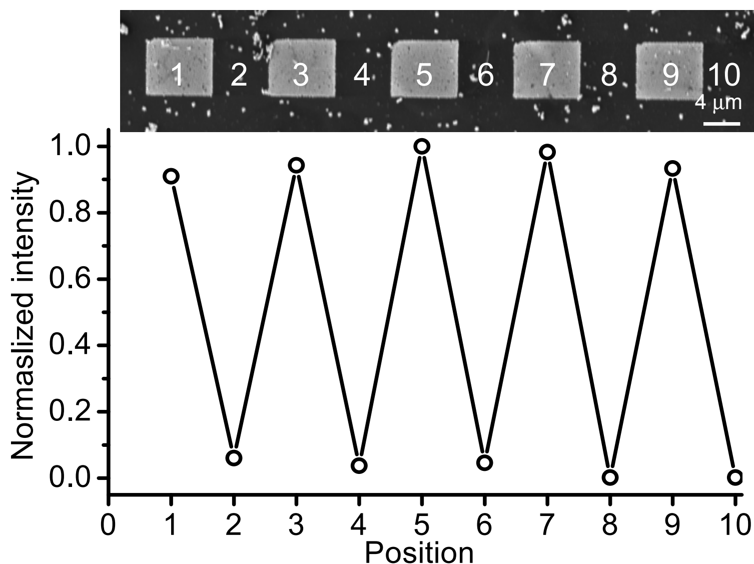

Figure 7.12: SERS spectra of thiophenol carried out in the micro-Raman array created by EBL on Au/C/Si substrate. The SERS signal has been normalized with respect to the maximum signal obtained for the region 5.

as the number of process steps would be minimal. Pd hexadecanethiolate, as explained in section 4.4.2, also behaves as a negative tone e-beam direct write resist. SERS bits of Pd have been fabricated direct write method using e-beam as shown in Figure 7.13. SERS study performed on a patterned Pd nanocrystalline substrate by adsorption of the probe molecule, thiophenol is shown in Figure 7.14. The pattern remained undisturbed following the analyte dosage. Well-formed 6.5 x 6.5 μm^2 metal islands separated by $\sim$ 7.5 μm was obtained. Riding on the 1005 cm^{-1} mode of thiophenol, the Raman signal intensity was collected from various locations (1-9) on and off the islands. Regions numbered 2, 4, 6 and 8 correspond to metal islands and produced signals of good intensity. The signal from the intervening regions 1, 3, 5, 7 and 9 is nearly absent, an important criterion for chip application. Another observation is that the Raman signal intensity is uniform ($\pm$ 5%) across the SERS bits, particularly in the case of Pd based chip. The stability of the signal without any 'hotspots' is another important attribute for quantitative applications.

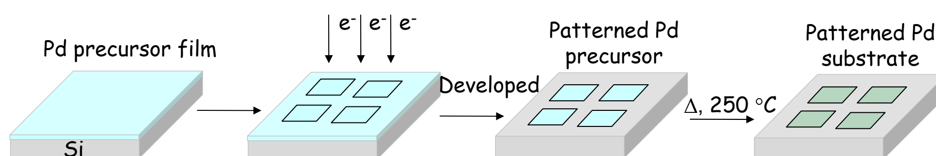

Figure 7.13: Schematic of patterned Pd substrate preparation.

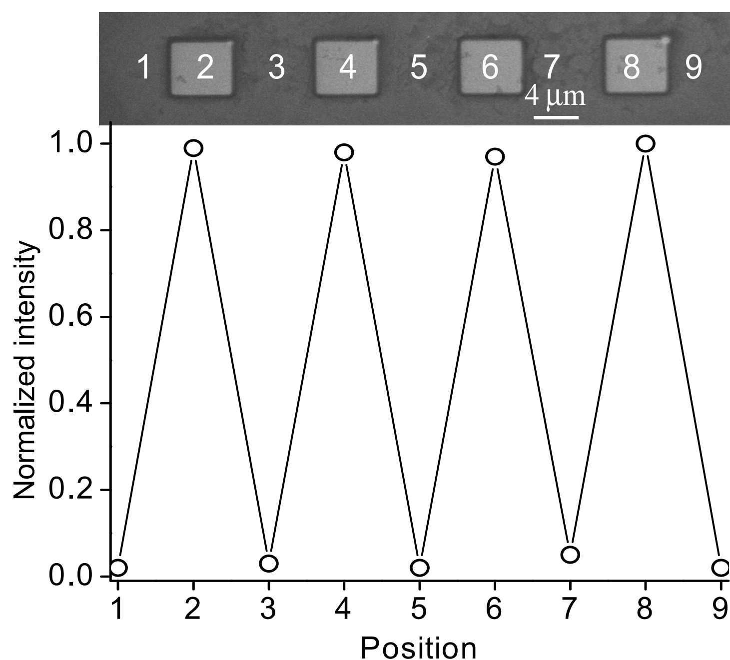

Figure 7.14: Raman spectral intensity at the 1005 cm^{-1} mode of thiophenol adsorbed on the SERS active regions called 'SERS bits'. The intensity values have been normalized with respect to that on bit 8.

To promote its application as a Raman biochip, the SERS bits were dosed with solutions of various biomolecules: haemoglobin (Hb), myoglobin (Mb), and the base pairs adenine (A), uracil (U), cytosine (C), guanine (G), and thymine (T). The spectral features of the various analytes shown in Figure 7.15 are similar to those of earlier reports [174–176, 178, 179]. The spectra present a high contrast and are free from any fluorescence background. Interestingly, the SERS spectra of Hb and Mb closely resemble the solution-phase spectra, which suggests that the protein structure is intact upon adsorption onto the Pd substrate. The Fe-spin

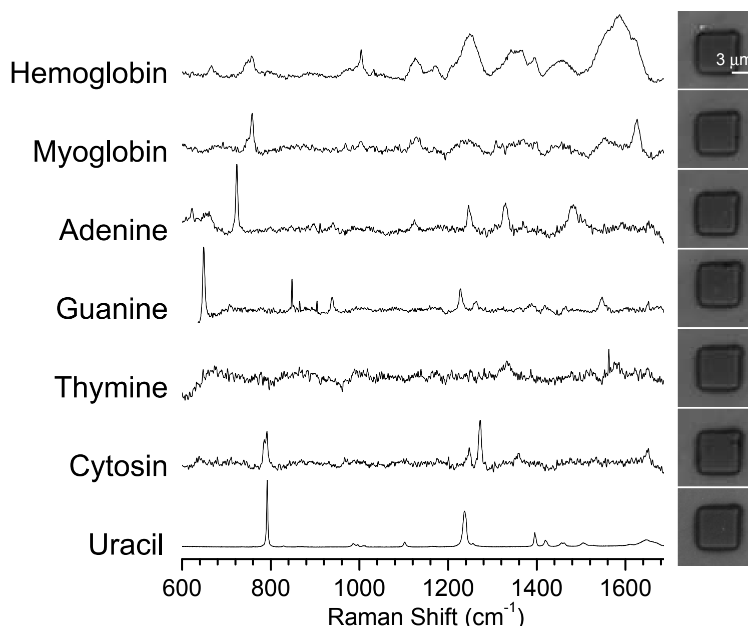

Figure 7.15: SERS spectra of haemoglobin (Hb), myoglobin (Mb), adenine (A) guanine (G), thymine (T), cytosine (C) and uracil (U). SEM images of the 'SERS bits' are collated alongside of the spectra.

marker mode around 1640 cm^{-1} is seen in both cases [178].The ring bending modes and C-N and C=O stretching modes of all the base pairs match well with the values reported in the literature (see Table 7.1).

7.4.4 SERS on Femtoliter Ag cups

Figure 7.16 illustrates the preparation of the cups obtained from the pulse laser ablation of a Ag foil [164]. The SEM image in Figure 7.17a shows that the cups have a diameter in the range of 2-15 μm with internal volume in atto to femtolitre range. The cups were filled with the molecules, when the whole substrate was dipped in a thiophenol solution and lifted horizontally upward to ensure some entrapment of the liquid for SERS measurements.

Raman measurements carried out on thiophenol filled Ag femtolitres metal cups

Table 7.1 Surface enhanced Raman Scattering band assignments for the base pairs.

Adenine	Cytosine	Guanine	Thymine	Uracil	Raman modes
1653	1651	1652	1650		$\beta_s(NH_2)$ NH_2 Scissoring
				1648	ν_s(C=O) C=O Stretching
1594		1547	1585		$\delta(NH_2)$ NH_2 Deformation
1552		1486		1534	Ring Stretching (Py)
	1540				$\delta(NH_2)$ NH_2 Deformation
					ν_s(C=N) C=N Stretching (Im)
1482	1458	1353	1477	1435	ν_s(C=N) C=N Stretching (Py)
		1410		1419	$\nu_s(C_4C_5)$ C-C Stretching
			1386		$\delta(CH_3)$ CH_3 Deformation
1372	1360			1395	$\nu_s(C_6N_1)$ C-N Stretching (Py)
		1323	1332		ν_s(C-N) C-N Stretching (py)
1329					ν_s(C-N) C-N Stretching (Im)
	1272	1263		1235	$\nu_s(C_2\text{-}N_3)$ C-N Stretching
1246	1247	1227	1235		$\nu_s(C_8\text{-}N_9)$ C-N Stretching
		1179	1208		ν_s(C-C) Ring-CH_3 Stretching
1123	1107	1095			$\nu_s(C_5\text{-}C_6)$ C-C Stretching
1035		1015	1017	986	ν_s(N-C) N-Sugar Stretching
940	966	938			$\rho(NH_2)$ NH_2 Rocking
		847			ν_s(N-C-N) N-C-N Stretching
720	791		784	795	Ring breathing (Py)
		647			Ring breathing (Im)

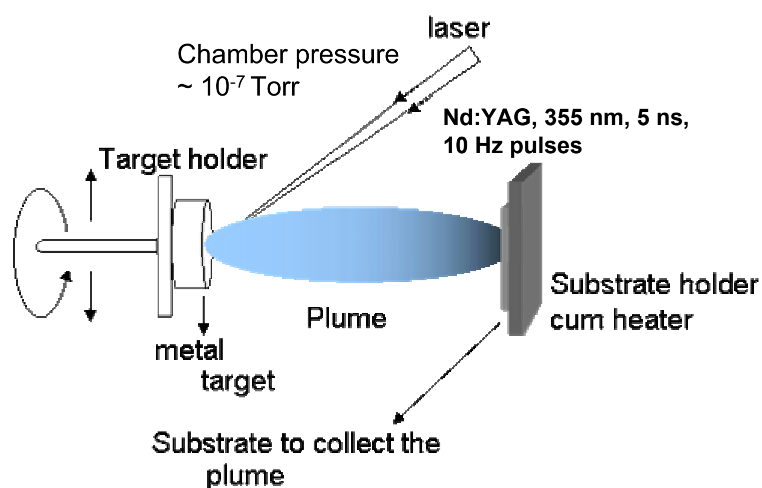

Figure 7.16: Schematic of the laser ablation of Ag metal to obtain femtoliter cups.

are shown in Figure 7.17b, along with the optical images of the relevant cups. The Raman enhancement is clearly evident as the spectral intensities from both the

cups are much higher compared to that from the substrate. The enhancement factor in the two case is estimated to be $\sim 10^6$. Interestingly, metal cups showed no distortion or melting under the laser beam.

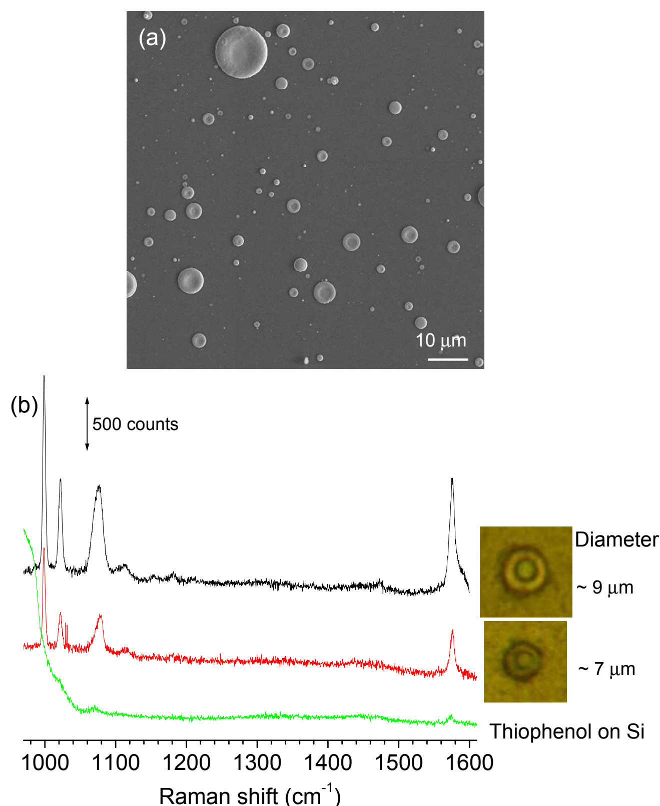

Figure 7.17: (a) SEM image of Ag femto-cups. (b) Raman spectra of thiophenol recorded on Ag femtoliter cups and on Si substrate along with their optical images.

While the above experiment was performed by immersing the whole substrate (along with the metal cups) into the analyte solution, another study was carried out by selectively dosing the cups with the molecules using a metal tip, much like a dip pen method [14]. This way, the potential utility of the cups in nanomolar assays could be successfully demonstrated. Figure 7.18 presents the SERS spectra along with the optical images. It is remarkable that considerable spectral intensity was observed with such small volume of the probe molecule (<1 femtoliter). Indeed,

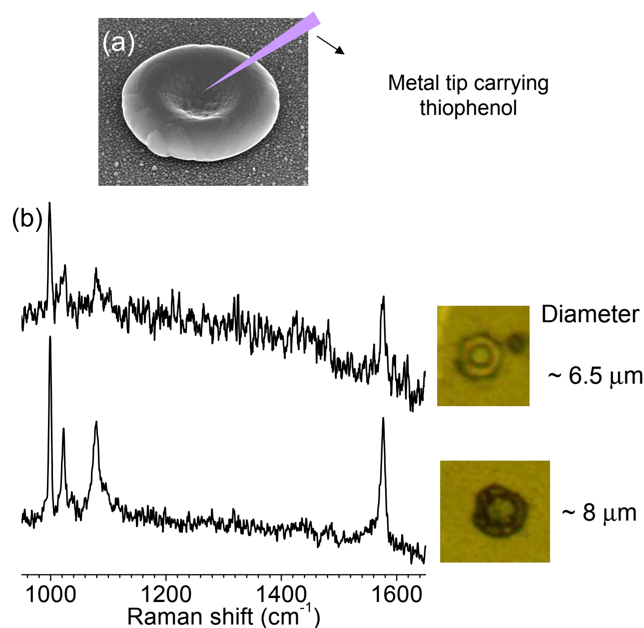

Figure 7.18: (a) An individual metal cup being fed with thiophenol using a micro-metal tip (the tip is shown schematically) and the analyte molecule was carried as an ink onto a sharp metal tip with diameter (∼1 μm). (b) Raman spectrum obtained from individual cups.

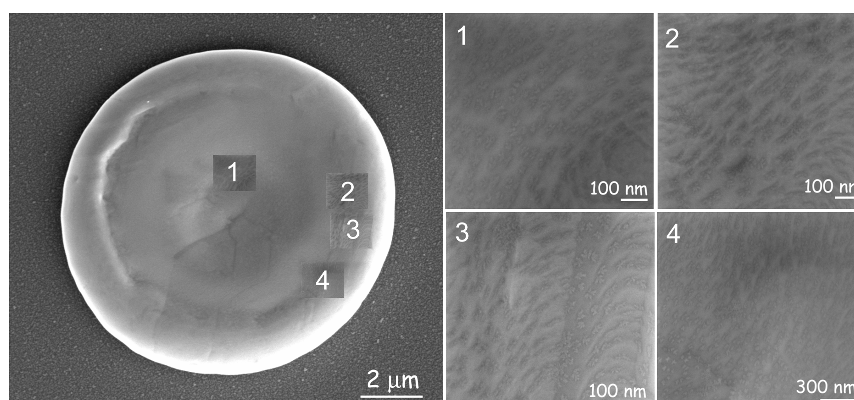

Figure 7.19: Topography of a femto-cup with magnified images showing the surface roughness.

the internal surface of the cups is SERS active.

The origin of the SERS activity from the cups is evident from the microscopy analysis of the cup surface. Figure 7.19 reveals that the cup surface is not really smooth but consists of aggregates of nanoparticles in the range of 30-40 nm. The

particles are oriented radially along the cup boundary with irregular shape. These features are borne out of the liquid metal flow pattern during the formation of the cups [164]. This degree of surface roughness is just apt for the SERS event.

7.5 Conclusions

In conclusion, the study on electroless plating of Au on carbon covered Si substrates has shown that the metal resides in the capillary pores present in the amorphous carbon matrix, its morphology being critically dependent on the thickness of the carbon layer. The Au deposition is optimal at a carbon layer thickness of 90 nm, where the deposited metal occurs as nanogranules of ∼65 nm in size with a spacing of ∼7 nm. Such a morphology of the deposit seems adequate for enhancing the Raman signal with an enhancement factor as high as 10^7. Temperature-dependent SERS measurements between 123 and 433 K reveal that the substrates are robust.

Thermolysed Pd thiolate films have been tried out as SERS substrates. Microscopic analysis has confirmed the nanocrystalline nature of the film with a particle size in the range of 20-50 nm. The Pd surface produced was SERS active with an enhancement factor of 1.2×10^5 for the probe molecule, thiophenol. The precursor, Pd hexadecanethiolate, behaves as an e-resist in direct-write EBL, which enabled patterning of Pd regions that were SERS active. Such regions may be termed 'SERS bits'. The bits on a chip were made to adsorb different molecules. Besides thiophenol and pyridine, various other molecules such as hemoglobin, myoglobin, and the nucleic acids adenine, guanine, thymine, cytosine and uracil were detected using both Au and Pd SERS substrates.

In another study, femtoliter Ag cups different sizes (2-15 μm), prepared by

the pulsed laser ablation were filled with the probe molecule, thiophenol either by dipping the substrate carrying the cups or by selectively dosing the cups with sharp metal tip, for SERS studies. SERS studies carried on these metal cups showed a typical enhancement factors of $\sim 10^6$ were obtained. This study not only demonstrates the utility of metal cups as small containers but also their high SERS activity, most desirable feature of a small container in biological studies.

CHAPTER 8

Self assembled circuits of multi-walled carbon nanotubes with Pd hexadecanethiolate as a nanosolder

Summary*

Carbon nanotube (CNT) circuits are made using Pd hexadecanethiolate as a soldering material. It was found that the thiolate not only served as a solder but also mediated self-assembly to CNTs to sit across the gap electrodes in a perpendicular and equally distributed fashion. The soldering action was realized by electrically activation or by heating at 250 °C resulting in ohmic contacts. The method is quite successful in fabricating single CNT circuits. The soldered CNT is shown to work as a fuse by passing high currents.

8.1 Introduction

Carbon nanotubes have been proposed as a prototype nanoscale building blocks because of their unique electrical and other properties. The nature of electrical conduction through a carbon nanotube (SWNT) crucially depends on its internal geometry, whether it is single walled (SWNT), double walled (DWNT) or

*A manuscript based on this work is under preparation.

multi walled (MWNT) and many other factors. The exploitation of the properties of carbon nanotubes is actively being pursued worldwide. An important aspect of this research is related fabrication of electrical circuits with carbon nanotubes as active elements.

Among the investigated methods, one can differentiate between such methods in which CNTs are randomly placed over a substrate and such methods in which CNTs are deposited onto a desired position. For the electrical contacting, randomly placed CNTs require a three-step procedure: In the first step the positions of the CNTs on the substrate are located by an AFM or SEM. In the second step, the located positions are marked and in the third step, the CNTs are contacted with the electrodes. The time intensive search is a major drawback. Additionally, such a method does not allow suspended CNTs deposition. Dohn et al.[180] used movable microcantilevers, which served as contacting electrodes. Instead of movable electrodes, Ebbesen et al.[181] and Schoenenberger et al.[182] formed metal electrodes on top of CNTs by focused-ion beam and evaporation, respectively.

Different methods for the deposition of CNTs directly to a desired position have been discussed in the literature. Lewenstein et al.[183] deposited CNTs over four prefabricated electrodes using amino-functionalized regions to which CNTs adsorb preferentially. Instead of using functionlized electrodes, Klinke et al.[184] functionalized the CNTs themselves. The functionalized CNTs were adsorbed by the designated areas and electrodes were built over the adsorbed CNT subsequently. Gao et al.[185] placed an individual CNT between two opposing metal electrodes and realized a four-point contacting. To achieve this goal, they placed two additional CNTs acting as electrodes on top of the first CNT by using an AFM. Li et al.[186] made use of a PDMS microchannel mold and directed SWNT into them by blowing gas and successfully transferred them between a pair of gap electrodes.

Another method employed is dielectrophoresis, in which an electric dipole of CNT is exposed to an inhomogeneous electric field to guide the CNT to specific electrode locations [187, 188].

The nanotube-electrode coupling is no less an issue. Bachtold et al.[189] exposed MWNT-Au electrode contact to electron beam in a SEM and observed decrease in contact resistance by several orders of magnitude due to pressure contact. EBID [190] has been employed to dump metal deposits at CNT-electrode junction. These deposits are truly metallic, nevertheless help in improving the contact. In another study, Au nanoparticle sol has been used as an ink to write with 'fountain pen' at the electrical contacts [191]. The electrical contact between CNTs and metal electrodes can also be improved by rapid thermal annealing [192].

8.2 Scope of the Present Investigation

There are several reports on the fabrication of CNT based circuits by selective masking [183], manipulating individual CNT to bring between designated electrodes[45], orienting them by applying external field [187, 188] and by simply pasting CNT film onto electrodes. Getting an individual CNT across the electrode has always been a tedious task. In addition, there are efforts to improve the CNT-electrode coupling by a metal containing on tip or by e-beam induced local coupling. As it is clear from these examples, there is no straight forward method of bringing in CNT into a circuit and solder it. The present work is aimed at building CNT circuits, particular single CNT circuit, through self-assembly. As such, self-assembly of CNTs across microchannels of PDMS is reported [193]. The present work exploited the self-assembly nature of Pd hexadecanethiolate in bringing CNTs across the gap between electrodes. The Pd precursor is also made to serve as a

nanosolder precursor. The recipe was first experimented with carbon microfibre, before applying it to CNTs.

8.3 Experimental Details

Several Au gap electrodes (50 nm thick) were deposited on glass slide using shadow masks with gaps of ∼1.1 mm and ∼9 μm, by physical vapor deposition. Carbon fibre (diameter, 7-8 μm) or multi-walled carbon nanotubes (Sigma Aldrich) of diameter 150 - 300 nm and length 7 - 12 μm were used as active elements across the gap electrodes. The Pd precursor, Pd hexadecanethiolate was used as a solder. An external multimeter (Keithley 236) served as the source and measurement unit for current-voltage characteristics. SEM images were taken using a Nova NanoSEM 600 equipment (FEI Co., The Netherlands) which allows low vacuum imaging for insulating samples and has an e-beam writer available to perform EBL (see section 1.6 for details).

8.4 Results and Discussion

8.4.1 Soldering a carbon fibre

To begin with, a carbon fibre (diameter, 7 μm) was placed using a forceps across a gap of 1.1 mm Au contact pads on a glass plate (Figure 8.1a). I-V measurement showed a non-linear behavior with a typical resistance of 0.1 MΩ around 1.5 V (see Figure 8.1b). A drop of Pd precursor in toluene was deposited at either end of the fibre. The circuit showed negligible current (see Figure 8.1c). The fibre lost contact with the electrode as the Pd precursor which is an insulator, seems

to have crept beneath the fibre. The glass substrate was heated at 250 °C for 10 minutes to bring about thermolysis of the Pd precursor resulting in metallic Pd. The I-V data following thermolysis is linear and the resistance measured is 200 Ω (Figure 8.1d). Instead of Pd hexadecanethiolate, when a commonly used conducting Ag paint was applied in this way, the resistance of the circuit was 15 kΩ, much higher than that obtained with the Pd precursor. This is understandable since Pd thermolysis leads to metallic Pd, while Ag paint often contains lot of hydrocarbons.

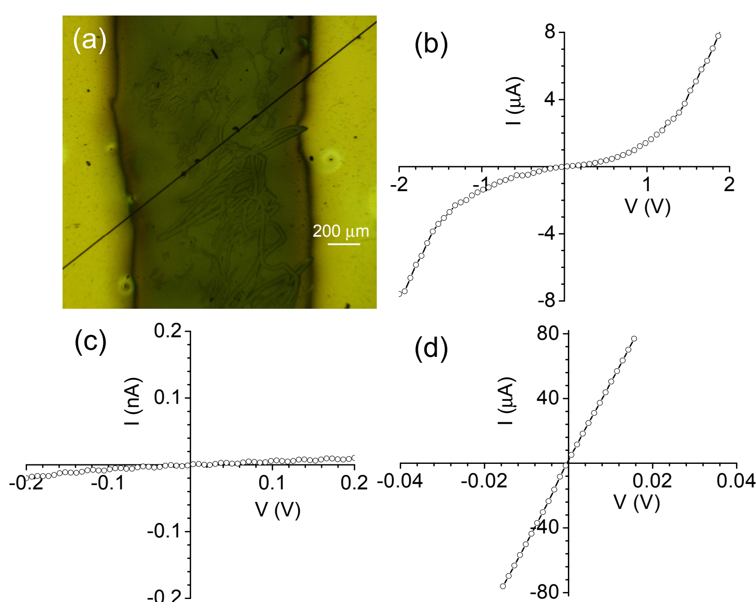

Figure 8.1: (a) Optical image showing the carbon fibre soldered on the Au electrode using Pd hexadecanethiolate. I-V characteristics of the carbon fibre (b) as-placed on the Au electrode, (c) after adding Pd precursor and (d) after thermolysis at 250 °C for 10 minutes.

In another experiment, a carbon fibre was placed between Au contact pads spin-coated with the Pd precursor (instead of pouring drops at both the ends). Initially, there was hardly any current in the circuit (see curve 1 in Figure 8.2a). An external bias of 30 V was applied for a few seconds and then the I-V measurement was done with a 1 V sweep (curve 2). The I-V data became linear with a resistance value of 4 kΩ. This observation is interesting, as in this case, the soldering action was

realized by electrical activation instead of thermolysis. Figure 8.2b shows the fibre on the electrode surface. In the inset is shown a close tilted view of the fibre. Pd metal aggregates resulting from the electrical breakdown of the Pd precursor are seen below the fibre. The higher resistance observed in this case (compared to that in Figure 8.1) is primarily due to the presence of carbon impurities along with the metal solder as the electrical activation need not remove them unlike thermolysis. These preliminary investigations of carbon nanofibre led to the study of CNT circuits.

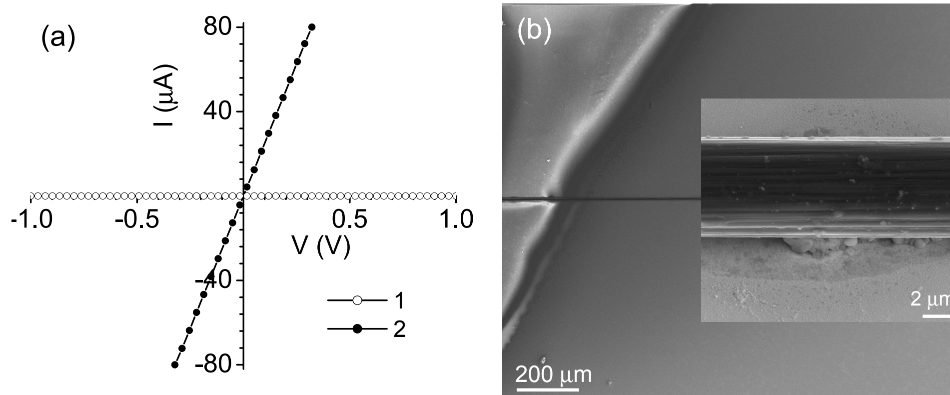

Figure 8.2: (a) I-V characteristics of carbon fibre soldered with Pd precursor spin-coated on the Au gap electrodes. Curve (1) carbon fibre physically placed, curve (2) after applying external bias. (b) SEM image showing the carbon fibre across the Au gap electrode and inset showing the soldering material holding the carbon fibre after application of external bias.

8.4.2 Self assembled and soldered CNT circuits

CNTs were drop coated from a CCl_4 dispersion on to 9 μm gap electrodes (see Figure 8.3a). I-V measurement showed a non-linear curve (see curve 1 in Figure 8.3b), indicating non-ohmic contact between CNTs and the Au electrodes. A drop of Pd precursor in toluene was then placed on top of the gap electrodes and the current dropped below 1 nA (see curve 2 in Figure 8.3b). The CNTs seem to

have lost contact as the Pd precursor creeps beneath. There was no response even after application of 200 V bias (see curve 3 in Figure 8.3b), unlike in the case of fibre where a 30 V activation was enough to establish a good contact (Figure 8.2). However, after a gentle wash in toluene, the I-V data became linear with resistance of 20 kΩ (see curve 4 in Figure 8.3b). The application of electrical bias is expected produce metallic species required for ohmic contact, much the way seen in the inset of Figure 8.2b, in the case of the fibre. CNTs, however, due to their size fail to establish contact with the metallic Pd species because the presence of hydrocarbon species around. A gentle toluene wash helps in getting rid of the hydrocarbons, allowing ohmic contact. The resistance measured is typical of CNTs.

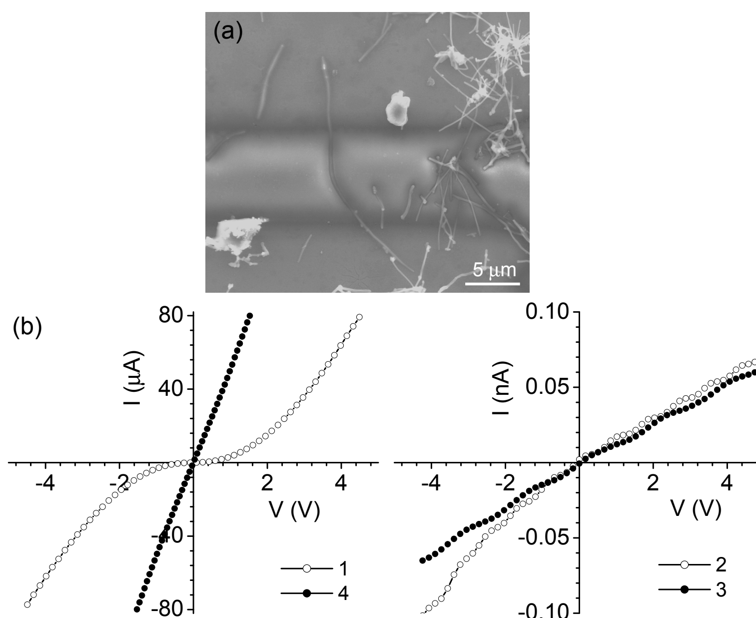

Figure 8.3: (a) SEM image showing bundle of CNTs across the gap electrode. I-V characteristics of CNTs soldered across the multiple gaps (b) Physically placed CNTs: as-placed on the gap electrode (curve 1), after drop-casting Pd precursor (curve 2), after application of external bias (curve 3) and after toluene wash (curve 4).

In order to avoid excess of Pd precursor in the gap as well as in the surrounding regions, the precursor was retained only at the edges of the gap by cross-linking

using electron beam and developing in toluene to wash away rest of the precursor (see section 4.4.2 for details on EBL). A drop of CNT dispersion on patterned Pd precursor gave rise to a circuit with a CNTs across the gap as shown in the schematic in Figure 8.4.

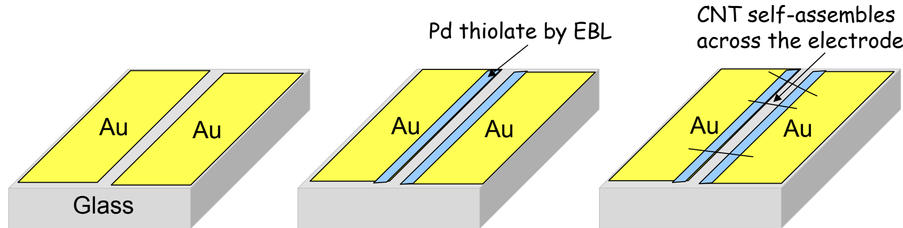

Figure 8.4: Scheme of the procedure adopted, where the Pd solder is first patterned on top of Au electrodes along the gap, before dropping CNTs.

In the first attempt, a single CNT was seen across the gap (7 μm wide, 120 μm long) as shown in Figure 8.5a. The corresponding I-V sweeps are shown in Figure 8.5b. Initially, there is little current in the circuit (curve 1). Following thermolysis at 250 °C for 10 minutes, the current improved (see curve 2 in Figure 8.5b), however, the I-V was non-linear. A 30 V bias was applied for few seconds. A sweep in 1 V showed a linear I-V with a resistance value of 4.9 kΩ(see curve 1 in Figure 8.5c). This value is typical of a single CNT [190]. While a toluene wash was required to improve the coupling in the previous case (Figure 8.3), here thermolysis alone is able to get rid of the hydrocarbon from the solder. On repeating the sweep, surprisingly, only negligible current was seen (see curve 2 in Figure 8.5c). The corresponding SEM image in Figure 8.5d shows that the CNT had blown off due to joule heating. Interestingly, the soldering material at the two ends appears to have vaporized leaving behind trench like features (see Figure 8.5e). Pd nanoparticles could be seen in the trenches. The deposits in the gap regions which created ‘ghost’ image of the CNT might have originated from the recondensation of the vaporized solder.

It is known that thermolysis induces the formation of metallic species while getting rid of hydrocarbon species. A small electrical activation could then improve the coupling between metal species and the CNT making the contact ohmic.

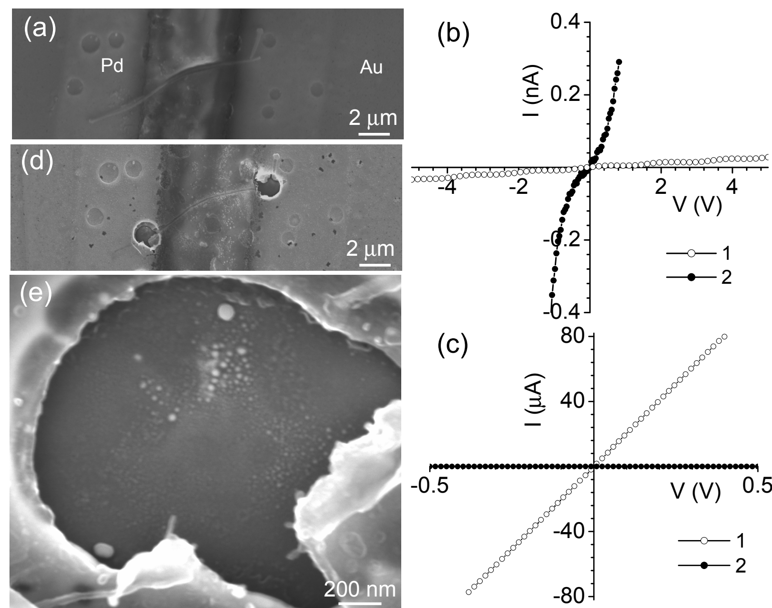

Figure 8.5: (a) SEM image of a CNT placed on the cross-linked Pd precursor on Au electrodes, (b) I-V characteristics of CNT before (curve 1) and after (curve 2) thermolysis at 250 °C for 10 minutes, (c) I-V characteristics of CNT after application of external bias (curve 1) and after blowing off the CNT (curve 2), (d) SEM image of blown off CNT by applying external bias and (e) SEM image of one of the trenches formed.

In another attempt, a drop of CNT dispersion on patterned Pd precursor produced a circuit with as many as nine CNTs in parallel across the gap (see Figure 8.6). I-V sweep produced a non-linear curve with current in the range of nA (see Figure 8.7a). The current is somewhat higher compared to similar situation with a single CNT, as there are nine parallel CNTs (compare Figure 8.7a with curve 1 in Figure 8.5b). Following thermolysis, the resistance dropped to 48.8 kΩ even without any high voltage activation. A repeated sweep produced such a high current that many CNTs were damaged and the current dropped to negligible values (see Figure 8.7c). The CNT-solder coupling must have improved so much during

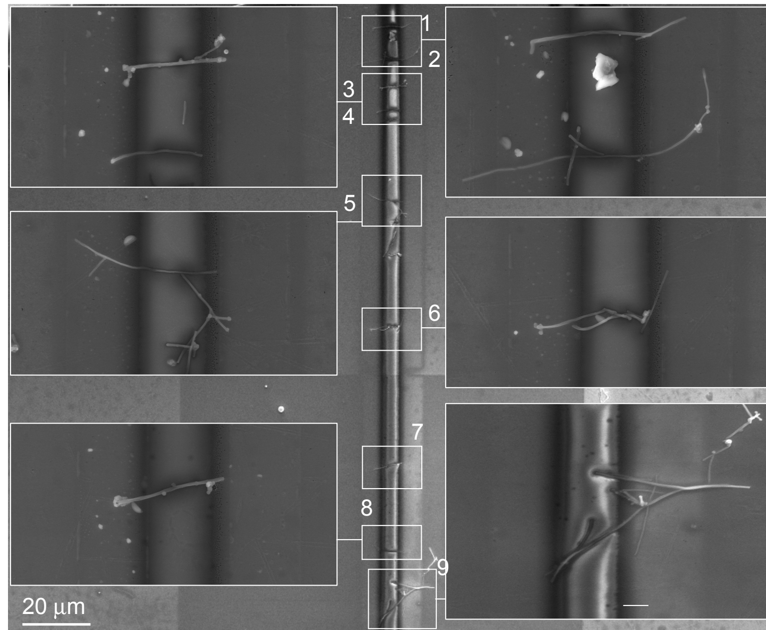

Figure 8.6: SEM image of the CNTs lying perpendicular to the gap. Zoom in images are also shown as insets.

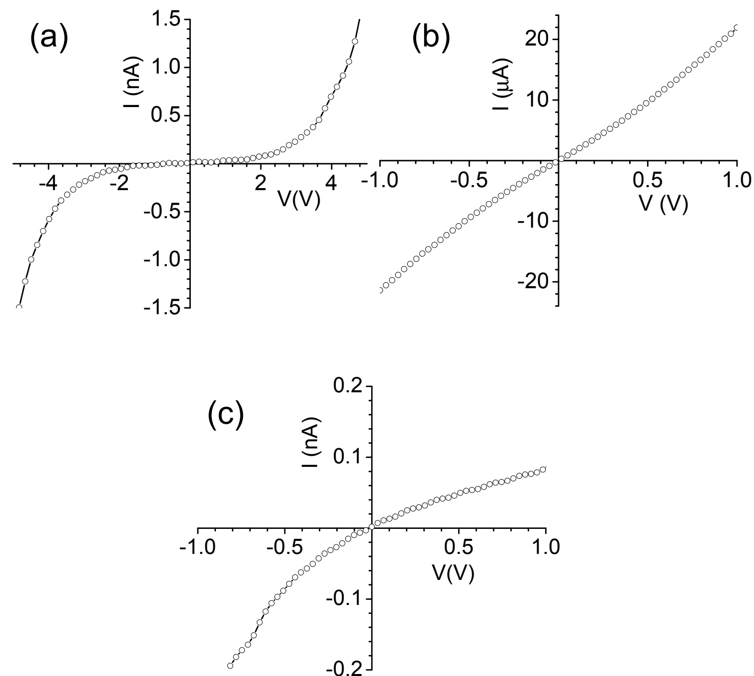

Figure 8.7: I-V characteristics of (a) CNTs placed across the gap, (b) after thermolysis at 250 °C for 10 minutes and (c) after application of external bias.

the second sweep that the CNTs were not able to handle the current any longer against Joule heating. Unlike the single CNT circuit in Figure 8.5, here the remains of the damaged CNTs were clearly visible along with cracked soldering material (see Figure 8.8).

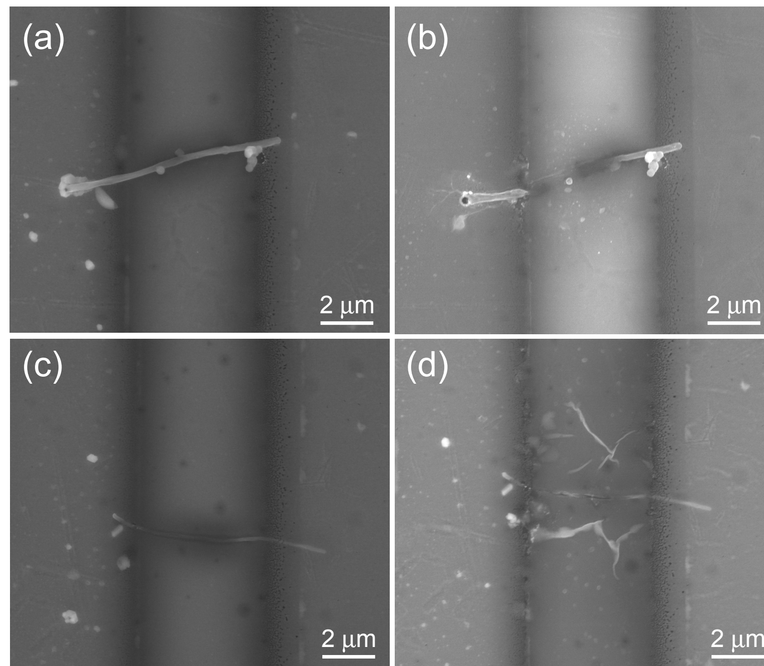

Figure 8.8: SEM image of CNTs lying across the gap before (a and c) and after (b and d) application of external bias.

The soldering action of Pd hexadecanethiolate is evident. Based on the above studies, one may deduce the following - Thermolysis giving rise to metallic species followed by an electrical activation to increase the coupling seems to be the best way to establish the soldering action. A gentle toluene wash may help remove hydrocarbons if any.

A striking feature of CNT circuits shown in Figures 8.5 and 8.6 is that the nanotubes are seen placed themselves in a highly desired configuration, i.e., nearly perpendicular to the gap and almost equally spanning on both the electrodes, much like what was seen on a PDMS stamp surface [193]. They are also well

spaced laterally. Further, no nanotube is seen lying within the gap parallel to it; neither are many nanotubes seen on rest of the electrode areas. This is clearly a self-assembly process driven by the Pd hexadecanethiolate, which is also serving as a nanosolder.

8.5 Conclusions

Nanosoldering action of Pd hexadecanethiolate is demonstrated on carbon fibre and CNTs. Self-assembly on CNTs is seen across the patterned Pd thiolate on the electrodes. A striking feature of CNT circuits developed in this study is that the nanotubes are seen placed themselves in a highly desired configuration shown to work as an excellent solder as well.

References

[1] Rao C. N. R., Thomas P. J. and Kulkarni G. U. *Nanocrystals: Synthesis, properties and applications, Springer-Verlag*, **2007**.

[2] Faraday M. *Philos. Trans. R. Soc.* London. **1857**, *147*, 145.

[3] www-unix.oit.umass.edu/∼blaylock/p284.

[4] El-Kareh B. *Fundamentals of Semiconductor Processing Technologies. Kluwer Academic Publishers, Dordrecht, The Netherlands*, **1995**.

[5] Whyte W. *Cleanroom Technology. Wiley. Publishers.*

[6] Klein M. V. and Furtak T.E. *OPTICS; John Wiley and Sons: New York, USA*, **1986**.

[7] Smith H. I. and Schattenburg M. L. *IBM J. Res. Develop.* **1993**, *31*, 319.

[8] Ito T. and Okazaki S. *Nature* **2000**, *406*, 1027.

[9] www.ifn.cnr.it/Groups/XRay/xray-optics.htm.

[10] Freeman D., Madden S. and Luther-Davies B. *Optics Express* **2005**, *13*, 3079.

[11] Myers B. D. and Dravid V. P. *Nano Lett.* **2006**, **6**, 963.

[12] Donthu S., Pan Z., Myers B., Shekhawat G., Wu N. and Dravid V. P. *Nano Lett.* **2005**, **5**, 1710.

[13] Loos J. *Adv. Mater. 2005*, 17, 1821.

[14] Ginger D. S., Zhang H. and Mirkin C. A. *Angew. Chem. Int. Ed.* **2004**, *43*, 30.

[15] Xia Y., Rogers J. A., Paul K. E. and Whitesides G. M. *Chem. Rev.* **1999**, *99*, 1823.

[16] Xia Y. and Whitesides G. M. *Angew. Chem. Int. Ed.* **1998**, *37*, 550.

[17] Tseng A. A., Chen K., Chen C. D. and Ma K. J. *IEEE Trans. Elect. Pack. Manufact.* **2003**, *26*, 141.

[18] van Dorp W. F., van Someren B., Hagen C. W. and Kruit P. *Nano Lett.* **2005**, **5**, 1303.

[19] Lipp S., Frey L., Lehrer C., Demm E., *Pauthner S. and Ryssel H. Proceedings of the 7th European Symposium* **1996**, 1779.

[20] www.s3.infm.it/fib.html.

[21] Saifullah M. S. M., Subramanian K. R. V.,Tapley E., Kang D.-J., Welland M. E. and Butler M. *Nano Lett.* **2003**, **3**, 1587.

[22] www.optics.org/cws/article/research/24274.

[23] Becker R. S., Golovchenko J. A. and Swartzentruber B. S. *Nature* **1987**, *325*, 419.

[24] Dagata J. A., Perez-Murano F., Abadal G., Morimoto K., Inoue T., Itoh J. and Yokoyama H., *Appl. Phys. Lett. 2000*, *76*, 2710.

[25] Vijaykumar T. and Kulkarni. G. U. *Nanotechnology* **2007**, *18*, 445303.

[26] Crommie M. F., Lutz C. P. and Eigler D. M. *Science*, **1993**, *262*, 218.

[27] Garno J. C., Yang Y. and Am N. A. *Nano Lett.* **2003**, *3*, 389.

[28] Bachtold A., Hadley P., Nakanishi T. and Dekker C. *Science* **2001**, *294*, 1317.

[29] Bernstein G. H., Hill D. A. and Liu W. *J. Appl. Phys.* **1992**, *71*, 4066.

[30] Chen J. K., Ko F. H. and Chang F. C. *Adv. Funct. Mater.* **2005**, *15*, 1147.

[31] Zailer I., Frost J. E. F., Chabasseur-Molyneux, V., Ford C. J. B. and Pepper M. *Semicond. Sci. Technol.* **1996**, *11*, 1235.

[32] Hoole A. C. F., Welland M. E. and Broers A. N. *Semicond. Sci. Technol.* **1997**, *12*, 1166.

[33] Geis M. W., Randall J. N., Mountain R. W., Woodhouse J. D., Bromley E. I., Astolfi D. K. and Economou N. P. *J. Vac. Sci. Technol. B* **1985**, *3*, 343.

[34] Tada T., Kanayama T., Robinson A. P. G., Palmer R. E., Allen M. T., Preece J. A. and Harris K. D. M. *Microelect. Engineering* **2000**, *53*, 425.

[35] Robinson A. P. G., Palmer R. E., Tada T., Kanayama T., Allen M. T., Preece J. A. and Harris K. D. M. *J. Vac. Sci. Technol. B* **2000**, *18*, 2730.

[36] Robinson A. P. G., Palmer R. E., Tada T., Kanayama T., Allen M. T., Preece J. A. and Harris K. D. M. *J. Phys D: Appl. Phys.* **1999**, *32*, L75.

[37] Seki S., Kanzaki K., Yoshida Y., Tagawa S., Shibata H., Asai K. and Ishigure K. *Jpn. J. Appl. Phys.* **1997**, *36*, 5361.

[38] Wu M., Chuang C., Chen Y. and Su W. *J. Mater. Chem.* **2008**, *18*, 780.

[39] Chuang C. M., Wu M. C., Huang Y. C., Cheng K. C., Lin C. F., Chen Y. F. and Su Y. F. *Nanotechnology* **2006**, *17*, 4399.

[40] Mallory G. O. and Hadju J. B. *Eds, Electroless plating Fundamentals and Applications, Orlando, FL*, 1990.

[41] Magagnin L., Maboudian R. and Carraro C., *J. Phys. Chem. B* **2002**, *106*, 401.

[42] Imamura S., Tamamura T., Harada K. and Sugawara S. *J. Appl. Poly. Sci.* **1982**, *27*, 937.

[43] Khoury M. and Ferry D. K. *J. Vac. Sci. Technol. B* **1996**, *14*, 75.

[44] Austin M. D., Zhang W., Ge H., Wasserman D., Lyon S. A. and Chou S. Y. *Nanotechnology* **2005**, *16*, 1058.

[45] Choi C. H. and Kertesz M. *J. Phys. Chem. A* **1997**, *101*, 3823.

[46] Flouttard J. L., Akinnifesi J., Cambril E. and Despax B. *J. Appl. Phys.* **1991**, *70*, 798.

[47] Ferrari A. C. and Robertson J. *Phys. Rev. B* **2000**, *61*, 14095.

[48] Eilers H., Biswas A., Pounds T. D., Norton M. G. and Elbahri M. *J. Mater. Res.*, **2006**, *21*, 2168.

[49] Peng Z., Guo L., Zhang Z., Tesche B., Wilke T., Ogermann D. Hu S. and Kleinermanns K. *Langmuir*, **2006**, *22*, 10915.

[50] Porel S., Singh S., Harsha S. S., Rao D. N. and Radhakrishnan T. P. *Chem. Mater.*, **2005**, *17*, 9.

[51] Deshmukh R. D. and Composto R. J. *Chem. Mater.*, **2007**, *19*, 745.

[52] Basak D., Karan S. and Mallik B. *Sol. Stat. Commun.*, **2007**, *141*, 483.

[53] Mahapatra S. K., Bogle K. A., Dhole S. D. and Bhoraskar V. N. *Nanotechnology* **2007**, *18*, 135602.

[54] Gates B. D., Xu Q., Stewart M., Ryan D., Willson C. G. and Whitesides, G. M. *Chem. Rev.* **2005**, *105*, 1171.

[55] Tseng A. A. *Small* **2005**, *1*, 924.

[56] Lin J. F., Bird J. P., Rotkina L. and Bennett P. A. *Appl. Phys. Lett.* **2003**, *82*, 802.

[57] Tham D., Nam C. Y. and Fischer J. E. *Adv. Mater.* **2006**, *18*, 290.

[58] Brintlinger T., Fuhrer M. S., Melngailis J., Utke I., Bret T., Perentes A., Hoffmann P., Abourida M. and Doppelt P. *J. Vac. Sci. Technol. B* **2005**, *23*, 3174.

[59] De Marzi G., Lacopino D., Quinn A. J., Redmond, G. *J. Appl. Phys.* **2004**, *96*, 3458.

[60] Valizadeh S., Abid M., Hernández-Ram´irez F., Rodr´iguez A. R., Hjort K. and Schweitz J. A. *Nanotechnology* **2006**, *17*, 1134.

[61] Im Y., Lee C., Vasquez R. P., Bangar M. A., Myung N. V., Menke E. J., Penner R. M. and Yun M. *Small* **2006**, *2*, 356.

[62] Kind H., Bonard J. M., Emmenegger C., Nilsson L. O., Hernadi K., Maillard-Schaller E., Schlapbach L., Forró L. and Kern K. *Adv. Mater.* **1999**, *11*, 1285.

[63] Lee J. Y., Yin D. and Horiuchi S. *Chem. Mater.* **2005**, *17*, 5498.

[64] Corbierre M. K., Beerens J. and Lennox R. B. *Chem. Mater.* **2005**, *17*, 5774.

[65] Corbierre M. K., Beerens J., Beauvais J. and Lennox R. B. *Chem. Mater.* **2006**, *18*, 2628.

[66] Stark T. J., Mayer T. M., Griffis D. P. and Russell P. E. *J. Vac. Sci. Technol. B* **1991**, *9*, 3475.

[67] Chan W. Y., Clendenning S. B., Berenbaum A., Lough A. J., Aouba S., Ruda H. E. and Manners I. *J. Am. Chem. Soc.* **2005**, *127*, 17651772.

[68] Hoffmann P., Assayag G. B., Gierak J., Flicstein J., Maar-Stumm M. and van den Bergh H. *J. Appl. Phys.* **1993**, *74*, 75881.

[69] Werts M. H. V., Lambert M., Bourgoin J. P. and Brust M. *Nano Lett.* **2002**, *2*, 43.

[70] Griffith S., Mondol M., Kong D. S. and Jacobson J. M. *J. Vac. Sci. Technol. B* **2002**, *20*, 2768.

[71] Reetz M. T., Winter M., Dumpich G., Lohau J. and Friedrichowski S. F. *J. Am. Chem. Soc.* **1997**, *119*, 4539.

[72] Lohau J., Friedrichowski S., Dumpich, G.; Wassermann E. F., Winter M. and Reetz M. T. *J. Vac. Sci. Technol. B* **1998**, *16*, 77.

[73] Ross I. M., Luxmoore I. J., Cullis A. G., Orr J., Buckle P. D. and Jefferson J. H. *J. Phys.: Conf. Ser.* **2006**, *26*, 363.

[74] Kunz R. R. and Mayer T. M. *J. Vac. Sci. Technol. B* **1988**, *6*, 1557.

[75] Rotkina L., Oh, S., Eckstein J. N. and Rotkin S. V. *Phys. Rev. B* **2005**, *72*, 233407.

[76] Koops H. W. P., Schössler C., Kaya A. and Weber M. *J. Vac. Sci. Technol. B* **1996**, *14*, 4105.

[77] Botman A., Mulders J. J. L., Weemaes R. and Mentink S. *Nanotechnology* **2006**, *17*, 3779.

[78] Barry J. D., Ervin M., Molstad J., Wickenden A., Brintlinger T., Hoffman P. and Meingailis J. *J. Vac. Sci. Technol. B 2006*, *24*, 3165.

[79] Utke I., Hoffmann P., Dwir B., Leifer K., Kapon E. and Doppelt P. *J. Vac. Sci. Technol. B* **2000**, *18*, 3168.

[80] Prestigiacomo M., Bedu F., Jandard F., Tonneau D., Dallaporta H., Roussel L. and Sudraud P. *Appl. Phys. Lett.* **2005**, *86*, 192112.

[81] Puretz J. and Swanson L. W. *J. Vac. Sci. Technol. B* **1992**, *10*, 2695.

[82] Tao T., Ro J., Melngailis J., Xue Z. and Kaesz H. D. *J. Vac. Sci. Technol. B* **1990**, *8*, 1826.

[83] Peate-Quesada L., Mitra J. and Dawson P. *Nanotechnology* **2007**, *18*, 215203.

[84] Telari K. A., Rogers B. R., Fang H., Shen L., Weller R. A. and Braski D. N. *J. Vac. Sci. Technol. B* **2002**, *20*, 590.

[85] Yan J. and Gupta M. C. *J. Vac. Sci. Technol. B* **2004**, *22*, 3202.

[86] Yin, D., Horiuchi S., Morita M. and Takahara A. *Langmuir* **2005**, *21*, 9352.

[87] Geissler M., Wolf H., Stutz R., Delamarche E., Grummt U. W., Michel B. and Bietsch A. *Langmuir* **2003**, *19*, 6301.

[88] Thomas P. J., Lavanya A., Sabareesh V. and Kulkarni G. U. *Proc. Indian Acad. Sci. (Chem. Sci.)* **2001**, *113*, 611.

[89] Nakamoto M., Yamamoto M. and Fukusumi M. *Chem. Commun.* **2002**, 1622-1623.

[90] Carotenuto G., Martorana B., Perlo P. and Nicolais L. *J. Mater. Chem.* **2003**, *13*, 2927.

[91] John, N. S. Ph.D. Thesis, *Investigations of Metal and Metal- Organic Bilayer Nanostructures Employing Atomic Force Microscopy and Related Techniques*; Jawaharlal Nehru Centre for Advanced Scientific Research, Bangalore, **2007** (620.11 P07).

[92] *CRC Handbook of Chemistry and Physics*, 84th Edition.

[93] Thompson L. F., Willson C. G. and Bowden M. J. *Introduction to Microlithography; 2nd Eds; American Chemical Society: Washington*, DC, **1994**.

[94] Brusatin G., Della Giustina G., Romanato F. and Gulielmi M. *Nanotechnology* **2008**, *19*, 175306.

[95] Seshadri K., Froyd K., Parikh A. N., Allara D. L., Lercel M. J. and Craighead H. G. *J. Phys. Chem.* **1996**, *100*, 15900.

[96] John N. S., Thomas P. J. and Kulkarni G. U. *J. Phys. Chem. B* **2003**, *107*, 11376.

[97] Maroncelli M., Qi S. P., Strauss H. L. and Snyder R. G. *J. Am. Chem. Soc.* **1982**, *104*, 6237.

[98] Snyder R. G., Maroncelli M., Qi S. P. and Strauss H. L. *Science* **1981**, *214*, 188.

[99] Suresh R., Venkataraman N., Vasudevan S. and Ramanathan K. V. *J. Phys. Chem. C* **2007**, *111*, 495.

[100] Venkataraman N. and Vasudevan S. *J. Phys. Chem. B* **2001**, *105*, 7639.

[101] Venkataraman N. and Vasudevan S. *J. Phys. Chem. B* **2001**, *105*, 1805.

[102] Venkataraman N. and Vasudevan S. *J. Phys. Chem. B* **2002**, *106*, 7766.

[103] Fujimori A., Mamiya K., Mizokawa T., Miyadai T., Sekiguchi T., Takahashi H., Mori, N. and Suga S. *Phys. Rev. B* **1996**, *54*, 16329.

[104] Kautz R. L., Dresselhaus M. S., Adler D. and Linz A. *Phys. Rev. B* **1972**, *6*, 2078.

[105] Miyadai T. *J. Phys. Soc. Jpn.* **1975**, *39*, 63.

[106] Wilson J. A., *The Metallic and Nonmetallic States of Matter, Taylor and Francis, London*, **1985**, 215.

[107] Sarma D. D., Krishnakumar S. R., Weschke E., Schubler-Langeheine C., Mazumdar C., Kilian L., Kaindl G., Mamiya K., Fujimori S. I., Fujimori A. and Miyadai T. *Phys. Rev. B* **2003**, *67*, 1551121.

[108] John N. S., Kulkarni G. U., Datta A., Pati, S. K., Komori F., Kavitha K., Narayana C. and Sanyal M. K. *J. Phys. Chem. C* **2007**, *111*, 1868.

[109] Blanchard S., Neese F., Bothe E., Bill E., Weyhermu1ller T. and Wieghardt K. *Inorg. Chem.* **2005**, *44*, 3636.

[110] Thio T. and Bennett J. W. *Phys. Rev.B* **1994**, *50*, 10574.

[111] Chen X., Li J., Cao Y., Lan Y., Li H., He M., Wang C., Zhang Z. and Qiao Z. *Adv. Mater.* **2000**, *12*, 1432.

[112] Hannon J. B., Kodambaka S., Ross F. M. and Tromp R. M. *Nature* **2006**, *440*, 69.

[113] Pan Z. W., Dai Z. R., Ma C. and Wang Z. L. *J. Am. Chem. Soc.* **2002**, *124*, 1817.

[114] Bethune D. S., Kiang C. H., De Vries M. S., Gorman G., Savoy R., Vazquez J. and Beyers R. *Nature* **1993**, *363*, 605.

[115] Lee J. S., Gu G. H., Kim H., Suh J. S., Han I., Lee N. S., Kim J. M. and Park G. *Syn. Metals* **2001**, *124*, 307.

[116] Peng H. B., Ristroph T. G., Schurmann G. M., King G. M., Yoon J., Narayanamurti V. and Golovchenko J. A. *Appl. Phys. Lett.* **2003**, *83*, 4238.

[117] Ago H., Murata K., Yumura M., Yotani J. and Uemura S. *Appl. Phys. Lett.* **2003**, *82*, 811.

[118] Martensson T., Carlberg P., Borgstro?m M., Montelius L., Seifert W. and Samuelson L. *Nano Letters* **2004**, *4*, 699.

[119] Martensson T., Borgstro?m M., Seifert W., Ohlsson B. J. and Samuelson L. *Nanotechnology* **2003**, *14*, 1255.

[120] Kind H., Bonard J., Emmenegger C., Nilsson L., Hernadi K., Maillard-Schaller E., Schlapbach L., Forror L. and Kern K. *Adv. Mater.* **1999**, *11*, 1285.

[121] Wolfe D. B., Love J. C., Paul K. E., Chabinyc M. L. and Whitesides G. M. *Appl. Phys. Lett.* **2002**, *80*, 2222.

[122] Greyson E. C., Babayan Y. and Odom T. W. *Adv. Mater.* **2004**, *16*, 1348.

[123] Ren Z. F., Huang Z. P., Wang D. Z., Wen J. G., Xu J. W., Wang J. H., Calvet L. E., Chen J., Klemic J. F. and Reed M. A. *Appl. Phys. Lett.* **1999**, *75*, 1086.

[124] Wang X., Summers C. J. and Wang Z. L. *Nano Letters* **2004**, *4*, 423.

[125] Fan H. J., Lee W., Scholz R., Dadgar A., Krost A., Nielsch K. and Zacharias M. *Nanotechnology* **2005**, *16*, 913.

[126] Li W. Z., Xie S. S., Qian L. X., Chang B. H., Zou B. S., Zhou W. Y., Zhao R. A. and Wang G. *Science* **1996**, *274*, 1701.

[127] Huang M. H., Wu Y. Feick H., Tran N., Weber E. and Yang P. *Adv. Mater.* **2001**, *13*, 113.

[128] Tak Y. and Yong K. *J. Phys Chem. B* **2005**, *109*, 19263.

[129] Saito N., Haneda H., Sekiguchi T., Ohashi N., Sakaguchi I. and Koumoto K. *Adv. Mater.* **2002**, *14*, 418.

[130] Saito N., Haneda H., Seo W. and Koumoto K. *Langmuir* **2001**, *17*, 1461.

[131] Lee J. Y., Horiuchi S. and Choi H. K. *Mater. Chem. Phys.* **2007**, *101*, 387.

[132] Lee J. Y., Yin D. and Horiuchi S. *Chem. Mater.* **2005**, *17*, 5498.

[133] Schmidt-Mende L. and MacManus-Driscoll J. L. *Mater. Today* **2007**, *10*, 40.

[134] Baker G. A. and Moore D. S. *Anal. Bioanal. Chem.* **2005**, *382*, 1751.

[135] Campion A. and Kambhampati P. *Chem. Soc. Rev.* **1998**, *27*, 241.

[136] Moskovits M. *Rev. Mod. Phys.* **1985**, *57*, 783.

[137] Drachev V. P., Nashine V. C., Thoreson M. D., Ben Amotz D.,Jo Davisson V. and Shalaev V. M. *Langmuir* **2005**, *21*, 8368.

[138] Gong J. L., Jiang J. H., Yang H. F., Shen G. L., Yu R. Q. and Ozaki Y. *Anal. Chim. Acta* **2006**, *564*, 151.

[139] Ni J., Lipert R. J., Dawson G. B. and Porter M. D. *Anal. Chem.* **1999**, *71*, 4903.

[140] Faulds K., Smith W. E., Graham D. *Anal. Chem.* **2004**, *76*, 412.

[141] Graham D., Mallinder B. J. and Smith W. E. *Angew. Chem. Int.Ed.* **2000**, *39*, 1061.

[142] Moore B. D., Stevenson L., Watt A., Flitsch S., Turner N. J., Cassidy C. and Graham D. *Nat. Biotechnol.* **2004**, *22*, 1133.

[143] Kneipp K., Haka A. S., Kneipp H., Badizadegan K. Yoshizawa N., Boone C. Shafer-Peltier K. E., Motz J. T., Dasari R. R. and Feld M. S. *Appl. Spectrosc.* **2002**, *56*, 150.

[144] Sengupta A., Laucks M. L. and Davis E. *J. Appl. Spectrosc.* **2005**, *59*, 1016.

[145] Reyes-Goddard J. M., Barr H. and Stone N. *Photodiagn. Photodyn. Ther.* **2005**, *2*, 223.

[146] Vo-Dinh T., Stokes D. L., Griffin G. D., Volkan M., Kim U. J. and Simon M. I. *J. Raman Spectrosc.* **1999**, *30*, 785.

[147] Yu C. C. and Liu Y. C. *Anal. Chim. Acta* **2006**, *566*, 130.

[148] Chase B. and Parkinson B. *J. Phys. Chem.* **1991**, *95*, 7810.

[149] Tian Z. Q., Ren B. and Wu D. Y. *J. Phys. Chem. B* **2002**, *106*, 9463.

[150] Tian Z. Q., Yang Z. L., Ren B., Li J. F., Zhang Y., Lin X. F., Hu J. W. and Wu D. Y. *Faraday Discussions* **2006**, *132*, 159.

[151] Gómez R., Pérez J. M., Solla G., Montiel V. and Aldaz A. *J. Phys. Chem. B* **2004**, **108**, 9943.

[152] Abdelsalam M. E., Mahajan S., Bartlett P. N., Baumberg J. J. and Russell A. E. *J. Am. Chem. Soc.* **2007**, *129*, 7399.

[153] Liu Z., Yang Z. L., Cui L., Ren B. and Tian Z. Q. *J. Phys. Chem. C* **2007**, *111*, 1770.

[154] Li Y., Lu G., Wu X. and Shi G. *J. Phys. Chem. B* **2006**, *110*, 24585.

[155] Dieringer J. A., McFarland A. D., Shah N. C., Stuart D. A., Whitney A. V., Yonzon C. R., Young M. A., Zhang X. and Van Duyne R. P. *Faraday Discuss.* **2006**, *132*, 9.

[156] Daniels J. K. and Chumanov G. *J. Phys. Chem. B* **2005**, *109*, 17936.

[157] Drachev V. P., Thoreson M. D., Nashine V., Khaliullin E. N., Ben Amotz D., Davisson V. J. and Shalaev V. M. *J. Raman Spectrosc.* **2005**, *36*, 648.

[158] Lu L., Eychmüller A., Kobayashi A., Hirano Y., Yoshida K., Kikkawa Y., Tawa K. and Ozaki Y. *Langmuir* **2006**, *22*, 2605.

[159] Kalkan A. K., Fonash S. J. *J. Phys. Chem. B* **2005**, *109*, 20779.

[160] Gunnarsson L., Bjerneld E. J., Xu H., Petronis S. and Kasemo B. Kall, M. *Appl. Phys. Lett.* **2001**, *78*, 802.

[161] Félidj N., Truong S. L., Aubard J., Levi G., Krenn J. R., Hohenau A., Leitner A. and Aussenegg F. R. *J. Chem. Phys.* **2004**, *120*, 7141.

[162] Schmidt J. P., Cross S. E. and Buratto S. K. *J. Chem. Phys.* **2004**, *121*, 10657.

[163] Bartlett P. N., Baumberg J. J., Coyle S. and Abdelsalam M. *Faraday Discuss.* **2003**, *123* 19.

[164] John N. S., Selvi N. R., Mathur M., Govindarajan R. and Kulkarni G. U. *J. Phys. Chem. B* **2006**, *110*, 22975.

[165] Forrest R. D., Burden A. P., Silva S. R. P., Cheah L. K. and Shi X. *Appl. Phys. Lett.* **1998**, *73*, 3784-3786.

[166] Johnson S. E., Ashfold M. N. R., Knapper M. P., Lade R. J., Rosser K. N., Fox N. A. and Wang W. N. *Diamond Relat. Mater.* **1997**, *6*, 569.

[167] Robertson J. *Mater. Sci. Eng. R* **2002**, *37*, 129.

[168] Ferrari A. C. and Robertson J. *Phys. Rev. B* **2000**, *61*, 14095.

[169] Ferrari A. C. and Robertson J. *Phys. Rev. B* **2001**, *64*, 075414.

[170] Zuruzi A. S., Ward M. S. and MacDonald N. C. *Nanotechnology* **2005**, *16*, 1029.

[171] Taylor C. E., Pemberton J. E., Goodman G. G. and Schoenfisch M. H. *Appl. Spectrosc.* **1999**, *53*, 1212.

[172] Shiu J.-Y. and Chen P., *Adv. Funct. Mater.* **2007**, *17*, 2680.

[173] Tinazli A., Piehler J., Beuttler M., Guckenberger R. and Tampe R. *Nat. Nanotechnol.* **2007**, *2*, 220225.

[174] Hildebrandt P. and Stockburger M. *J. Phys. Chem.* **1984**, *88*, 5935.

[175] Etchegoin P., Liem, H., Maher R. C., Cohen L. F., Brown R. J. C., Milton M. J. T. and Gallop J. C. *Chem. Phys. Lett.* **2003**, *367*, 223.

[176] Bizzarri A. R. and Cannistraro S. *Appl. Spectrosc.* **2002**, *56*, 1531.

[177] Fleischmann M., Hendra P. J. and McQuillan A. J. *Chem. Phys. Lett.* **1974**, *26*, 163.

[178] Jang N. H. *Bull. Korean Chem. Soc.* **2002**, *23*, 1790.

[179] Suh J. S. and Moskovits M. *J. Am. Chem. Soc.* **1986**, *108*, 4711.

[180] Dohn S., Molhave K. and Boggild P. *Sensor Lett.* **2005** *3*, 300.

[181] Ebbesen T. W., Lezec H. J., Hiura H., Bennett J. W., Ghaemi H. F. and Thio T. *Nature* **1996**, *382*, 54.

[182] Schoenenberger C., Bachtold A., Strunk C., Salvetat J. P. and Forro L. *Appl. Phys. A: Mater. Sci. Processing* **1999**, *69*, 283.

[183] Lewenstein J. C., Burgin T. P., Ribayrol A., Nagahara L. A. and Tsui R. K. *Nano Lett.* **2002**, *2*, 443.

[184] Klinke C. Hannon J. B., Afzali A. and Avouris P. *Nano Lett.* **2006**, *6*, 906.

[185] Gao, B., Chen Y. F., Fuhrer M. S., Glattli D. C. and Bachtold A. *Phys. Rev. Lett.* **2005**, *95*, 196802.

[186] Li S., Liu N., Chan-Park M. B., Yan Y. and Zhang Q. *Nanotechnology***2007**, *18*, 455302.

[187] Vijayaraghavan A., Blatt S., Weissenberger D., Oron-Carl M. Hennrich F., Gerthsen D., Hahn H. and Krupke R. *Nano Lett.* **2007**, *7*, 1556.

[188] Schwamb T., Choi T., Schirmer N., Bieri N. R., Burg B., Tharian J., Sennhauser U. and Poulikakos D. *Nano Lett.* **2007**, *7*, 3633.

[189] Bachtold A., Henny M., Terrier C., Strunk C., Schönenberger C., Salvetat J., Bonard J and Forro? L. *Appl. Phys. Lett.* **1998**, *73*, 274.

[190] Madsen D. N., Moølhave K., Mateiu R., Rasmussen A. M., Brorson M., Jacobsen C. J. H. and Bggild P. *Nano Lett.* **2003**, *3*, 47.

[191] Dockendorf C. P. R., Steinlin M., Poulikakos D. and Choi T. *Appl. Phys. Lett.* **2007**, *90*, 193116.

[192] Lee J., Park C., Kim J., Kim J., Park J. W. and Yoo K. *J. Phys. D* **2000**, *33*, 1953.

[193] Chen J. and Weimer W. A. *J. Am. Chem. Soc.* **2002**, *124*, 758.

Publications

1. Optimizing growth conditions for electroless deposition of Au films on Si(111) substrates, **Bhuvana T.** and Kulkarni G. U., *Bulletin of Materials Science*, **29**, 505-511 (2006).

2. Nanogranular Au films deposited on carbon covered Si substrates for enhanced optical reflectivity and Raman scattering, **Bhuvana T.**, Pavan Kumar G. V., Narayana C. and Kulkarni G. U., *Nanotechnology*, **18**, 145702 (2007).

3. Carbon assisted electroless gold for surface enhanced raman scattering studies, **Bhuvana T.**, Pavan Kumar G. V., Narayana C. and Kulkarni G. U., *Journal of Physical Chemistry C*, **111**, 6700-6705 (2007).

4. Highly Conducting Patterned Pd Nanowires by Direct-Write Electron Beam Lithography, **Bhuvana T.** and Kulkarni G. U., *ACS Nano*, **2**, 457-462 (2008).

5. A SERS-Active Nanocrystalline Pd Substrate and its Nanopatterning Leading to Biochip Fabrication, **Bhuvana T.** and Kulkarni G. U., *Small*, **4**, 670-676 (2008).

6. Polystyrene as a zwitter resist in electron beam lithography based electroless patterning of gold, **Bhuvana T.** and Kulkarni G. U., *Bulletin of Materials*

Science, **31**, 201-206 (2008).

7. The electron resist behavior of Pd hexadecanethiolate examined using x-ray photoelectron spectroscopy with nanometric lateral resolution, **Bhuvana T.**, Gregoratti L., Heun S., Dalmiglio M. and Kulkarni G. U., *Submitted* (2008).

8. Femtolitre cups of Ag as SERS active containers for bioanalysis, **Bhuvana T.** and Kulkarni G. U., *Submitted* (2008).

9. Catalytic growth of ZnO nanostructures on electron beam patterned Pd, **Bhuvana T.** and Kulkarni G. U., *Under preparation.*

10. Silver-triphenylphosphine-nitrate-polystyrene blend as an electron resist leading to conducting Ag nanocrystal patterns, **Bhuvana T.**, Subramaniam C., Pradeep T. and Kulkarni G. U., *Under preparation.*

11. Direct-Write Electron Beam Lithography on Ni thiolate for NiS_2 nanowire circuits, **Bhuvana T.** and Kulkarni G. U., *Under preparation.*

12. Nanosoldering CNTs to electrodes using Pd hexadecanethiolate, **Bhuvana T.**, Smith K. C., Fisher T. S. and Kulkarni G. U., *Under preparation.*

Other publications

1. Gold nanostructuring on Si substrate by selective electroless deposition, **Bhuvana T.** and Kulkarni G. U., *Journal of Nanoscience and Nanotechnology*, **7**, 2063-2068 (2007).

2. Inhomogeneous vortex-state-driven enhancement of superconductivity in nanoengineered ferromagnet-superconductor heterostructures, Rakshit R. K., Budhani R. C., **Bhuvana T.**, Kulkarni V. N. and Kulkarni G. U., *Physical Review B - Condensed Matter and Materials Physics*, **77**, 052509 (2008).